DIRECT CONTACT MEMBRANE DISTILLATION FOR DESALINATION OF HIGH SALINITY BRINES: FUNDAMENTALS AND APPLICATION

by

Omkar R. Lokare

Bachelor of Chemical Engineering, Institute of Chemical Technology, 2012

Master of Chemical Engineering, Institute of Chemical Technology, 2014

Submitted to the Graduate Faculty of

Swanson School of Engineering in partial fulfillment

of the requirements for the degree of

Doctor of Philosophy

University of Pittsburgh

2018

UNIVERSITY OF PITTSBURGH

SWANSON SCHOOL OF ENGINEERING

This dissertation was presented

by

Omkar R. Lokare

It was defended on

August 27, 2018

and approved by

Radisav D. Vidic, Ph.D., Professor, Department of Civil and Environmental Engineering

Leonard Casson, Ph.D., Associate Professor,
Department of Civil and Environmental Engineering

Vikas Khanna, Ph.D., Associate Professor,
Department of Civil and Environmental Engineering

Carla Ng, Ph.D., Assistant Professor, Department of Civil and Environmental Engineering

Andrew Zydney, Ph.D., Professor,
Department of Chemical Engineering, Pennsylvania State University

Dissertation Director: Radisav D. Vidic, Ph.D., Professor,
Department of Civil and Environmental Engineering

DIRECT CONTACT MEMBRANE DISTILLATION FOR DESALINATION OF HIGH SALINITY BRINES: FUNDAMENTALS AND APPLICATION

Omkar R. Lokare, PhD

University of Pittsburgh, 2018

Membrane distillation is a cost effective solution for the treatment of high salinity wastewater where reverse osmosis is not feasible, especially if waste heat is utilized for its operation. One such example of high salinity wastewater is produced water generated as a consequence of hydraulic fracturing used for natural gas extraction from unconventional onshore resources. The objective of this study was to evaluate the feasibility of treating such high salinity wastewaters by employing membrane distillation while using waste heat as a source of energy to drive the process and by using produced water as an example wastewater. When commercially available membranes were tested in a direct contact membrane distillation (DCMD) system, the membranes exhibited excellent rejections of ions with no flux degradation due to fouling. However, it was found that concentration polarization (CP) was significantly higher when treating high salinity feed water and the CP effect could not be accurately estimated using current methods of calculation. Based on lab scale studies, an ASPEN Plus simulation was developed to simulate the operation of large scale systems and estimate energy requirements of the DCMD process to treat produced water in the state of Pennsylvania by using exhaust stream of Natural Gas Compressor Station (NG CS) as the waste heat source. The results from this study suggested that the waste heat available from NG CS

is sufficient to treat all the produced water generated in Pennsylvania regardless of its initial salinity.

In an attempt to study the effect of concentration polarization that was found to be significant during DCMD tests with produced water, and has been neglected in most membrane distillation studies, a novel spatially resolved non-intrusive spectrophotometric method was developed to measure the concentration profile of solute near the membrane surface in a direct contact membrane distillation system. The objective was to probe the concentration profile of solute and analyze the impact of operating parameters, such as feed concentration, hydrodynamic conditions and feed temperature, on the solute concentration profile in the boundary layer. A key finding of this study is that the conventional approach of estimating the effect of concentration polarization severely under predicts the boundary layer thickness (BLT) and concentration polarization coefficient (CPC). The results of this study highlight the need to develop new methods to estimate the BLT and CPC as the conventional approach of mass transfer analogy of heat transfer does not agree with experimental observations obtained for a membrane distillation system.

TABLE OF CONTENTS

LIST OF TABLES

LIST OF FIGURES

ACKNOWLEDGEMENTS

I would like to express my heartfelt gratitude to my PhD advisor Dr. Radisav Vidic for his guidance and unwavering support through the last four years. His patience, belief and motivation have helped me immensely in my research and personal development as a scientist. He has and continues to be a great mentor and inspiration for me in my career.

I would like to extend thanks to my lab mates and friends for being my family away from home and making my time in Pittsburgh so memorable and fun-filled.

Last but not the least I would like to thank my family for their being a constant source of support, motivation and love.

NOMENCLATURE

δ	boundary layer thickness (m)
ρ	fluid density (kg/m^3)
μ	fluid viscosity (Pa·s)
ρ	fluid density (kg/m^3)
υ	fluid velocity (m/s)
A	area of membrane (m^2)
AC	acrylic copolymer
BLT	boundary layer thickness (μm)
C	membrane distillation coefficient ($kg/m^2/s/Pa$ or LMH/kPa)
$C_{b,f}$	concentration of solute in the bulk feed stream (g/l)
$C_{m,f}$	concentration of solute at the feed-membrane interface (g/l)
CP	concentration polarization
C_p	specific heat of water (J/kg/K)
CPC	concentration polarization coefficient
D	solute diffusion coefficient (m^2/s)
DCMD	direct contact membrane distillation
d_f	diameter of spacer filament (m)
d_h	hydraulic diameter (m)

E	specific enthalpy (J/kg)
h	heat transfer coefficient ($W/m^2/K$)
H	spacer thickness (m)
h_f	heat transfer coefficient on the feed side ($W/m^2/K$)
h_p	heat transfer coefficient on the permeate side ($W/m^2/K$)
IC	ion chromatography
J	permeate flux ($kg/m^2/s$ or LMH)
J_s	solute flux across the membrane (m/s)
K	film-diffusion mass transfer coefficient (m/s)
k	thermal conductivity (W/m/K)
k_{dc}	correction factor for spacer geometry
k_f	thermal conductivity of the fluid (W/m/K)
L	latent heat of vaporization (kJ/kg)
l_m	spacer mesh size (m)
LMH	$L/m^2/hr$
m, M	flow rate (kg/s)
MD	membrane distillation
MD	membrane distillation
$\dot{m}_f$	feed mass flow rate (kg/s)
$\dot{m}_p$	permeate mass flow rate (kg/s)
NORM	naturally occurring radioactive material
Nu	Nusselt number
p	vapor pressure (Pa)

$P_{m,f}$	vapor pressures at the feed-membrane interface (Pa)
$P_{m,p}$	vapor pressures at the permeate-membrane interface (Pa)
PP	polypropylene
Pr	Prandtl number
PTFE	polytetrafluoroethylene
PVDF	polyvinylidene fluoride
Q	heat flux (W/m^2)/rate of heat transfer (W)
Re	Reynold number
SEM	scanning electron microscopy
T	absolute temperature (K)
$T_{b,f}$	bulk temperature of feed (^oC)
$T_{b,p}$	bulk temperature of permeate (^oC)
TDS	total dissolved solids (mg/L)
$T_{f,i}$	feed inlet temperature (K)
$T_{f,o}$	feed outlet temperature (K)
T_{in}	feed inlet temperature (^oC)
$T_{m,f}$	temperature at feed-membrane interface (^oC)
$T_{m,f}$	temperature at the feed-membrane interface (^oC)
$T_{m,p}$	temperature at permeate-membrane interface (^oC)
$T_{m,p}$	temperature at the permeate-membrane interface (^oC)
TOC	total organic carbon (mg/L)
T_{out}	feed exit temperature (^oC)
$T_{p,i}$	permeate inlet temperature (K)

$T_{p,o}$	permeate outlet temperature (K)
U	overall heat transfer coefficient ($W/m^2/K$)
W	water recovery (%)
x	fraction of feed that is recovered on the permeate side
X	salt concentration in the concentrate (g/L)
x	distance from the membrane surface (m)
X_o	salt concentration in the fresh feed (g/L)
δ	membrane thickness (m)
ΔH	latent heat of vaporization for water (J/kg)
ΔP	pressure difference (kPa)
ε	porosity (-)
η	evaporation efficiency (%)
θ	hydrodynamic angle
φ	spacer voidage

1.0 INTRODUCTION

1.1 WASTEWATER FROM HYDRAULIC FRACTURING

The use of hydraulic fracturing techniques to extract oil and natural gas from different formations has been assessed since the 1950s, while horizontal drilling has been used to produce oil since the early 1980s. These techniques were combined in the early 2000 to achieve successful large-scale natural gas productions from the Barnett Shale in Texas. Over the past few years, these technological advancements allowed access to vast quantities of natural gas from reservoirs that were previously considered uneconomical. In the United States, natural gas production increased from 0.3 trillion cubic feet in 2000 to 9.6 trillion cubic feet in 2012 [1]. U.S. has become a natural gas exporter in 2017 and it is expected to continue to export more natural gas than it imports throughout 2018 [2, 3]. Unconventional shale gas is a promising energy resource with major economic benefits but is accompanied by a host of environmental challenges, including increased level of methane emissions at shale gas production sites [4, 5], and the potential for drinking water [6] and groundwater contamination [7]. One of the critical challenges for this industry is the management of vast quantities of high salinity wastewater generated in the process of hydraulic fracturing [8].

During hydraulic fracturing, a mixture of water and chemicals (Table 1.1) known as fracturing fluid [9] is injected in a horizontal well to fracture the formation rock, increase its

permeability and facilitate flow of oil and gas into the well. After the pumping pressure is relieved, some of the fracturing fluid mixed with the formation water returns to the surface. This water is typically designated as flowback water [10] and is collected over a period of 2-3 weeks with a total volume ranging from 10-40% of the fracturing fluid volume [11]. Figure 1.1 shows how the quantity and quality of flowback water changes over time. Wastewater continues to be produced throughout the lifetime of the well but at a rate that is much lower than during the flowback period. This wastewater is known as produced water [10] and is characterized by high concentration of total dissolved solids (TDS) and presence of organic compounds [12]. The composition of produced water depends on the well location and it varies during the lifetime of the well [13].

Table 1.1 Common chemical additives for hydraulic fracturing [14]

Additive type	**Example compounds**	**Purpose**
Acid	Hydrochloric acid	Cleaning of wellbore, dissolving minerals and initiate cracks in the rock
Friction reducer	Polyacrylamide, petroleum distillate	Minimize friction between the fluid and pipe
Corrosion inhibitor	Isopropanol, acetaldehyde	Prevent corrosion of pipes
Iron control	Citric acid, thioglycolic acid	Prevent the precipitation of metal oxides
Biocide	Glutaraldehyde, 2,2-dibromo-3-nitrilopropionamide	Control bacteria
Gelling agent	Guar/xanthan gum or hydroxyethyl cellulose	Water thickener to suspend sand
Crosslinker	Borate salts	Increase fluid viscosity at high temperatures
Breaker	Ammonium persulfate, magnesium peroxide	Promote breakdown of gel polymers
Oxygen scavenger	Ammonium bisulfite	Remove oxygen from the liquid to reduce corrosion of pipes
pH adjustment	Potassium or sodium hydroxide or carbonate	Maintain the pH for other compounds to retain effectiveness
Proppant	Silica quartz sand	Keep fractures open

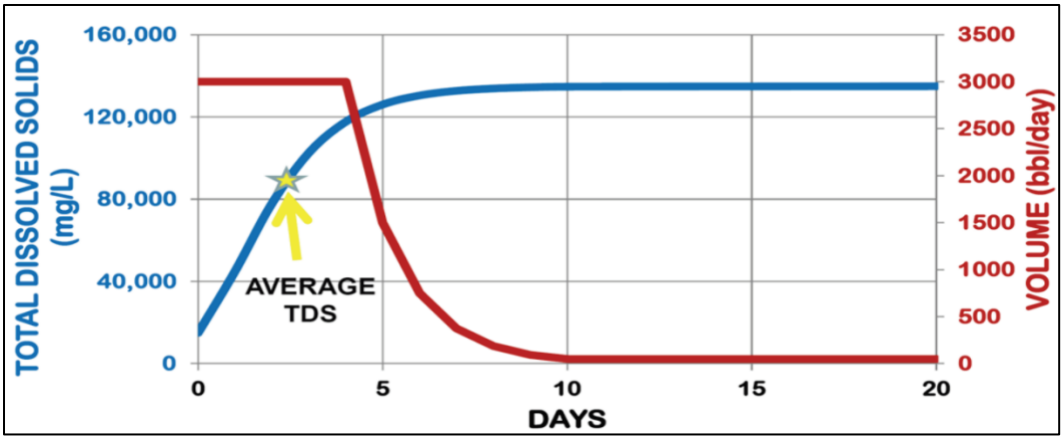

Figure 1.1 Total dissolved solids (TDS) and flowback volume in the early stage of well completion [15].

1.2 CURRENT TREATMENT/DISPOSAL STRATEGIES

Marcellus Shale (Figure 1.2) is a major natural gas (NG) reservoir with steadily increasing production since 2008 that currently accounts for about 40% of the total U.S. shale gas production [16]. Natural gas extraction from Marcellus shale in Pennsylvania, West Virginia and Ohio is accompanied by large amounts of produced water that contains high total dissolved solids (TDS). Figure 1.3 shows shale gas production in different shale plays in the U.S. from 200-2016 [17]. Future extraction of shale gas requires economical management of wastewater while also minimizing potential environmental impacts. Produced water injection into Class II Underground Injection Control (UIC) wells is the dominant management alternative in many shale plays with sufficient disposal capacity [10, 18, 19]. There are a total of about 144,000 Class II disposal wells in the U.S. with the majority of wells located in Texas (50,000 wells), California, Kansas, and Oklahoma [20]. Salt water disposal (SWD) wells account for 20% of total disposal wells of which 12,000 are located in Texas, 800 in Oklahoma, and only 8 in Pennsylvania [20]. In the Marcellus shale region, the average cost of produced water transportation from the well site in Pennsylvania

to injection wells in Ohio or West Virginia ranges from 10 to 20 $/barrel (bbl) [21, 22]. In addition, the costs associated with deep-well injection is estimated at $1/bbl [21]. Lack of sufficient disposal capacity in Pennsylvania requires the development of alternative approaches for management of high TDS produced water [23]. In areas of limited disposal capacity (e.g., Pennsylvania) or where water resources are stressed (e.g., Texas and Oklahoma), reuse and recycling of produced water is an attractive alternative to direct underground injection of produced water. Recent studies have also documented concerns over induced seismic activities due to deep-well injection [24-27], further emphasizing the need for the development of innovative management strategies for produced water to avoid unintended environmental consequences. Management strategies such as injecting wastewater into disposal wells, residual waste processing and reuse, roadspreading, and landfilling that are currently used in Pennsylvania may not guarantee the long-term sustainability of shale gas development [28].

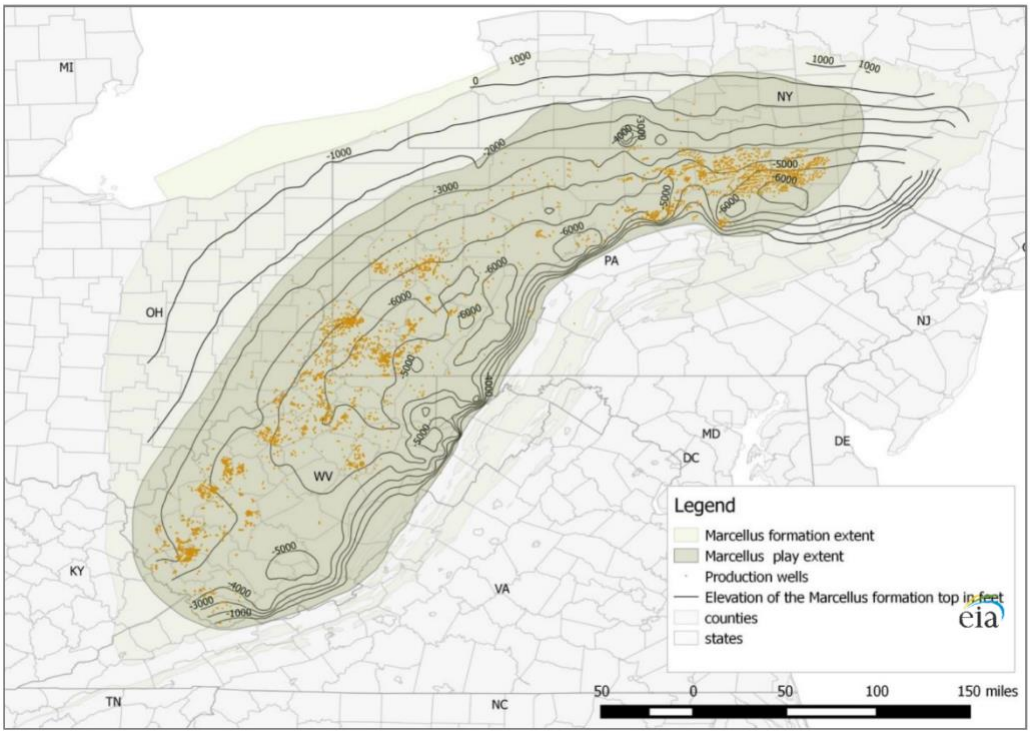

Figure 1.2. Structure map of Marcellus formation

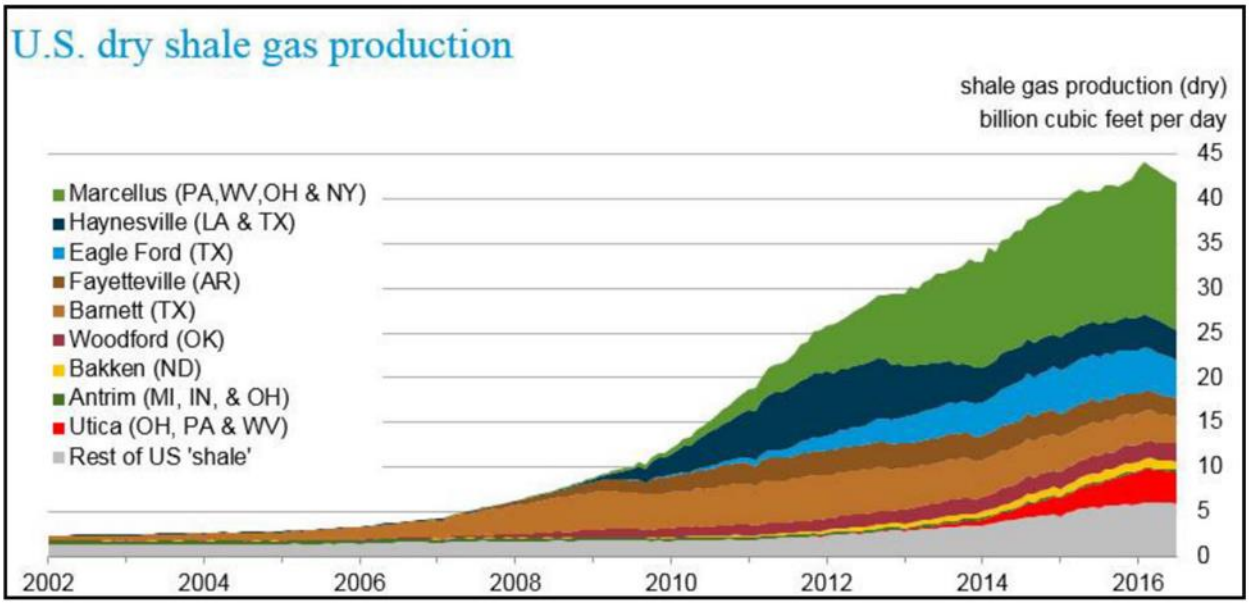

Figure 1.3. U.S. Energy Information Administration (EIA) official shale gas production data through July 2016.

1.3 MEMBRANE DISTILLATION

Desalination has emerged as a promising solution to address the world's water scarcity problem by removing dissolved salts from saline or brackish water, thus making it applicable for a number of water sources and uses [29, 30]. Membrane-based processes such as reverse osmosis (RO) and electrodialysis (ED) and thermal processes such as multi effect distillation (MED), multi stage flash (MSF), and mechanical vapor recompression (MVR) are the two main categories of commercial desalination technologies with RO and MSF accounting for 78% of the desalination capacity worldwide [31]. However, RO is limited to about 70,000 mg/l of total dissolved solids (TDS) in the feed as the hydraulic pressure required for RO systems can be up to 380 bar at the solubility limit of sodium chloride [32]. Among thermal based desalination technologies, membrane distillation (MD) shows the most promising performance for desalination of high salinity wastewaters [33]. Over the past two decades, there have been noticeable improvements in the design of membranes and technical performance of this technology [34]. Prior studies have shown that MD has the potential to achieve up to 99.9% of salt rejection [35-38] and 99.5% rejection of organic materials [39, 40]. These characteristics make MD one of the most promising technologies for treatment of high salinity wastewaters.

Membrane distillation operates at near ambient pressure and requires significantly lower capital investment [29]. Desalination of saline waters using different configurations of membrane distillation has been studied extensively [41-45]. With low operating temperatures, relatively low fouling propensity and lower energy requirements for pumping compared to pressure driven membrane processes, membrane distillation may be an attractive alternative for treatment of high salinity wastewaters. MD has been shown to be effective in removing heavy metals from wastewater [46] and concentrating radioactive waste [47] so that the concentrate could be disposed

safely. Direct Contact Membrane Distillation (DCMD), where both the hot feed and the recirculating cold permeate are in direct contact with the membrane, has been evaluated for desalination of sea water [35, 42, 48] as well as fruit juice concentration [49-51] and acid recovery [52].

1.4 RESEARCH OBJECTIVES AND THESIS LAYOUT

The current research aims to study the feasibility of membrane distillation to treat high salinity brines with an emphasis on understanding the fundamentals of the process. The work aims to: 1) study the effect of membrane fouling when treating real produced water brines while focusing on membrane selection from different commercially available hydrophobic microfiltration membranes; 2) validate the idea of using waste heat to drive membrane distillation for treatment of produced water through a case study in Pennsylvania; 3) develop a technique to probe the concentration profile of solute near the membrane surface; 4) evaluate the effect of different operating parameters on concentration polarization and validate the conventional approach of estimating concentration polarization effect through semi-empirical correlations.

The first chapter provides a brief introduction of produced water, its origin and current efforts to manage this challenging wastewater along with an introduction to membrane distillation. The research described herein is laid out in a chapter wise manner from Chapter 2 to 6, where the chapters are transcribed in standard research article format. Finally, a short summary covering the entire work is described in Chapter 7 followed by the future directions of this work in Chapter 8.

2.0 FOULING IN DIRECT CONTACT MEMBRANE DISTILLATION OF PRODUCED WATER FROM UNCONVENTIONAL GAS EXTRACTION

Hydraulic fracturing used for natural gas extraction from unconventional onshore resources generates large quantities of produced water that needs to be managed efficiently and economically to ensure sustainable development of this industry. Membrane distillation can serve as a cost effective method to treat produced water due to its low energy requirements, especially if waste heat is utilized for its operation. This study evaluated the performance of commercially available hydrophobic microfiltration membranes in a direct contact membrane distillation system for treating very high salinity (i.e., up to 300,000 mg/L total dissolved solids) produced water. Polypropylene and polytetrafluoroethylene membranes yielded the highest permeate flux with membrane distillation coefficient of 5.6 l/m^2/hr/kPa (LMH/kPa). All membranes showed excellent rejection of dissolved ions, including naturally occurring radioactive material (NORM), which is a significant environmental concern with this high salinity wastewater. Analysis of membranes after extended testing with actual produced waters revealed unevenly distributed inorganic deposits with significant iron content. A key finding of this study is that the iron oxide fouling layer had negligible effect on membrane performance over extended period of time despite its thickness of up to 12 μm. The results of this study highlight the potential for employing membrane distillation to treat high salinity wastewaters from unconventional gas extraction.

2.1 INTRODUCTION

The use of hydraulic fracturing techniques to extract oil and natural gas from different formations has been assessed since 1950s, while horizontal drilling has been used to produce oil since the early 1980s. These techniques were combined in the early 2000 to achieve successful large-scale natural gas productions from the Barnett Shale in Texas. Over the past few years, these technological advancements allowed access to vast quantities of natural gas from reservoirs that were previously considered uneconomical. In the United States, natural gas production increased from 0.3 trillion cubic feet in 2000 to 9.6 trillion cubic feet in 2012 [1] and it is projected that the US will become a net natural gas exporter by 2017 [2]. Despite these economic benefits, the extraction of oil and gas from unconventional reservoirs has potential drawbacks, including methane leaks [9, 53], contamination of surface waters [54] and production of highly contaminated wastewater [10, 55].

Water management has become a key issue for the future of this industry. During hydraulic fracturing, a mixture of water and chemicals known as fracturing fluid [9] is injected in a horizontal well to fracture the formation rock, increase its permeability and facilitate flow of oil and gas into the well. After the pumping pressure is relieved, some of the fracturing fluid mixed with the formation water returns to the surface. This water is typically designated as flowback water [10] and is collected over a period of 2-3 weeks with a total volume ranging from 10-40% of the fracturing fluid volume [11]. Wastewater continues to be produced throughout the lifetime of the well but at a rate that is much lower than during the flowback period. This wastewater is known as produced water [10] and is characterized by high concentration of total dissolved solids (TDS) and presence of organic compounds [12]. The composition of produced water depends on the well location and it varies during the lifetime of the well [13]. Currently, many of the shale plays rely

on underground injection for the disposal of flowback and produced water [56]. This option is increasingly being scrutinized by both public and regulatory agencies because it has been associated with seismic activity [24]. An alternative strategy is to develop desalination technologies for the recovery of clean water and valuable byproducts.

Reverse osmosis is the most studied desalination process in the past few decades [57] and accounts for about 61% of the world's capacity for seawater and brackish water desalination [58]. However, the hydraulic pressure required to use reverse osmosis can be up to 380 bar at the solubility limit of sodium chloride [32]. Membrane distillation operates at near ambient pressure and requires significantly lower capital investment [29]. Desalination of saline waters using different configurations of membrane distillation has been studied extensively [41-45]. With low operating temperatures, relatively low fouling propensity and lower energy requirements for pumping compared to pressure driven membrane processes, membrane distillation may be an attractive alternative for treatment of high salinity wastewaters. Due to low operating temperatures, MD could be employed using solar energy or waste heat to increase the temperature of the feed solution [59]. MD has been shown to be effective in removing heavy metals from wastewater [46] and concentrating radioactive waste [47] so that the concentrate could be disposed safely. Direct Contact Membrane Distillation (DCMD), where both the hot feed and the recirculating cold permeate are in direct contact with the membrane, has been evaluated for desalination of sea water [35, 42, 48] as well as fruit juice concentration [49-51] and acid recovery [52].

Several studies evaluated the use of MD to treat high salinity produced water from steam assisted gravity drainage process [60-62], oilfield produced water [63], coal seam gas produced water [64, 65] and produced water generated from natural gas exploration [66]. The feed water used in these studies had total dissolved solids (TDS) ranging from 4,000 to 70,000 mg/l and was

concentrated up to 230,000 mg/l [66]. Depending on the composition of feed water, the desired recovery factor and the heat source, the cost of produced water treatment using membrane distillation could range from 0.3 to 4.47 $/m^3 [60, 63]. However, none of the studies with oil and gas produced waters included a comparison of different hydrophobic membranes or discussed the potential for membrane fouling by inorganic deposits that are likely to form at high water recoveries and after a prolonged period of operation.

In this study, DCMD was evaluated for treatment of high salinity wastewaters from unconventional gas extraction. Initial screening of hydrophobic membranes to select the most promising ones in terms of mechanical stability and permeability also evaluated the key membrane parameters that affect its permeability. The morphology and composition of the inorganic deposit formed on the membrane surface when actual produced waters are concentrated up to halite saturation was assessed together with its impact on permeate flux and quality.

2.2 MATERIALS AND METHODS

2.2.1 DCMD experiments

All experiments were carried out in a countercurrent DCMD module with a flat sheet membrane. The membrane module was made of clear acrylic and could accommodate a flat sheet membrane with an effective area of 40 cm^2. The module includes two O-rings to seal the membrane that was supported by 2 mm thick spacers with porosity of 0.77 supplied by Delstar Technologies (Richland, PA).

The schematic diagram of the experimental system is shown in Figure 2.1. The feed solution was heated by a hot plate equipped with magnetic stirrer and supplied to one side of the DCMD module using a centrifugal pump (TE-5C-MD-115V March Pumps, Glenview, IL); flexible heating cable was also wound around the feed tank for additional heating capacity. Cool deionized water was circulated from the permeate tank on the other side of the membrane by centrifugal pump. Temperature of the cold water was maintained at a desired level using a stainless steel cooling coil that was immersed in the permeate tank and cooled by a 2.4 kW chiller (M75, Thermo Fisher Scientific Inc., Grand Island, NY). The overflow from the permeate tank was collected in a separate reservoir and tracked using a weighing balance (Ohaus Corp., Parsippany, NJ) while the permeate quality was continuously monitored using a conductivity probe (Thermo Fisher Scientific Inc., Grand Island, NY). A set of thermocouples (Type K, Tempco Electric Heater Corp., Wood Dale, IL) and pressure transducers (Series 628CR, Dwyer Instruments, Inc., Michigan City, IN) was used in conjunction with a data acquisition system (NI 9211 and NI 9207, National Instruments, Austin, TX) to continuously monitor the inlet and outlet temperatures and inlet pressures on both sides of the DCMD module. Feed and permeate flow rates were continuously monitored using flow meters (F-450, Blue-White Industries, Ltd., Huntington Beach, CA). It should be noted that the feed and permeate side velocities were maintained at 0.63 m/s (flow rate = 1.9 L/min) for all experiments conducted in this study. All pipes and fittings used in the system were made of high density polyethylene, polyvinyl chloride, nylon or tygon to avoid corrosion problems with metal parts when using high salinity solutions. Experimental results with both pure and saline water using the setup were found to be highly reproducible with a maximum standard deviation in permeate flux of ± 1 LMH.

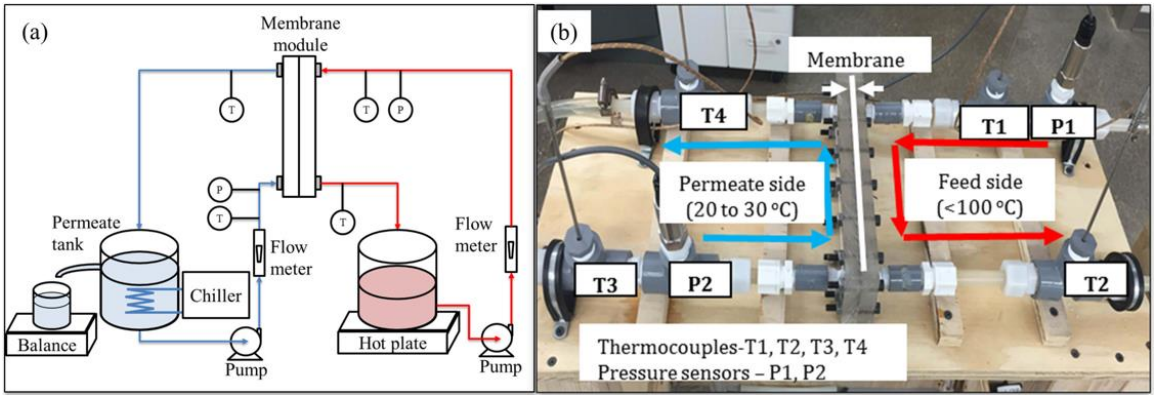

Figure 2.1. (a) Schematic diagram of the DCMD setup, (b) Bench scale DCMD module.

2.2.2 Membranes

Acrylic copolymer with a nylon support (AC), polytetrafluoroethylene with polyester support (PTFE 2), polytetrafluoroethylene with polypropylene support (PTFE 3) and polyvinylidene fluoride (PVDF) membranes were purchased from Pall Corporation (Port Washington, NY), while polypropylene (PP) and polytetrafluoroethylene with polypropylene support (PTFE 1) were purchased from Sterlitech Corporation (Kent, WA). The average thickness of each membrane was evaluated using scanning electron microscopy (SEM) (JEOL JSM6510, Peabody, MA). The membranes were first frozen using liquid nitrogen and cut with a sharp blade. The SEM was used to measure the cross section at 10 different points to determine the average thickness of each membrane. Contact angle was measured using a goniometer (VCA 2000 contact angle goniometer, AST Products Inc., Billerica, MA) and a sessile drop method (contact angle for a 10µl drop was measured at three different sites for each membrane).

Dry and wet gas permeation tests [67, 68] were used to obtain the mean pore size of the membranes and their porosity (ε) was evaluated according to the method suggested by Smolders and Franken [69] where test with isopropyl alcohol was used to calculate the density of the polymer

and test with deionized water was used to calculate the overall density of the membrane. The membrane porosity (ε) was then calculated as

$$\boldsymbol{\varepsilon = 1 - \frac{density\ of\ membrane}{density\ of\ polymer}} \quad (1\text{-}1)$$

Thermal conductivity was measured based on the laser flash technique using NETZSCH 467 HyperFlash instrument according to Method ASTM E1461-13 [70]. The properties of hydrophobic membranes used in this study are summarized in Table 2.1.

Table 2.1. Properties of the membranes used in this study

Membrane	**Mean pore size (μm)**	**Thickness (μm)**		**Contact angle (active layer)**	**LEP (psi)**	**% Porosity of membrane**		**Thermal Conductivity (W/mK)**
		Total	Active layer			Bulk	Active layer	
AC	0.23	215 ± 18	-	135 ± 4.7	23.7 ± 0.5	30 ± 3.1	-	0.105
PP	0.38	135 ± 5	-	136 ± 1	32 ± 1.7	79 ± 1.8	-	-
PTFE 1	0.21	112 ± 17	20 ± 4	142 ± 2.1	40.3 ± 0.5	42 ± 0.5	92 ± 1.7	0.294
PTFE 2	0.25	210 ± 12	-	147 ± 3.8	37 ± 1	37 ± 1.8	-	-
PTFE 3	0.24	148 ± 30	60 ± 5	149 ± 3	15.5 ± 1.9	60 ± 6.8	94 ± 1.3	0.242
PVDF	0.19	145 ± 3	-	107 ± 1.4	14.2 ± 0.7	68 ± 5	-	-

2.2.3 Produced water

Produced water samples were obtained from sites in the Marcellus Shale region in Pennsylvania. Site 1 was located in Tioga County while Sites 2 and 3 were located in Washington County. Prior to characterization, produced water samples from these sites were pretreated by filtration through 0.22 μm membrane to remove suspended solids. The TDS was determined using EPA gravimetric method (EPA Method 160.1). Concentration of chloride as the main anion was determined using Dionex ICS-1100 ion chromatography (IC) system (Dionex, Sunnyvale, CA) with the IonPac AS22 Carbonate Eluent Anion-Exchange Column. Concentrations of cations (except Fe) were analyzed using the same equipment with IonPac CS12A Cation-Exchange Column. The total iron content was measured using the colorimetric test (Hach Method 10249, Loveland, CO).

Total organic carbon (TOC) was analyzed using GE Sievers InnovOx Laboratory TOC Analyzer (General Electric, Boulder, CO) while Radium 226 activity was measured using gamma spectrometer with high purity germanium detector (GEM15P4-70, ORTEC, Oak Ridge, Tennessee). For Ra226 analysis, 10 ml of each sample was filtered through 0.22 μm membrane and heated at 105^{o}C to evaporate the liquid. Residual solids were crushed and spread evenly across a 46-mm Petri dish that was then sealed with vinyl tape and analyzed using gamma spectrometer at 186 keV with 24-hr counting period [71, 72].

The feed water quality assessed according to the methods described above is shown in Table 2.2. The TDS in produced water samples obtained for this study ranged from 92,800 to 308,300 mg/l. These samples also contained significant Ra 226 concentration and fairly low TOC. It should be noted that all produced waters used in this study had no detectable sulfate

concentration, the presence of which could potentially foul the membrane due to precipitation of sulfates of calcium, barium and strontium at high water recoveries [73, 74].

The morphology and composition of solids deposited on the membrane surface after DCMD experiments with actual produced waters was analyzed using scaning electron microscopy (SEM) and energy dispersive spectroscopy (EDS) (JEOL JSM6510, Peabody, MA).

Table 2.2. Composition of produced water samples

Component (mg/L)	Site 1	Site 2	Site 3
Cl^-	188,728	63,588	165,580
Na^+	81,442	26,427	42,650
NH_4^+	1,002	279	-
K^+	786	258	209
Mg^{+2}	2,664	675	1,715
Ca^{+2}	32,901	6,523	26,507
Sr^{+2}	11,910	1,620	3,544
Ba^{+2}	6,256	3,743	-
Fe total	30	10	91
TDS	308,300	92,800	240,296
TOC	0	11	19
***Ra226**	17,980 ± 1,100	753 ± 60	3,561 ± 328
pH (no units)	2.9	7	5.4

*Ra226 concentration is expressed in pCi/l

2.3 RESULTS AND DISCUSSION

2.3.1 Short term experiments

The performance of six membranes selected for this study was evaluated in DCMD module using actual produced water from unconventional gas well as feed. Initial screening of these membranes was carried in a constant concentration mode where the feed concentration was maintained at a constant level by recycling the permeate back to the feed reservoir. Testing in a constant concentration mode was performed for a period of 3 hours with produced water from Site 1 (Experiment 1). As shown in Figure 2.2(a), the permeate flux remained constant throughout the experiment. The permeate flux obtained in this study is higher than that reported by Adham et al. [75] for PTFE membrane and Criscuoli et al. [76] for PP membrane under similar experimental conditions. Figure 2.2(b) shows a correlation between the steady-state permeate flux and MD coefficient obtained with pure water experiments by a method described in literature [77]. As can be seen from Figure 2.2(b), the MD coefficient obtained using pure water feed can adequately predict relative membrane performance even when treating extremely high salinity water. PP membrane had the highest MD coefficient due to large pore size (i.e., 0.38 μm) and high porosity (i.e., 79%). PVDF membrane had low MD coefficient in spite of having high porosity (i.e., 68%). This could be explained by slightly lower mean pore size compared to other membranes as well as a very thick active layer. Unlike the PTFE membranes used in this study, which had an active layer thickness of 20-60 μm, the PVDF membrane was unsupported and the active layer itself was 145 μm thick. As the active layer is usually the mass transfer limiting layer, a thick active layer would decrease the flux significantly and hence decrease the MD coefficient. The three PTFE membranes exhibited significant

differences in MD coefficient. The PTFE 2 membrane has a support made of non-woven polyester with almost twice the thickness of the other PTFE membranes and low porosity of 37%. Although the thickness of active layer for PTFE 3 is about three times that of PTFE 1, PTFE 3 exhibited higher MD coefficient because it had about 50% higher bulk porosity and about 14% larger pore size. The higher bulk porosity of PTFE 3 is attributed to the high porosity of its support since the porosities of active layers of PTFE 1 and PTFE 3 are similar. These results suggest that the membrane support plays an important role in the performance of MD system and that a highly porous support should be considered when selecting membranes for this application. These findings are in agreement with a previous study [78] that discussed how the properties of the support layer can add additional resistances in series with the active layer and hence affect the flux.

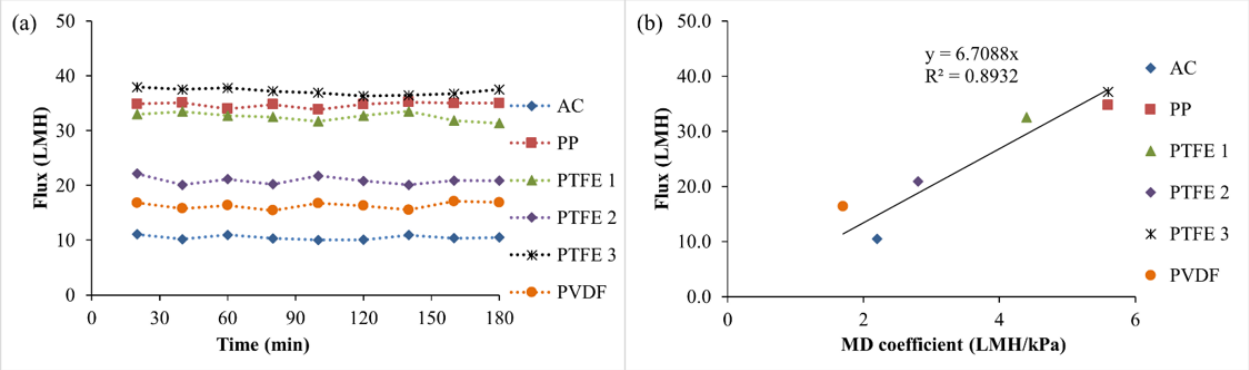

Figure 2.2. (a) Permeate flux in DCMD module treating produced water from Site 1 in a constant concentration mode [feed flow rate = 1.9 L/min (Re = 740), permeate flow rate = 1.9 L/min (Re = 2100)], feed inlet temperature = 60 ºC, permeate inlet temperature = 30 ºC); (b) Steady-state permeate flux as a function of pure water MD coefficient.

The salt rejection for DCMD experiments was determined based on chloride and Ra 226 concentrations in the permeate. As can be seen from Table 2.3, the infiltration of chloride ions

from the feed solution was negligible while Ra 226 in permeate water was not detectable. These results demonstrate the ability of DCMD to provide stable fluxes and excellent rejections of ions in spite of extremely high dissolved solids content of the feed; permeate water also showed no presence of Ra266, which is a significant health and environmental concern with produced water. Analysis of the six membranes with SEM (not shown) revealed that no fouling had occurred during three hours of operation. It could be argued this may not be sufficient operating time to observe the effects of membrane fouling. Hence, long term experiments were performed and the results are discussed in the next section. The PP membrane exhibited one of the highest permeate fluxes among the membranes tested in this study but the membrane would tear during experiments. Hence, PTFE membranes (PTFE 1 and PTFE 3) were used for further experiments.

Table 2.3. Permeate quality during tests in constant concentration mode with Site 1 produced water

Membrane	Cl^- (ppm)	Rejection %	Average Flux (LMH)
AC	2	99.9	10.5
PP	7	99.9	34.7
PTFE 1	0.5	99.9	32.5
PTFE 2	1	99.9	20.8
PTFE 3	2	99.9	37.5
PVDF	1	99.9	16.3

DCMD experiments with produced water from Site 2 (Experiment 2) were conducted without returning the permeate to the feed tank until the TDS on the feed side reached 270,000 mg/L (Figure 2.3), which corresponds to water recovery of 66%. A decrease in the permeate flux

shown in Figure 2.3 can be attributed to vapor pressure lowering of the feed solution due to the increase in salt concentration. The predicted flux in Figure 2.3 was calculated using the APSEN Plus model developed for this system where the membrane surface temperatures were estimated using the procedure described by Yun et al. [79] and then used to obtain the corresponding vapor pressures and associated permeate flux based on the MD coefficients. Hence, the temperature polarization effects were taken into account when predicting the DCMD flux. Excellent agreement between measured and predicted permeate flux is evident during the early stages of these experiments while some discrepancy is observed towards the end of the experiment when the feed TDS exceeded about 200,000 mg/L. This discrepancy can be attributed to either membrane fouling or concentration polarization since the temperature polarization effects are already included in the predictive model. This issue will be further discussed in the section that offers the analysis of the fouling layer. As shown in Table 2.4, both PTFE membranes showed excellent rejections of chloride, TOC and Ra226.

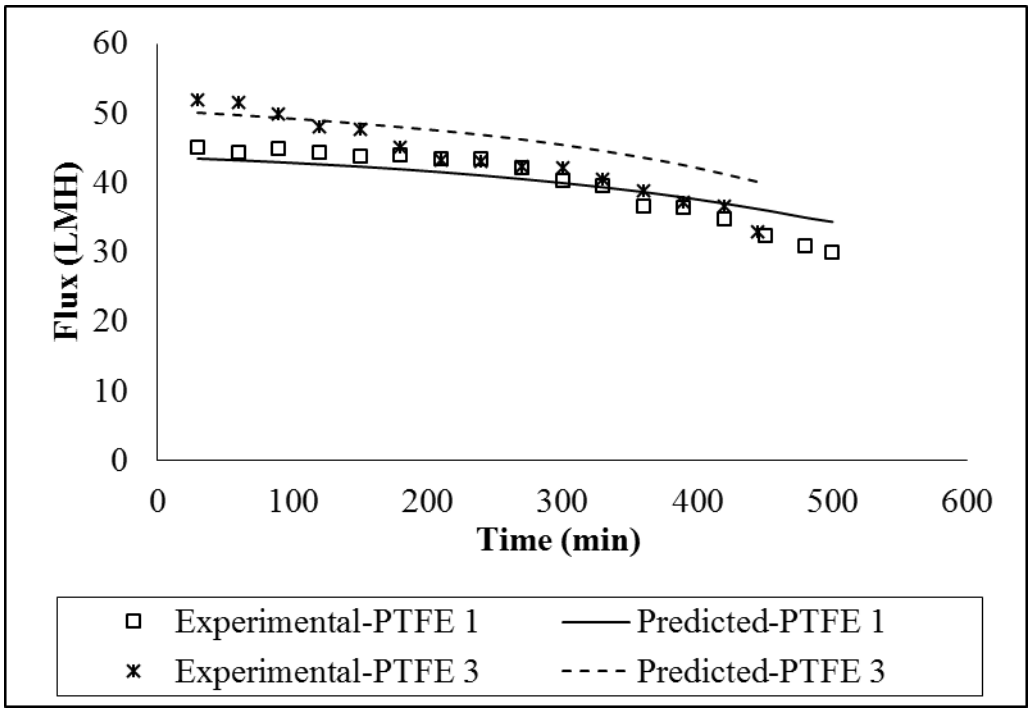

Figure 2.3. Permeate flux for PTFE 1 and PTFE 3 membranes treating produced water from Site 2 until the feed concentration reached 270,000 mg/L TDS (feed flow rate = 1.9 L/min (Re = 2,220 at the beginning and 900 at the end of the experiment), permeate flow rate = 1.9 L/min (Re = 2,100), feed inlet temperature = 60 ºC, permeate inlet temperature = 30 ºC).

Table 2.4. Permeate quality during concentration tests with Site 2 produced water (Experiment 2)

		PTFE 1	**PTFE 3**
Cl^-	Conc. (mg/L)	0.4	0.5
	Rejection (%)	99.9	99.9
Ra 226	pCi/L	ND	ND
TOC	Conc. (mg/L)	1	0.83
	Rejection (%)	90.9	92.4

The specific thermal energy consumption of the DCMD system was calculated using the procedure described by Criscuoli et al. [76] which involved adding energy required for heating the feed stream and energy required for cooling the permeate stream. The thermal efficiency of separation, which is the same as gain output ratio (GOR) for a system that does not include heat recovery, is defined as the ratio of thermal energy utilized for water evaporation to the total heat flux across the membrane [80]. The specific thermal energy consumption for PTFE 1 during this experiment increased from 2.6 kWh/kg at the beginning of the experiment (feed TDS = 92,800 mg/L) to 3.7 kWh/kg at the end (feed TDS = 270,000 mg/L), while the thermal efficiency of separation decreased from 51% to 35%. Similarly, the specific thermal energy consumption for PTFE 3 increased from 2.1 kWh/kg to 3 kWh/kg while the thermal efficiency of separation decreased from 62% to 46%. It should be noted that the energy required to heat the feed stream would be 50% of the specific energy requirement reported above as the heat loss to the environment in the system was negligible. The change in specific thermal energy consumption and thermal efficiency of separation is attributed to the flux decline due to vapor pressure decrease of the feed solution as the salt concentration in the feed increased. The permeate flux decrease with an increase in feed salinity decreases the contribution of latent heat to the total energy consumption because the conductive losses remain fairly constant regardless of the feed solution composition. The lower thermal efficiency of PTFE 1 membrane when compared to PTFE 3 can be attributed to a slightly higher thermal conductivity as well as lower thickness of PTFE 1 membrane (Table 2.1), which lead to higher conduction losses and lower thermal efficiency. These results also indicate that the DCMD performance with respect to thermal efficiency and specific energy consumption is affected significantly at such high salinities. The specific energy consumption

obtained in this study with produced water was comparable to that reported by Criscuoli et al. [76] for pure water.

2.3.2 Long term experiments

Short term experiments discussed above are crucial to evaluate DCMD performance in terms of energy requirements and thermal efficiency but cannot be used to assess the membrane fouling propensity. Therefore, long term experiments were carried out with produced water from Site 1 and Site 3 using PTFE 1 membrane under identical experimental conditions as in Experiments 1 and 2.

A constant concentration test similar to Experiment 1 was carried out for 48 hours to assess DCMD performance with the high salinity produced water from Site 1 (Experiment 3). During this test, the feed water was replaced after 24 hours to provide additional scaling constituents on the feed side. As shown in Figure 2.4(a), the permeate flux remained constant during the 48-hour period without any deterioration in permeate quality. The concentration of chloride in the permeate at the end of the experiment was 0.2 mg/l, while Ra226 was not detectable, which corresponds to 99.99% rejection of dissolved solids.

An experimental setup with the schematic shown in Figure 2.5 was used to simulate a continuous process for DCMD (Experiment 4). In this process, the feed concentration was maintained by regulating the flow rate of the feed makeup stream. A peristaltic pump was used to control the feed makeup flow, while an overflow purge stream continuously removed a fraction of the feed solution to prevent excessive accumulation of dissolved solids in the feed tank. Such a continuous process would be used to treat saline wastewater in actual DCMD treatment plant. Produced water from Site 3 was used for this experiment after diluting it to 80,000 mg/l TDS as

the dissolved solids originally present in this water were close to halite saturation limit. Initially, the feed water at 80,000 mg/l was concentrated to 300,000 mg/l, which required about 30 hours. When the concentration of the feed reached 300,000 mg/l, the feed makeup and purge streams were used to maintain the concentration in the feed tank at 300,000 mg/l for another 42 hours (the total duration of this experiment was 72 hours). As seen in Figure 2.4(b), the permeate flux obtained during the experiment was stable once the concentration of dissolved solids in the feed tank reached 300,000 mg/l. It is important to note that the permeate flux in Experiments 3 and 4 was almost identical (i.e., ~30 LMH) as the TDS in the both feed stream was also identical (i.e., 300,000 mg/L). The fact that the permeated flux in these long-term experiments was identical to the one obtained in a short-term experiment (Experiment 1) suggests the absence of any membrane fouling with the produced water from Site 1. During the course of this experiment, the concentration of chloride ions in the permeate reached 0.3 mg/l with no detectable levels of Ra226. The dissolved solids rejection at steady-state was 99.99% while the TOC levels in the permeate reached 4 mg/l, which corresponds to a TOC rejection of 78.9%. During the 72-hour experiment, MD was able to concentrate 13.2 liters of feed at a TDS of 80,000 mg/l to 300,000 mg/l (i.e., water recovery of 73%) with just 40 cm^2 of membrane without any degradation in permeate flux and its quality.

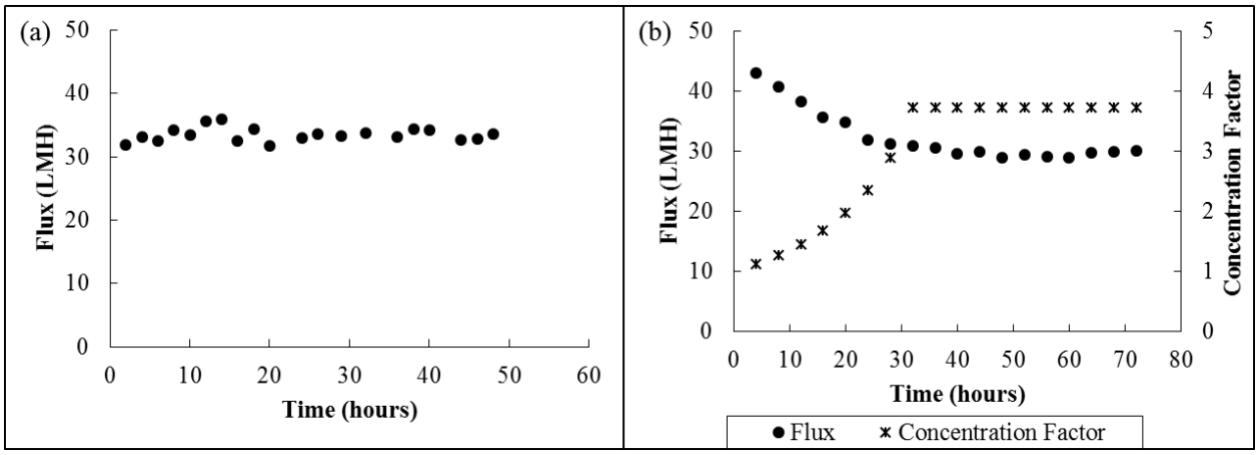

Figure 2.4. Variation of permeate flux with time in (a) Experiment 3 and (b) Experiment 4.

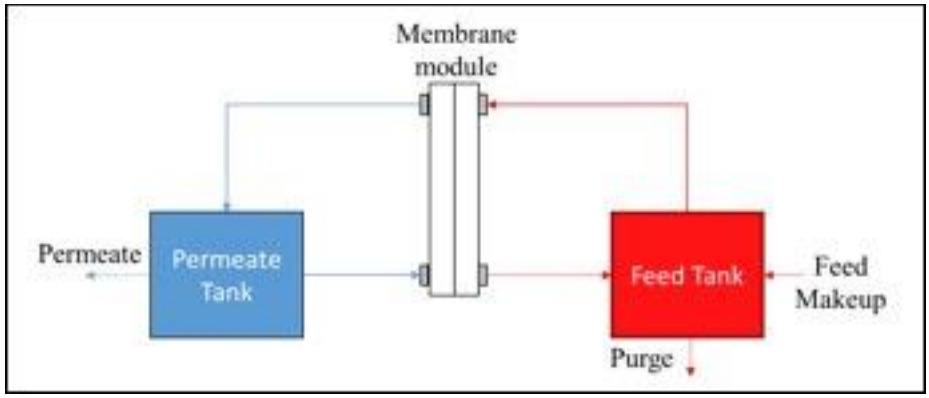

Figure 2.5. Schematic representation of flow diagram for continuous treatment of produced water using DCMD.

2.3.3 Membrane fouling

The results from Experiments 1 and 3 (Figures 2.2 and 2.4) suggest that there was no membrane fouling in those experiments as the trans-membrane flux remained constant during experiments with very high salinity produced water from Site 1. However, a significant flux decline in the short term Experiment 2 suggests that the membrane may be fouled by the produced water from Site 2. Permeate flux decline was also observed in the long term Experiment 4 (Figure 2.4(b)). However, the results shown in Figure 2.4(b) indicate that even if there was any membrane

fouling due to scale formation, the build-up of the scale layer was limited because the permeate flux remained constant during the last 48 hours of the experiment. To analyze the effect of fouling on membrane performance, dry gas permeation tests were carried out with the membranes used in these experiments and compared with the results obtained with pristine membranes. The results shown in Figure 2.6 reveal that the gas flux for membranes used in Experiments 2, 3 and 4 was almost identical to that observed for pristine membranes, indicating that the membrane permeability was not altered by treating the produced water.

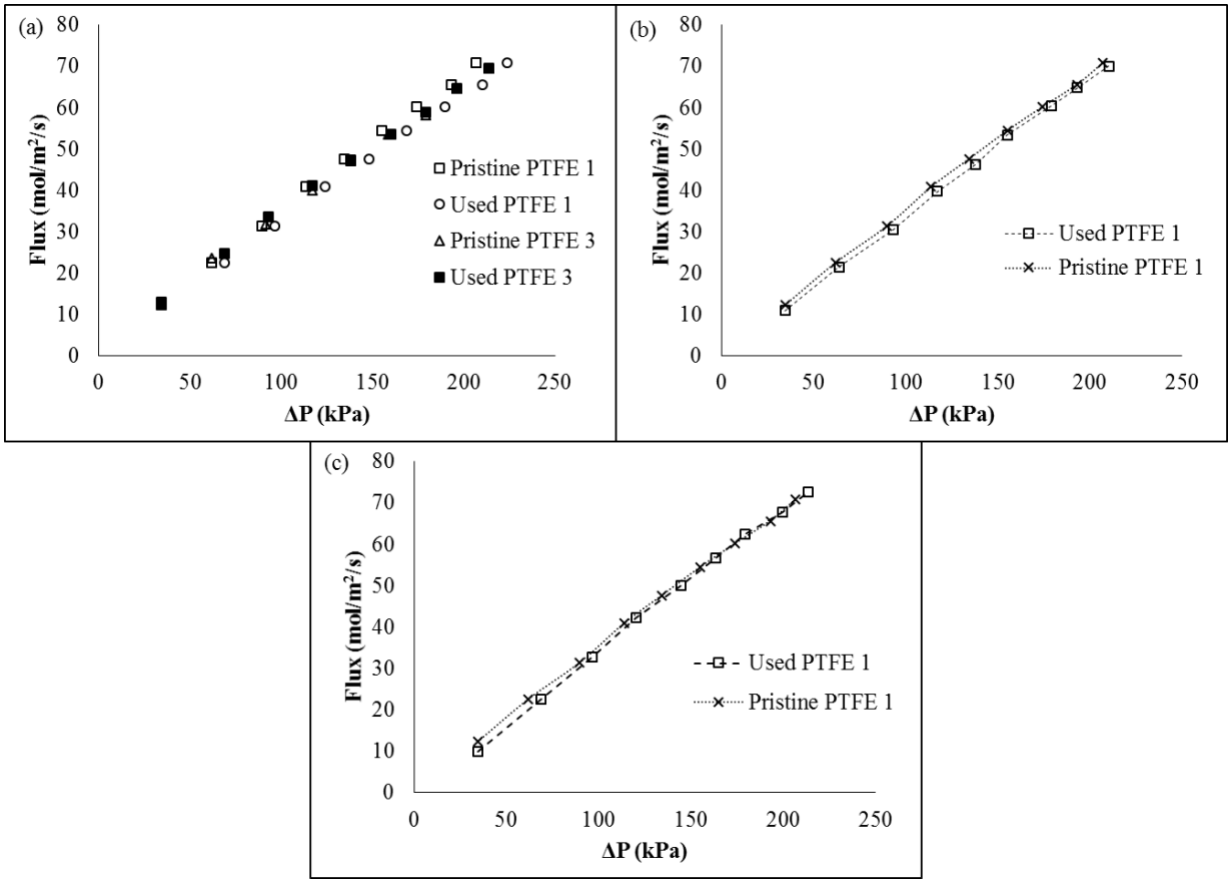

Figure 2.6. Gas permeation flux as a function of pressure difference across the membranes used for (a) Experiment 2, (b) Experiment 3 and (c) Experiment 4.

To further support this conclusion, PTFE membranes used in Experiments 2, 3 and 4 were tested for pure water permeability at a feed temperature of 60 ^{o}C (feed flow rate = 1.9 l/min, Re = 2860) and permeate temperature of 30 ^{o}C (permeate flow rate = 1.9 l/min, Re = 2100). In all cases, the permeate flux obtained with used membranes was identical to that previously determined for pristine membranes (data not shown). Moreover, the flux measured in Experiment 3 was almost identical to the flux obtained when pure NaCl solution with the same TDS content was used as feed where no scaling was observed because the feed was maintained below the halite saturation limit. This confirms that the PTFE membranes used in the experiments with produced water were not fouled and that the flux decline observed in these experiments was due to the increase in the salinity of the feed and a corresponding reduction in vapor pressure.

Based on the results discussed above, it can be concluded that the discrepancy between observed and predicted flux for both PTFE 1 and PTFE 3 membranes shown in Figure 2.3 can only be attributed to concentration polarization effects as temperature polarization was accounted for in the model used to predict permate flux. The discrepancy between predicted and observed flux at the very end of Experiment 2 corresponds to a concentration polarization factor (c_m/c_b) of 1.31 for PTFE 1 and 1.27 for PTFE 3 membrane. On the other hand, the temperature polarization factor, $(T_{m,f}-T_{m,p})/(T_{b,f}-T_{b,p})$, increased from 0.73 to 0.76 for PTFE 1 membrane and from 0.66 to 0.70 for PTFE 3 membranes throughout these experiments, which has much smaller impact on permeate flux compared to concentration polarization. Limited increase of the temperature polarization factor was also observed in the case of flat sheet PTFE membranes when NaCl solutions up to 1.67 M were used to study the temperature and concentration polarization effects [81]. The membrane surface temperatures were calculated by the method given by Yun et al. [79], which uses fundamental heat transfer equations together with empirical Nusselt number

correlations developed by Phattaranawik et al. [77]. These findings suggest that the concentration of salts at the membrane surface can be about 30% higher than that in the bulk, which can have significant impact on permeate flux but was previously neglected when analyzing MD performance [81-83].

The SEM images of membranes used in experiments with produced water (Figure 2.7) reveal the distribution of inorganic deposits that were formed on the membrane surface. Dark patches represent the membrane section where salt deposition occurred, whereas the light grey areas represent clean membrane sections with no deposits. The composition of the solids that accumulated on the surface of the membrane was determined by EDS analysis and is shown in Table 2.5.

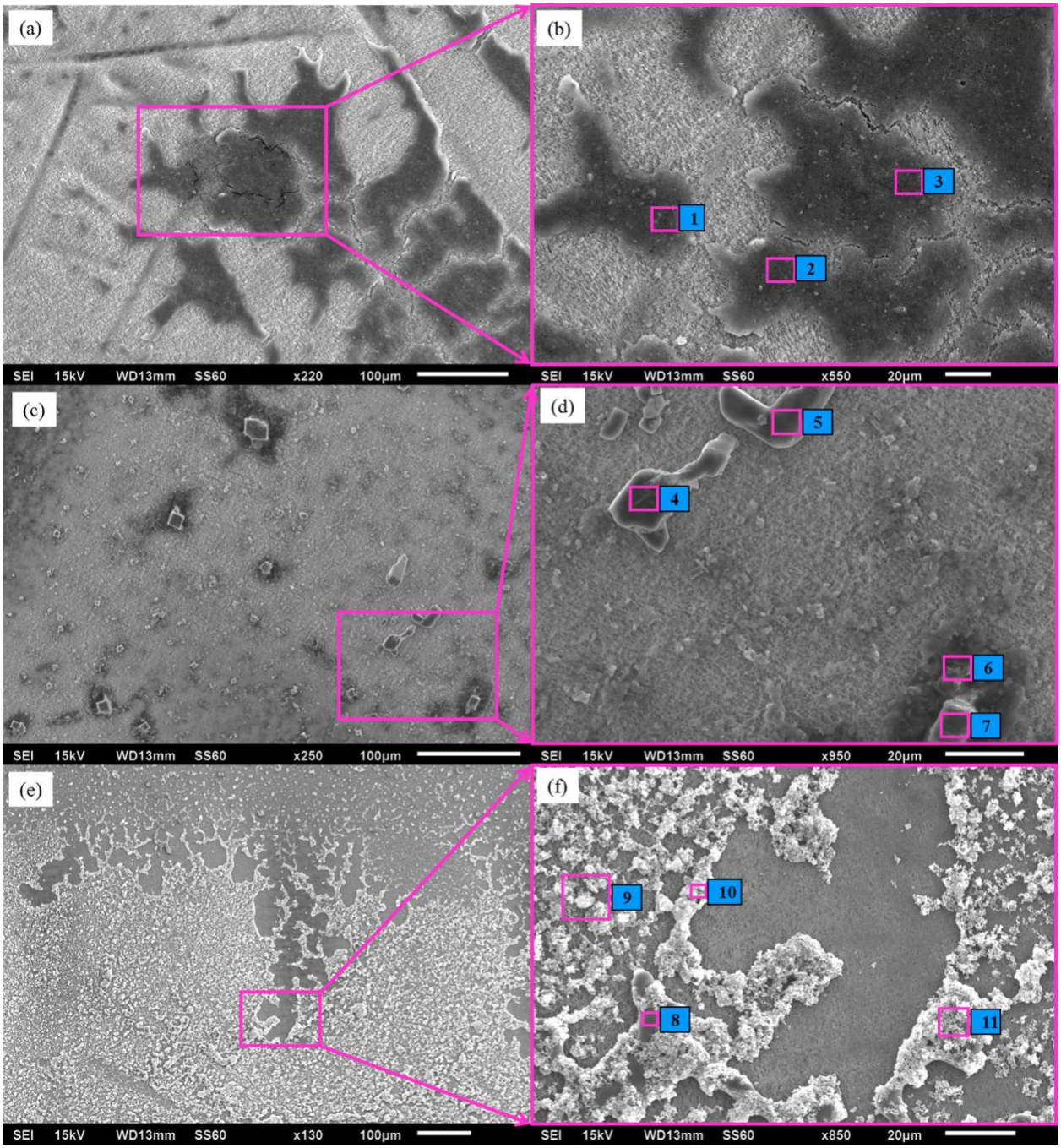

Figure 2.7. SEM images of PTFE 1 membrane used for (a-b) Experiment 2, (c-d) Experiment 3 and (e-f) Experiment 4.

Table 2.5. Elemental analysis of scales formed on the PTFE 1 membranes shown in Figure 2.7.

Location	Weight %							
	O	Na	Mg	Cl	Ca	Fe	Sr	Ba
1	41	2	1	3	2	45	0	7
2	38	2	1	4	3	50	0	3
3	44	2	0	3	2	44	0	5
4	1	27	0	68	2	1	0	0
5	0	38	0	62	0	0	0	0
6	25	1	2	41	7	13	3	8
7	0	38	0	62	0	0	0	0
8	2	38	0	59	0	1	0	0
9	36	1	1	16	6	38	1	0
10	36	1	1	15	6	41	1	0
11	19	23	0	31	1	27	0	0

Distinct crystals shown in SEM images were identified as predominantly sodium chloride. Moreover, the presence of iron in the accumulated scale was quite significant considering the fairly low concentrations of iron in the feed solution (Table 2.2). As can be seen from the elemental analysis at locations 1, 2, 3, 6, 9 and 10 in Table 2.5, iron oxide is most likely the dominant form of iron formed on the membrane surface. Theoretical calculations with PHREEQC chemical speciation software and the bulk composition of feed solution showed that only iron based compounds (i.e., goethite, hematite and magnetite) achieved positive saturation indices under the experimental conditions evaluated in this study (data not shown). While goethite and hematite are

both very stable forms of iron oxide [84, 85], the lower pH of produced water studied in this work is likely to favor goethite precipitation [86, 87]. Hence it is reasonable to assume that goethite is the dominant form of iron deposited on the membrane surface under the experimental conditions evaluated in this study. It must be noted that halite was fairly close to saturation at bulk feed composition (i.e., saturation index close to zero) and it is very likely that the concentration polarization on the feed side was responsible for the detection of halite in these scales (Table 2.5). Gryta [85] reported that iron oxide has a porous structure and limited impact on membrane permeability even after 20 hours of operation. Hausmann et al. [88] also suggested that MD fouling by whey had a much less impact on the permeate flux then fouling by skim milk because of the higher porosity of the fouling layer. Similarly, the porous nature of the scale layer is likely responsible for the negligible impact on membrane permeability observed in this study. In addition, the scale layer did not have enough coverage on the membrane surface to significantly affect the permeate flux. Figure 2.8 shows the thickness of deposits formed on PTFE 1 during long-term treatment of produced water from Site 3 (Experiment 4). The thickness of the deposits on the membrane surface ranged between 6 - 12 μm, while that for the membrane used in Experiment 2 was less than 1 μm (data not shown). However, the permeate flux observed for PTFE 1 membrane in Experiments 2 and 4 were almost identical at the same feed concentration. This further supports the hypothesis that the iron oxide scale formed on the membrane surface did not affect the permeate flux. The membrane used in Experiment 3 showed negligible fouling when compared to other membranes because of the low pH of the feed water, which prevented iron oxide formation.

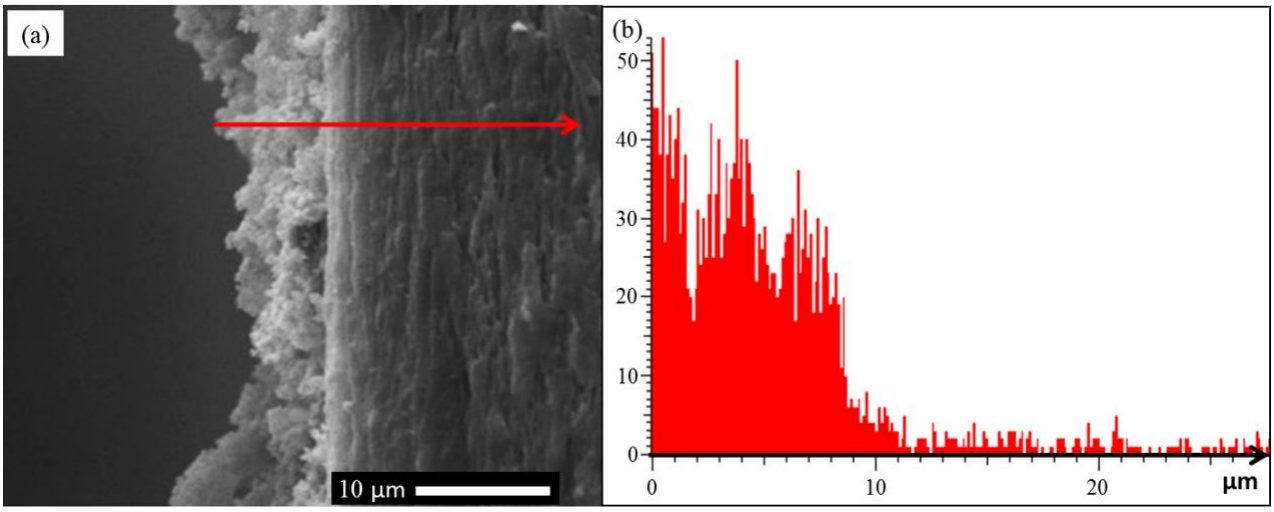

Figure 2.8. SEM image showing (a) the cross section of the membrane at the feed side with the scale layer formed during Experiment 4; (b) EDS line scan to evaluate the thickness of the scale layer. The y-axis shows the intensity of iron content while the x-axis shows the distance in µm.

2.4 CONCLUSIONS

The potential of DCMD to treat very high salinity produced water from unconventional onshore natural gas extraction was assessed in this study. Initial screening of commercially available hydrophobic membranes was carried out to identify those with high permeabilities suitable for this challenging application. The MD coefficients of the membranes evaluated in this study were significantly higher than those previously reported in the literature and the PTFE membranes used in this study exhibited substantially higher flux than that reported before for feed waters with a fairly high TDS content [63]. It was found that the properties of the membrane support layer (e.g., thickness and porosity) greatly influence the permeate flux and that highly porous support should be considered when selecting membranes for DCMD.

The membranes used in this study showed excellent rejection of ions, including radioactive Ra226 and organic compounds. While temperature polarization had minimal effect on membrane performance, concentration polarization had a major impact on permeate flux at high salinities, which was previously neglected when analyzing MD performance. This study revealed that iron-based deposits formed on the membrane surface even with relatively low concentrations of iron in the feed. However, the iron oxide scale layer, which had a thickness of 6-12 μm, had negligible impact on membrane performance even after 3 days of operation at an extremely high TDS of 300,000 mg/l. The results obtained in this study indicate that DCMD can prove as a robust technology for treatment of high salinity wastewaters to produce almost pure water with minimal membrane fouling.

3.0 INTEGRATING MEMBRANE DISTILLATION WITH WASTE HEAT FROM NATURAL GAS COMPRESSOR STATIONS FOR PRODUCED WATER TREATMENT IN PENNSYLVANIA

Direct contact membrane distillation (DCMD) has immense potential in the desalination of highly saline wastewaters where reverse osmosis is not feasible. This study evaluated the potential of DCMD for treatment of produced water generated during extraction of natural gas from unconventional (shale) reservoirs. Exhaust stream from Natural Gas Compressor Station (NG CS), which has been identified as a potential waste heat source, can be used to operate DCMD thereby providing economically viable option to treat high salinity produced water. An ASPEN Plus simulation of DCMD for the desalination of produced/saline water was developed in this study and calibrated using laboratory-scale experiments. This model was used to optimize the design and operation of large scale systems and estimate energy requirements of the DCMD process. The concept of minimum temperature approach used in heat exchanger design was applied to determine the optimum membrane area for large scale DCMD plants. Energy analysis revealed that the waste heat available from NG CS is sufficient to concentrate all the produced water generated in Pennsylvania to 30 wt.% regardless of its initial salinity.

3.1 INTRODUCTION

Marcellus Shale is a major natural gas (NG) reservoir with steadily increasing production since 2008 that currently accounts for about 40% of the total U.S. shale gas production [16]. Natural gas extraction from Marcellus shale in Pennsylvania, West Virginia and Ohio is accompanied by large amounts of produced water that contains high total dissolved solids (TDS). Future extraction of shale gas requires economical management of wastewater to minimize potential environmental impacts. Produced water injection into Class II Underground Injection Control (UIC) wells is the dominant management alternative in many shale plays with sufficient disposal capacity [10, 18, 19]. In the Marcellus shale region, the average cost of produced water transportation from the well site in Pennsylvania to injection wells in Ohio or West Virginia ranges from 10 to 20 $/barrel (bbl) [21, 22]. In addition, the costs associated with deep well injection is estimated at $1/bbl [21]. However, while there is a total of 12,000 Class II saline water disposal wells in Texas, only 8 such wells are currently available in Pennsylvania [89]. Lack of sufficient disposal capacity in Pennsylvania requires the development of alternative approaches for management of high TDS produced water [23]. Recent studies have documented concerns over induced seismic activities due to deep well injection [24-27], further emphasizing the need for the development of innovative management strategies for produced water to avoid unintended environmental consequences.

Among different wastewater treatment technologies, emerging membrane distillation (MD) process is particularly attractive because of its low capital investment, low operating temperature, and thus the ability to operate using low grade (waste) heat. MD is a vapor pressure driven process that has been known for over four decades. The first MD patent was filed in 1963 by Bodell [90], while the first paper was published in 1967 by Findley [91]. Direct contact membrane distillation (DCMD) is the most commonly studied MD configuration in which a

hydrophobic micro-porous membrane is in direct contact with a hot feed stream on one side and a cold recirculating permeate stream on the other. The volatile vapors from the feed side traverse across the membrane and are condensed on the permeate side. The nonvolatile compounds in the feed stream, such as salts, suspended solids, and macromolecules are retained in the feed solution due to the hydrophobic nature of the membrane. The permeate solution will be free from impurities as long as the membrane is not wetted [92, 93] and as long as there are no volatile contaminants in the feed stream that can permeate across the membrane.

DCMD is a non-isothermal separation process that involves simultaneous heat and mass transfer and operates on the principle of vapor-liquid equilibrium. In the last decade, researchers have developed several predictive models for DCMD systems by combining heat and mass transfer principles [79, 94-98]. Heat transfer models comprise of Nusselt number-based empirical correlations to evaluate the heat transfer coefficients [77, 99, 100], while mass transfer is typically expressed as a linear function of the vapor pressure difference across the membrane [99-102]. Moreover, different types of heat recovery approaches have been described in the literature [80, 103-106] to recover the energy lost to the permeate side stream from the feed stream and increase the overall energy efficiency of the process. DCMD is being explored for diverse applications such as desalination of water, concentration of aqueous solutions in the food industry and concentration of acids [50-52, 107, 108]. MD processes are able to distill water at operating temperatures of 30-90^{o}C, which is significantly lower than the conventional thermal treatment processes. The lower operating temperature of MD also offers an excellent opportunity to integrate MD processes with waste heat sources to further reduce the operating cost. Furthermore, MD operates at lower hydrostatic pressure compared to conventional pressure-driven membrane technologies, such as reverse osmosis and nano-filtration [109]. Membrane distillation has been evaluated for

desalination of seawater and brine from thermal desalination plants in pilot-scale studies [75, 110-112], but the commercialization of this technology is hindered by high energy cost [113]. Kesieme et al. [29] estimated that the MD treatment cost decreased from \$2.2/m^3 to \$0.66/m^3 when a waste heat source was employed to drive the process. In comparison, the operating cost of reverse osmosis treatment was estimated at \$0.80/m^3 [29].

While many studies reported that integrating MD with waste heat sources can lower its operating cost [29, 114, 115], the focus of those studies was often on a qualitative understanding without identifying specific sources of waste heat or conducting a systems analysis to integrate full scale MD technology with actual waste heat sources. Furthermore, there are no studies in the literature that are focused on the feasibility of MD technology utilizing waste heat for treatment of high salinity produced water from shale gas extraction. Relatively abundant and unutilized source of waste heat is available in the natural gas compressor stations (NG CS) in the U.S [116]. The U.S. natural gas pipeline network is an integrated transmission and distribution network consisting of more than 210 pipeline systems, 300,000 miles of transmission pipelines, and 1,799 compressor stations with more than 17 million installed horsepower (HP) for continuous delivery of natural gas [117]. In most CS, a portion of NG is combusted to provide the energy required by the compressor engine that is usually an internal combustion engine or a gas turbine. Despite the high thermal efficiency of compressor engines, about two-thirds of the fuel energy is lost as waste heat [118]. A recent study revealed that a huge quantity of waste heat is available at NG CS in the form of hot exhaust gases [116]. It is estimated that an average of 610 TJ/day of waste heat is released in the hot flue gas of compressor engines in the U.S. at temperatures above 900 K [116]. This offers a potential to collocate wastewater treatment facilities with NG CS to offset the energy requirements of the MD process.

This study evaluated the synergies and potential of MD technology for treatment of shale gas produced water utilizing waste heat available from NG CS. A mathematical model based on the fundamentals of heat and mass transfer processes was developed and calibrated for a DCMD process using laboratory-scale experiments. The model was then used to optimize design and operating parameters for a full-scale DCMD system. The energy analysis from this model was combined with the information about available waste heat at NG CS in Pennsylvania (PA) region of Marcellus shale to estimate the amount of produced water that can be treated in distributed DCMD wastewater treatment plants. Results from this study provide important insights in the operation of an integrated system and can be extended to other sources of industrial waste heat combined with other thermally-driven water treatment technologies.

3.2 THEORY AND METHODOLOGY

3.2.1 Mathematical model of DCMD

In DCMD, the hot feed (liquid to be separated or treated) evaporates at the membrane surface and vapors travel across the membrane to be condensed in a recirculating cold liquid on the other side of the membrane. The permeate flux across the membrane can be determined by Equation 3.1 [119], where J is the mass flux (kg/m^2/s), C is the membrane distillation coefficient (kg/m^2/s/Pa), $p_{m,f}$ and $p_{m,p}$ are vapor pressures (Pa) at the feed-membrane and permeate-membrane interface corresponding to membrane surface temperatures $T_{m,f}$ and $T_{m,p}$, respectively. The MD coefficient, C, is considered fairly constant as it is weakly dependent on temperature [120, 121].

$$J = C\left(p_{m,f} - p_{m,p}\right) \tag{3.1}$$

The schematic of the heat and mass fluxes in DCMD is displayed in Figure 3.1. The presence of boundary layers at the membrane surface substantially contributes to the heat transfer resistances. Heat transfer in DCMD occurs in the following steps:

a) heat transfer from the bulk feed to the surface of the membrane (Q_f) (Equation (3.2)),

b) heat transfer across the membrane (Q_m) (Equation (3.3)),

c) heat transfer from membrane surface at the permeate side to the bulk permeate (Q_p) (Equation (3.4))

$$Q_f = h_f(T_{b,f} - T_{m,f}) \tag{3.2}$$

$$Q_m = J\Delta H + \frac{k_m}{\delta}(T_{m,f} - T_{m,p}) \tag{3.3}$$

$$Q_p = h_p(T_{m,p} - T_{b,p}) \tag{3.4}$$

where, h_f and h_p are the heat transfer coefficients ($W/m^2/K$) on the feed and permeate side respectively, ΔH is the latent heat of vaporization of water (J/kg), k_m is the membrane thermal conductivity (W/m/K), δ is the membrane thickness (m), and $T_{b,f}$ and $T_{b,p}$ are the bulk feed and permeate temperatures, respectively.

All three heat fluxes are equal at steady state (Equation (3.5)).

$$Q_f = Q_m = Q_p \tag{3.5}$$

Heat transfer across the boundary layer can offer substantial resistance leading to a difference between the membrane surface temperature and the bulk temperature of the fluid [122]. Yun et al. [79] have shown that the membrane surface temperatures can be calculated using Equations (3.6) and (3.7) that are derived from Equations (3.1) to (3.5). The authors also included constants C_p' and ΔH^o to account for the variation in latent heat of vaporization of water with membrane surface temperature.

$$T_{m,f} = \frac{\left[1-exp\left(-JC_p'\frac{k_m}{\delta}\right)\right]\left(\hbar_f T_{b,f} - J\Delta H^o\right) + JC_p'\left(T_{b,p} + \frac{\hbar_f}{\hbar_p}T_{b,f}\right)\left[2-exp\left(-JC_p'\frac{k_m}{\delta}\right)\right]}{\hbar_f\left[1-exp\left(-JC_p'\frac{k_m}{\delta}\right)\right] + JC_p'\left\{1+\frac{\hbar_f}{\hbar_p}\left[2-exp\left(-JC_p'\frac{k_m}{\delta}\right)\right]\right\}} \quad (3.6)$$

$$T_{m,p} = \frac{\left[1-exp\left(-JC_p'\frac{k_m}{\delta}\right)\right]\left(h_p T_{b,p} + J\Delta H^o\right) + JC_p'\left(T_{b,f} + \frac{h_p}{h_f}T_{b,p}\right)}{h_p\left[1-exp\left(-JC_p'\frac{k_m}{\delta}\right)\right] + JC_p'\left[2+\frac{h_p}{h_f}-exp\left(-JC_p'\frac{k_m}{\delta}\right)\right]} \quad (3.7)$$

where, C_p' = 1900 J/kg/K and ΔH^o = 2967.3 kJ/kg [79].

The heat transfer coefficients for the feed and the permeate sides can be calculated using Equations (3.8) and (3.9) [77], where Nusselt number (Nu) is evaluated from a correlation with Reynolds number (Re) and Prandtl number (Pr).

$$\hbar = Nu\frac{k}{d_\hbar} = \left[0.664 k_{dc} Re^{0.5} Pr^{0.33}\left(\frac{2d_\hbar}{l_m}\right)^{0.5}\right]\frac{k}{d_\hbar} \quad (3.8)$$

$$k_{dc} = 1.654\left(\frac{d_f}{H}\right)^{-0.039}\phi^{0.75}\left[sin\left(\frac{\theta}{2}\right)\right]^{0.086} \quad (3.9)$$

where, k is the thermal conductivity of the fluid, d_h is the hydraulic diameter of the channel, l_m is the distance between filaments of the spacer, d_f is the thickness of spacer filament, H is the thickness of the spacer, ϕ is the porosity of the spacer and θ is the hydrodynamic angle between the crosslinked spacer filaments. The correction factor k_{dc} is included to account for the effects of spacer characteristics on heat transfer.

A step-wise approach to modeling heat and mass transfer in DCMD described by Gustafson et al. [123] for large scale systems was employed to obtain the temperature and flowrate profiles along the length of the membrane module. According to this approach, the membrane is divided into several sections (Figure 3.1) and Equations (3.1) to (3.9) are used in conjunction with energy and mass balance for each section of the membrane module to obtain temperature and flow distribution across the membrane. The mass flow rates of the feed and the permeate in a section of the membrane can be evaluated by:

$$M_{f,i+1} = M_{f,i} - J_i A_i \tag{3.10}$$

$$M_{p,i} = M_{p,i+1} + J_i A_i \tag{3.11}$$

where, M ($kg \cdot s^{-1}$) is the mass flow rate, A_i (m^2) is the area of the membrane in a section and J_i ($kg \cdot m^{-2} \cdot s^{-1}$) is the mass flux across the membrane section. The subscripts 'i' refers to the feed inlet and permeate outlet for the i^{th} section, while 'i+1' refers to the feed outlet and permeate inlet for the same section of membrane (Figure 3.1). The energy balance across the i^{th} section can be used to calculate the enthalpy, and hence temperatures, of the streams leaving the section as follows:

$$M_{f,i} E_{f,i} = M_{f,i+1} E_{f,i+1} + Q_{m,i} A_i \tag{3.12}$$

$$M_{p,i} E_{p,i} = M_{p,i+1} E_{p,i+1} + Q_{m,i} A_i \tag{3.13}$$

where, E ($J \cdot kg^{-1}$) refers to the specific enthalpy and $Q_{m,i}$ ($W \cdot m^{-2}$) refers to the heat flux across the membrane.

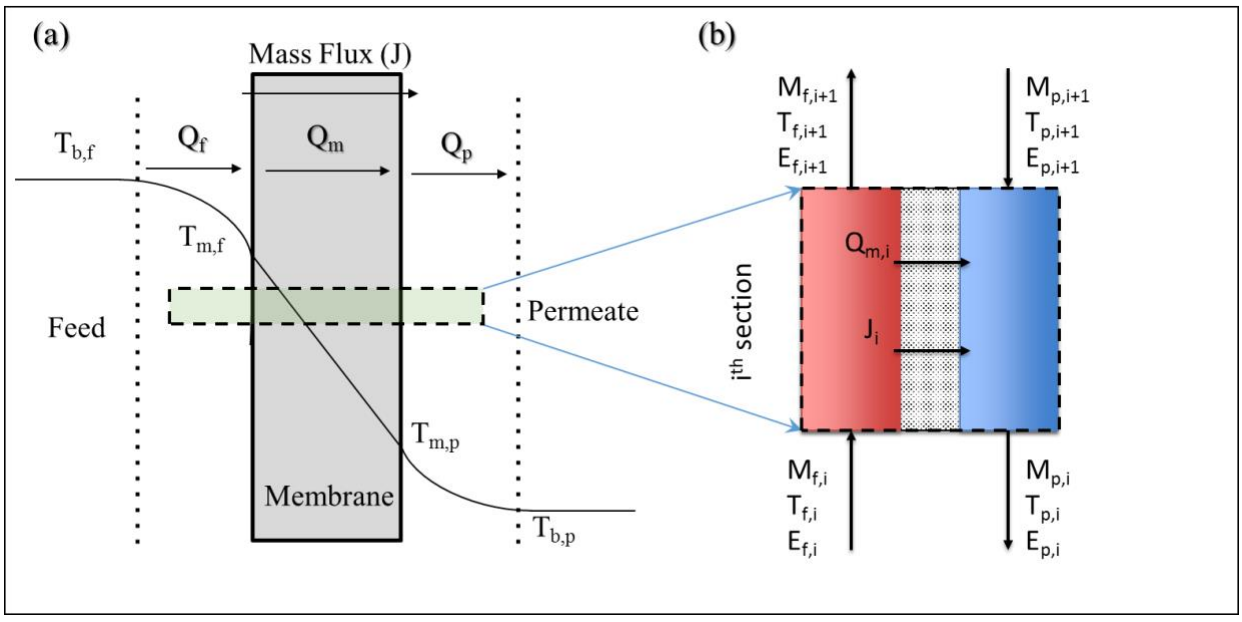

Figure 3.1. (a) Temperature profile in DCMD module, (b) enlarged section of DCMD module

3.2.2 Coupling mathematical model with Aspen Plus simulation for DCMD

The equations listed in the previous section (Eqn. (3.1) to (3.13)) were used to simulate operation of a DCMD system in Aspen Plus (Version 8.8) as a user defined unit operation. These user-defined blocks were arranged in series with the feed and permeate flow in a countercurrent direction to obtain the temperature, concentration and flow profiles of all streams. According to the flowchart for one such block shown in Figure 3.2, the temperatures of the entering streams ($T_{f,i}$ and $T_{p,i+1}$) were used as the initial guesses of the membrane surface temperatures ($T_{m,f}$ and $T_{m,p}$) to calculate the associated liquid vapor pressures ($p_{m,f}$ and $p_{m,p}$). An initial value of the flux (J) was then calculated using Equation (3.1) with a membrane distillation coefficient (C) of 5.6 $kg/m^2/hr/kPa$ determined in a previous laboratory-scale study which employed a polytetrafluoroethylene membrane with a polypropylene support [124]. The properties of the membrane and spacer used in these experiments are shown in the Appendix A1. Heat transfer coefficients (h_f and h_p) were calculated using Equation (3.8) and used to determine the membrane surface temperatures ($T'_{m,f}$ and $T'_{m,p}$) using Equations (3.6) and (3.7). These values were then used to calculate the flux (J') corresponding to the adjusted membrane surface temperatures. This iterative procedure was repeated until the relative difference between J' and J reached a selected tolerance of 0.1%.

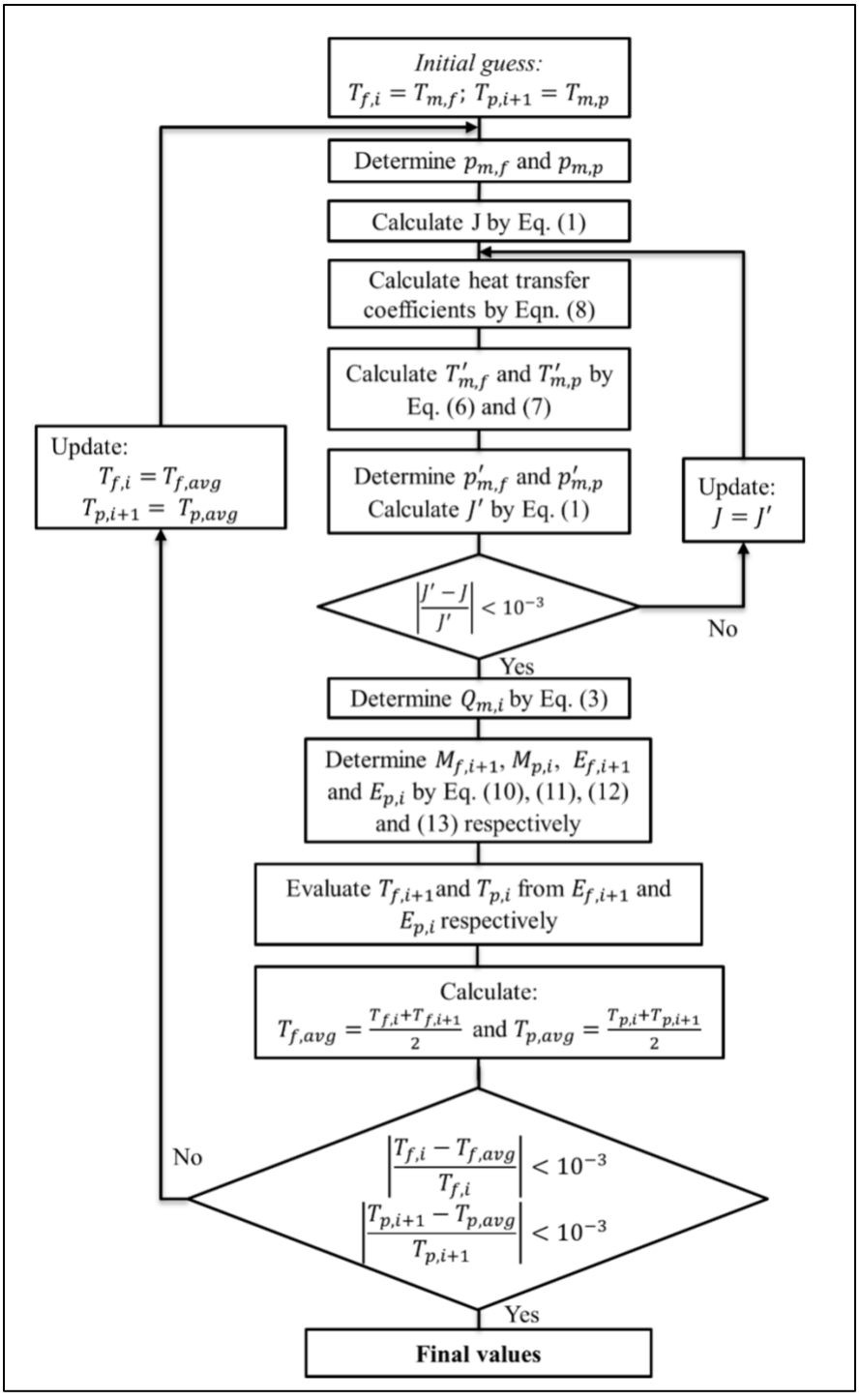

Figure 3.2. Algorithm used for the simulation of DCMD

The permeate flux obtained using this approach was used to calculate the heat flux across the membrane ($Q_{m,i}$) using Equation 3.3, and the mass flow rates of the feed and permeate streams ($M_{f,i+1}$ and $M_{p,i}$) leaving the membrane section using Equations (3.10) and (3.11), respectively. Equations (3.12) and (3.13) were then used to calculate the specific enthalpy of feed and permeate streams ($E_{f,i+1}$ and $E_{p,i}$) leaving the module section, which were then used to calculate the temperatures of these streams ($T_{f,i+1}$ and $T_{p,i}$). Finally, the averages of the feed and permeate bulk temperatures ($T_{f,avg}$ and $T_{p,avg}$) were calculated and the initial guesses of membrane surface temperatures ($T_{m,f}$ and $T_{m,p}$) were updated with these values. The same procedure was repeated until the relative difference between the values calculated in subsequent iterations was below 0.1%.

The mass and heat fluxes across the membrane section were determined at the average values of stream properties for each section of the membrane to prevent overestimation of the fluxes. For example, if the feed stream enters a membrane section at 60 ^{o}C and the permeate stream enters on the other side of the module at 40 ^{o}C, it is reasonable to assume that the feed stream would leave the membrane section at a lower temperature (e.g., 58 ^{o}C) while the permeate side stream would leave that same section at a higher temperature (e.g., 42 ^{o}C). The flux values are generally calculated at the feed inlet temperature (i.e., 60 ^{o}C) and permeate inlet temperature (i.e., 40 ^{o}C) in most theoretical models, which can lead to overestimation of fluxes as the predicted vapor pressure difference would be greater than is the case in reality. Hence, calculating the flux using the average feed temperature (i.e., 59 ^{o}C) and average permeate side temperature (i.e., 41 ^{o}C) would result in a more accurate flux prediction. It should be noted that these calculations were carried out assuming negligible heat loss to the surroundings. The physical properties of the streams were obtained from the electrolytic Non-Random Two-Liquid (NRTL) model available in Aspen Plus.

3.2.3 Calibration of the mathematical model

Previous work by the authors showed that the concentration polarization could result in up to 30% increase in the salt concentration at the feed-membrane surface at high salinities [124]. The model used in this study was therefore calibrated to account for this reduction in the driving force (vapor pressure) at higher salt concentration due to concentration polarization. Model calibration was carried out using the experimental data with the feed temperature of 60 ^{o}C and feed flow rate of 1.9 L/min. To calibrate the model, the difference in the predicted flux and experimentally observed flux values at different salinities was evaluated and the predicted flux was adjusted according to the experimentally observed concentration polarization coefficient. The experimental setup and the composition of produced water samples used for model calibration and validation is discussed elsewhere [124].

3.3 RESULTS AND DISCUSSION

3.3.1 Calibration/validation of the DCMD model

As shown in Figure 3.3, the model that was calibrated using the data collected at 60 ^{o}C was able to predict experimentally measured permeate flux at different feed temperatures, flow rates and salinities with a root mean square error of 6%, which is satisfactory for industrial applications [125]. The results shown in Figure 3.3 indicate that the impact of feed flow rate on permeate flux is significantly lower than that of the feed temperature. For instance, a three-fold increase in the feed flow rate from 1.1 L/min (Re = 1,330) to 3.4 L/min (Re = 4,000) increases the permeate flux

by only 17% at a feed temperature of 60°C (Figure 3.3(a)). On the other hand, increasing the feed temperature from 50 to 60 °C at a feed flow rate of 1.1 L/min increases the permeate flux by 103%. While increasing the feed flow rate helps to decrease the effects of temperature polarization and improves mass transfer [63], the feed temperature is directly responsible for the driving force. This effect of temperature and flow rate on the permeate flux is consistent for varying salt concentrations as shown in Figure 3.3 and is in agreement with other studies [126, 127].

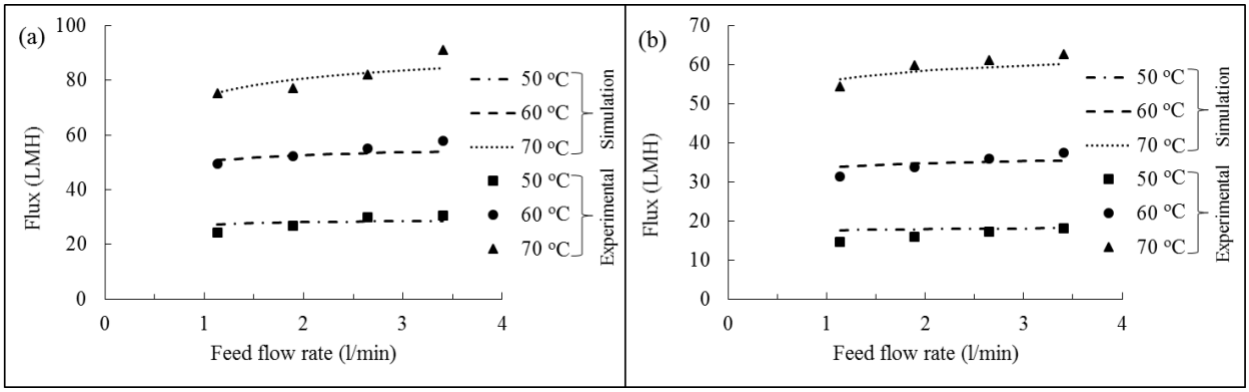

Figure 3.3. Comparison of simulated DCMD process with the experimental results obtained for (a) a TDS of 92.8 g/l and (b) TDS of 308.3 g/l. Permeate temperature and flow rate were 30 °C and 1.9 l/min, respectively.

Calibrated and validated model was used to predict flux and temperature profiles for large scale systems using the approach that was successful in predicting the permeate flux for a hollow fiber polypropylene membrane area of up to 0.66 m^2 [110]. Commercial microfiltration membrane assemblies commonly use membrane areas of 0.1 to 0.2 m^2 [128] and the area of a single flat-sheet membrane chosen for this simulation was 0.2 m^2. The number of membrane modules in series or the effective membrane area governs the temperature change on both feed and permeate side. As discussed before, increasing the feed flow rate enhances permeate flux across the membrane; the same is true for permeate side flow rate [109, 129]. However, this increase in permeate flux due to higher feed- or permeate-side flow rates eventually reaches a plateau after which increasing the

flow rates has no effect on the permeate flux. Hence, a minimum Reynolds number of 1,000 was used for simulating large scale membrane modules to ensure higher permeate flux across the membrane. Similarly, the temperature difference between the feed inlet and the permeate inlet streams were chosen to achieve maximum permeate flux and heat recovery. More information on the choice of temperatures is provided in the later section that discusses heat recovery and specific thermal energy requirements.

As can be seen in Figure 3.4, the permeate flux decreases with an increase in membrane area because of the decrease in temperature difference between the feed and permeate sides that occurs when more modules are added in series. Consequently, the total permeate flow initially increases with an increase in membrane area (Figure 3.4) but it levels off after a certain point when adding more modules in series offers limited benefit to the overall system performance.

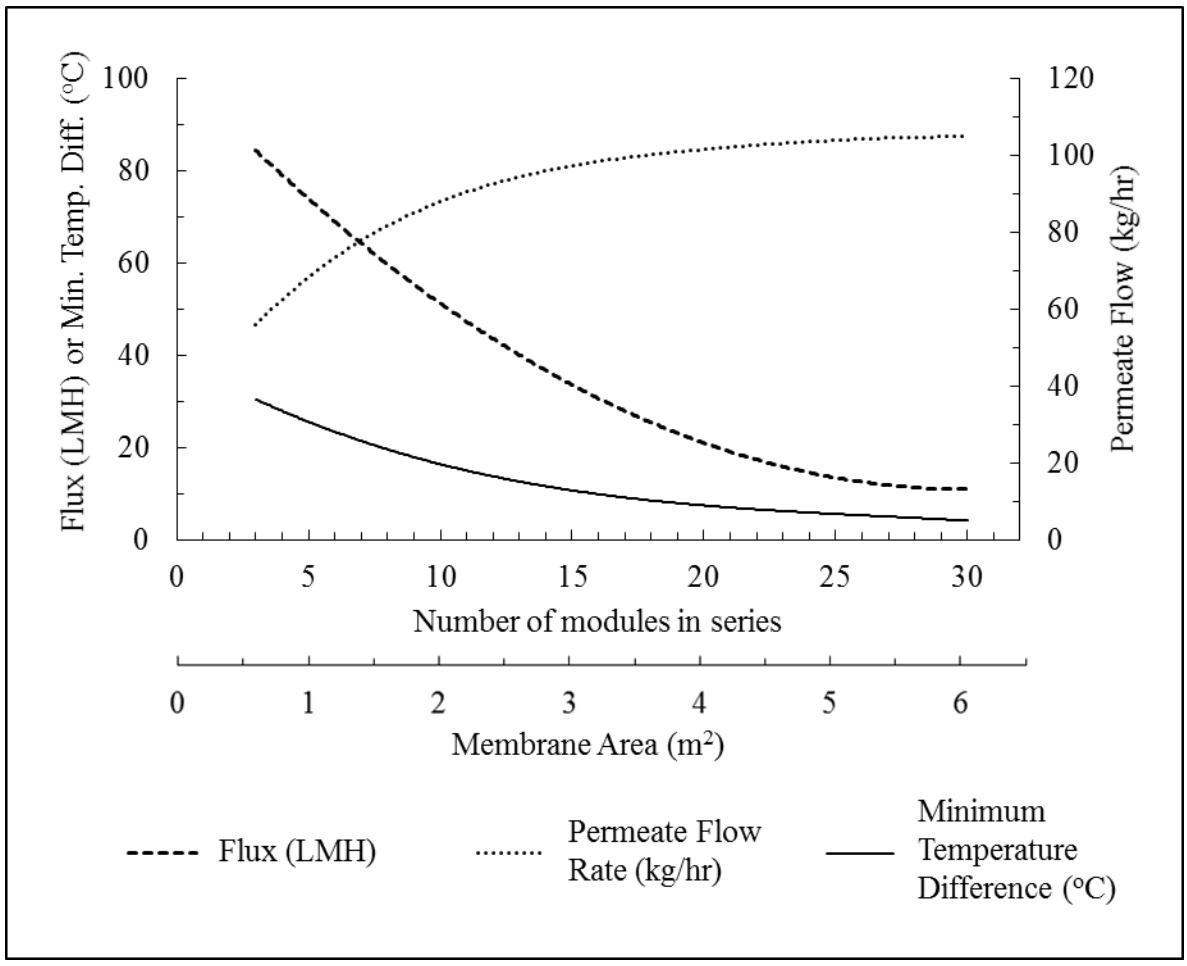

Figure 3.4. Minimum temperature difference, flux, and permeate flow profiles as a function of membrane area in a counter-current DCMD system. The feed and permeate flow rate was 1500 kg/hr while the inlet feed and permeate temperatures were fixed at 90 °C and 30 °C, respectively.

A minimum temperature approach similar to that used for the design of heat exchangers [130] was employed in this study to evaluate the maximum possible number of membrane modules in series. For heat exchangers, a minimum temperature difference of 10 ^{o}C between the hot and the cold side has been established as a thumb rule for effective heat transfer [131, 132]. Therefore, the minimum temperature difference between the feed outlet and the permeate side inlet in any module of a DCMD array was set at 10 ^{o}C to ensure that a reasonable driving force would be maintained in all modules. The maximum membrane area that meets this condition for the feed inlet temperature of 90 ^{o}C and the permeate inlet temperature of 30 ^{o}C was 3.6 m^2, which corresponds to 18 modules in series. The average flux obtained for these conditions was 26.5 $kg/m^2/hr$, which is significantly higher than 8.1 $kg/m^2/hr$ reported for a similar case in the literature [110]. This difference can be attributed to a considerably higher MD coefficient of the membrane used in this study [124] because of the highly porous and thin membrane selected for this application as shown in Appendix A1.

The objective of this study was to assess the energy requirements for produced water treatment using available waste heat from NG CS and these calculations were scaled up to a large scale system by simply putting the arrays of 18 modules in series in a parallel arrangement to achieve a desired total system capacity as illustrated in Appendix A1.

3.3.2 DCMD system with heat recovery

Heat recovery in DCMD system has been analyzed previously [80, 103, 104, 133] and the process flow diagram used in this study depicted in Figure 3.5 is similar to a recent case study of DCMD based desalination [104]. While the previous study [104] focused on concentrating the seawater

from a TDS of 28,050 mg/l to about 140,000 mg/l, this study evaluated the use of DCMD to concentrate produced water from TDS of 100,000 mg/l (10 wt.%) to 300,000 mg/l (30 wt.%). Flue gas from an NG CS was incorporated in the system as a source of waste heat using intermediate steam loop to drive the MD process. Heat exchanger HX-4 is used to generate steam at 3.6 bar (140 ^{o}C) using the hot flue gas, which is then utilized to increase the temperature of the MD feed stream to a desired operating temperature. Because the permeate stream is heated as it travels through the MD array, the heat exchanger HX-2 is added to recover some of that heat for preheating the feed stream. The permeate stream leaving HX-2 is cooled down to 30 ^{o}C in heat exchanger HX-1 by contacting with fresh produced water feed. It is assumed that a sufficient quantity of produced water is available at 20 ^{o}C to cool down the permeate stream in heat exchanger HX-1.

The salinity of produced water depends on the location and age of the fractured well with sodium chloride as the major constituent. For the purpose of this study, the salinity of the feed water was assumed to be 10 wt.% sodium chloride solution, while that of the brine leaving the system was fixed at 30% to yield the overall water recovery factor of 66.7%. It should be noted that a large volume of feed has to be recycled through the MD array because of the low water recovery rate in a single pass through a DCMD and that the flowrate of brine that is purged from the system is significantly lower than the flowrate of recycled brine. A full-scale system would typically include a pretreatment step to remove the scale forming salts prior to DCMD treatment. Hence, it is assumed that the flux decrease due to membrane fouling would be negligible.

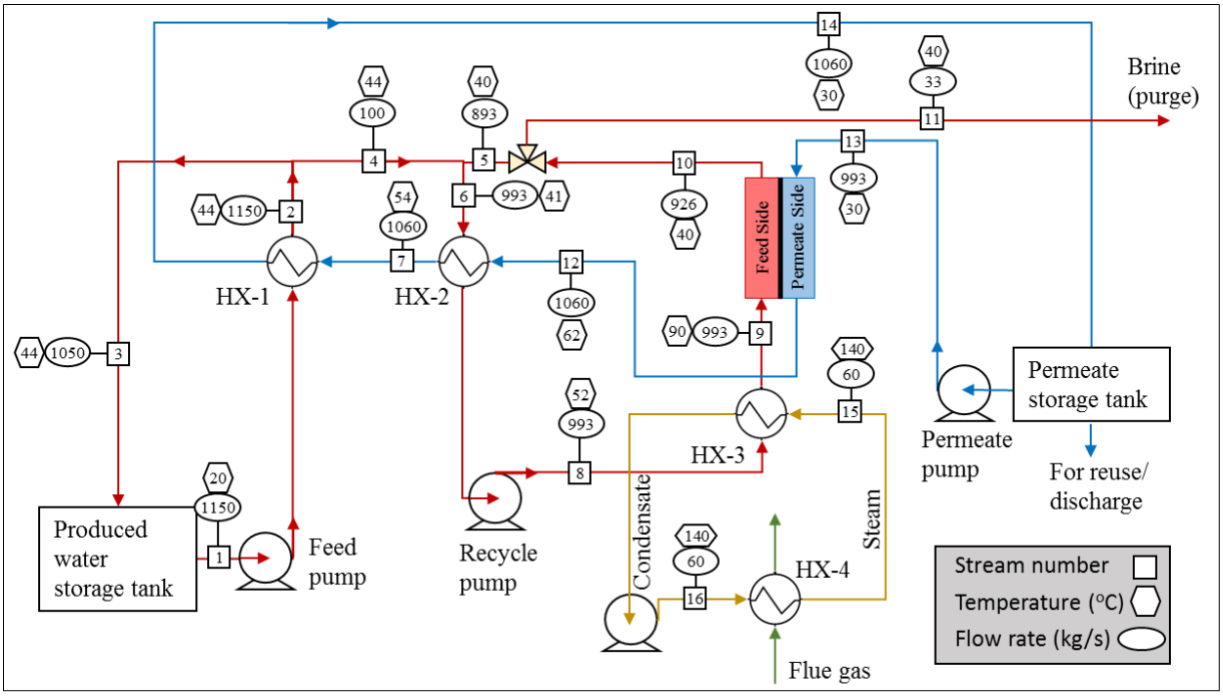

Figure 3.5. Schematic flow diagram of the DCMD desalination plant treating 100 kg/s (stream 4) of feed water. DCMD feed and permeate inlet temperature are 90 °C and 30 °C respectively, whereas the required membrane area is 9102 m^2.

Simulations of system performance were performed at different feed temperatures to determine the optimum range based on the specific thermal energy consumption (kWh/m^3) and the results are shown in Figure 3.6. As expected, the permeate flux increases with an increase in feed temperature. It must be noted that the fraction of recovered energy also increases with temperature because the permeate stream leaves the DCMD system at higher temperatures when the feed temperature is increased. As shown in Figure 3.6(b), the energy required per m^3 of permeate increased from 527 to 565 kWh/m^3 as the feed temperature decreased from 90 to 60 °C; hence, it is preferable to operate DCMD at a higher temperature where almost 37% of the energy needed for system operation can be recovered using heat exchangers HX-1 and HX-2. The lowest specific thermal energy required to operate DCMD was reported by Lin et al. [134] as 27.6 kJ/kg (or 7.67

kWh/m^3) but the values reported in the literature are at least one order of magnitude higher than this thermodynamic minimum. Khayet et al. [135] obtained a specific thermal energy consumption of 600 kWh/m^3 for a DCMD pilot study with a membrane area of 4 m^2, which is comparable to the values determined in this study. Khayet and Matsuura [136] reported the specific thermal energy requirement for a theoretical 24,000 m^3/day DCMD desalination plant studied by Al-Obaidani [137] of 39.7 kWh/m^3. However, these calculations assume a very high water recovery of 80% from DCMD without any recirculation of the feed side stream while the thermodynamic maximum for single pass recovery that can be attained in a DCMD system is 6.4% [134].

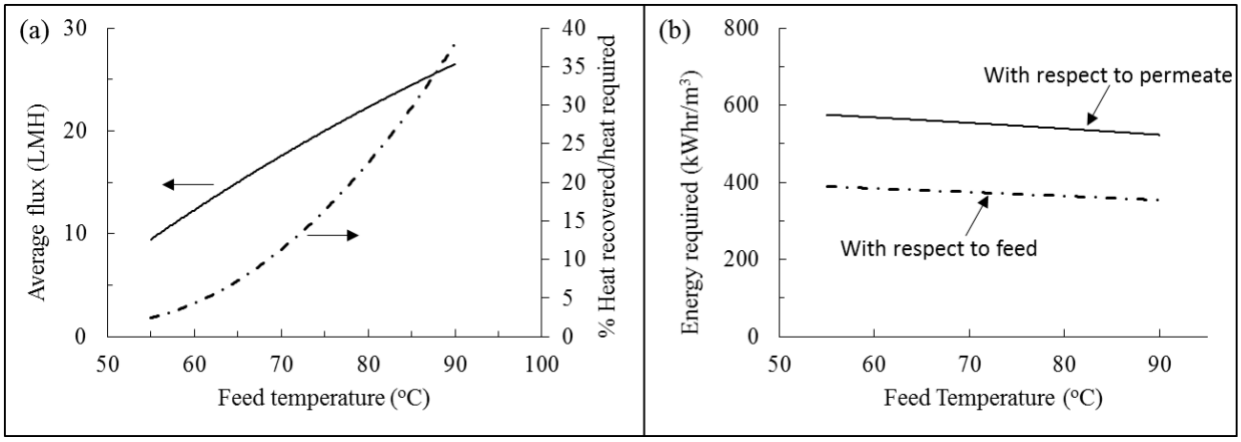

Figure 3.6. (a) Average flux and percentage heat recovery as a function of feed temperature, (b) Specific thermal energy required to concentrate produced water from 10% to 30% TDS as a function of feed temperature.

The Gain Output Ratio (GOR), which is defined as the ratio of the amount of permeate generated to the amount of saturated steam provided to the system [138], can theoretically be as high as 21 for DCMD systems [139] while the highest value of GOR obtained experimentally was between 5 and 6 [80, 140]. However, the temperature difference between the hot and the cold streams for both membrane modules and heat exchangers used for heat recovery would have to be around 1-2 °C to achieve such high GOR. Such low temperature difference would require enormous membrane and heat exchanger area and will detrimentally impact the economics of the

overall treatment process (i.e., capital cost). In addition, the flow rate of feed and permeate side streams in the DCMD system must be very low to obtain high water recovery and achieve higher GOR value [140]. While this makes the process more energy efficient, it significantly decreases the permeate flux because the temperature difference between the feed and the permeate side is drastically reduced due to increased residence time. Both these factors would lead to a substantial increase in the membrane area to achieve desired water recovery. Therefore, the minimum temperature approach was utilized in this study to optimize the membrane and heat exchanger area, which yielded a maximum GOR of 1.07 when the feed temperature was 90 ^{o}C.

3.3.3 Produced water treatment by DCMD in PA

To evaluate the potential of DCMD to treat produced water from unconventional gas extraction using waste heat available at NG CS in Pennsylvania (PA), it is necessary to estimate the volume of produced water generated in PA. The total shale gas production on a county level in Marcellus shale play in PA was based on the most updated information (January-July 2014) published by the Pennsylvania Department of Environmental Protection (PA DEP) [141]. There were 5,188 active unconventional gas wells operating in 2014 in PA with a total natural gas production of 5.1×10^{10} m^3 [142]. The amount of produced water per unit volume of gas production varies across different states and shale plays due to the differences in shale formation characteristics. Previous studies have shown that 300 barrels (47.7 m^3) of brine are produced per MCM (million cubic meter) of shale gas recovered in PA [143]. Brine production per day is calculated based on the total amount of produced water and the number of production days for each well provided by PA DEP [141]. Figure 3.7 shows estimated aggregate amount of produced water on a county level in PA during the first half of 2014. The results indicate that produced water generation ranged from 0.014

m^3/day in Cambria County to 3,211.5 m^3/day in Susquehanna County. Based on this analysis, it can be estimated that a total of about 2.78 MCM of produced water is generated in PA in the first six months of 2014, which is equivalent to 630 m^3/hr.

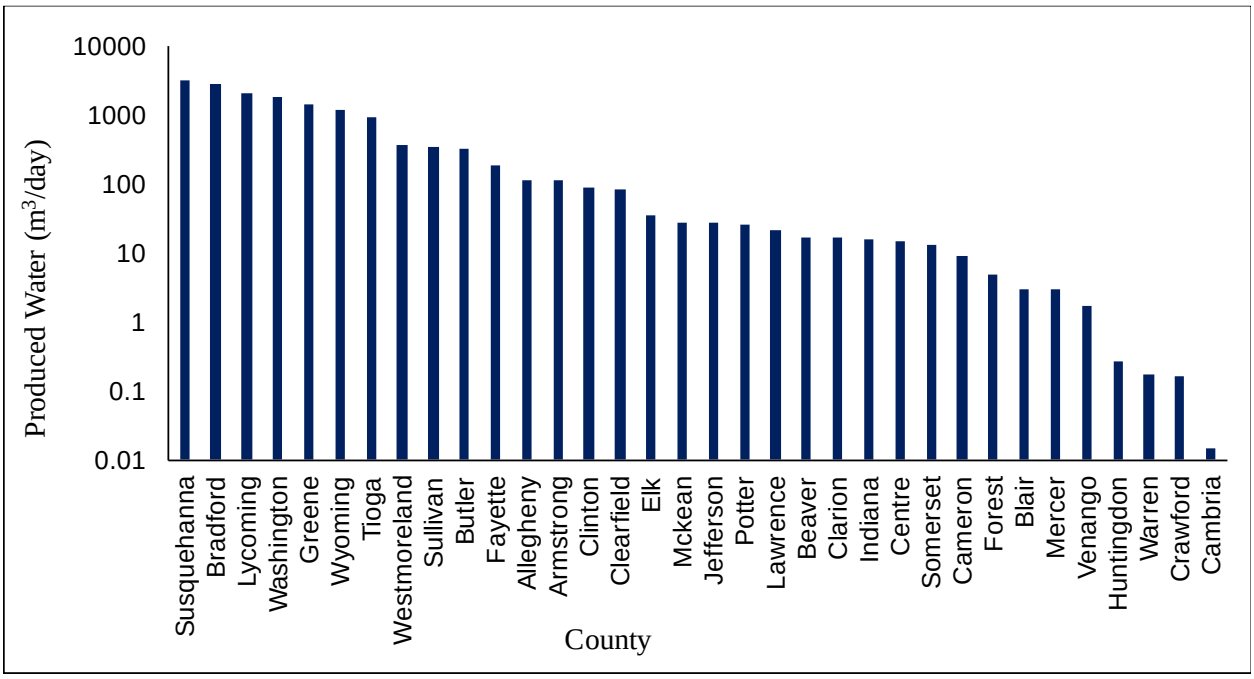

Figure 3.7. Estimated quantity of produced water on a county level in Pennsylvania

Previous study estimated that a total of 43.4 TJ/day of waste heat is available at natural gas compressor stations in PA [116]. The amount of energy required to concentrate the produced water generated in PA to 30% salinity can be estimated based on the DCMD specific thermal energy consumption shown in Figure 3.6(b). For example, the specific thermal energy consumption with respect to produced water with a TDS of 10 wt.% is 382 kWh/m^3 when the feed temperature is 60 ^oC. While this is the net energy requirement of the process, the actual energy requirement depends on the efficiency of steam generation. Assuming the efficiency of steam generation of 80%, it can be estimated that a total of 26 TJ/day of energy would be needed to treat 630 m^3/hr of produced water generated in PA if DCMD process is operated using the feed temperature of 60 ^oC. Figure

3.8(a) shows the amount of energy required to concentrate the produced water generated in PA to 30% as a function of feed temperature. The energy requirement in Figure 3.8 is calculated assuming 80% efficiency for steam generation. If the feed temperature is increased to 90 ^{o}C, only 56% of the total waste heat available from NG CS in PA is sufficient to concentrate the produced water generated in PA to 30% salinity. The effect of changes in produced water salinity on the energy requirements for DCMD process is shown in Figure 3.8(b). The results in this figure indicate the energy required to treat produced water would be lower than the available waste heat energy regardless of the feed water salinity. A maximum of 32.2 TJ/day of energy would be required to treat all produced water in PA even if the feed salinity is just 3%.

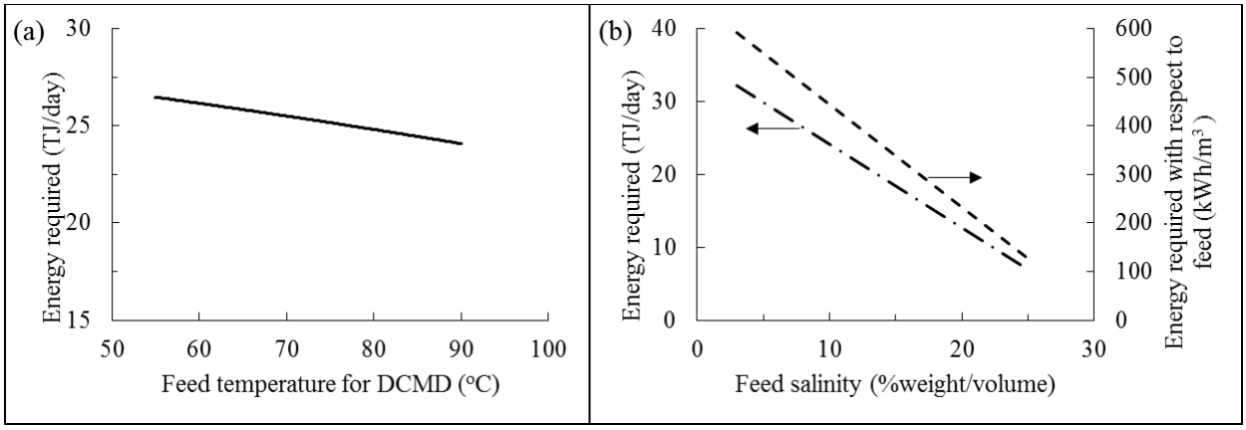

Figure 3.8. (a) Thermal energy required to concentrate produced water in PA to 30% salinity using DCMD as a function of feed temperature at a fixed initial TDS of 10% (w/v), (b) Total thermal energy and specific thermal energy with respect to feed as a function of the feed salinity when the feed temperature is 90 ^{o}C and is concentrated to 30% salinity.

Practical constraints such as transportation of produced water to the source of waste heat are likely to limit the application of MD technology. This issue can be clearly seen in Figure 3.9 which displays the spatial distribution of theoretical DCMD treatment capacity at NG compressor

stations and the estimated quantity of produced water generated in each county. Figure 3.10 highlights the counties with sufficient treatment capacity and counties with insufficient treatment capacity. The results in Figure 3.9 and Figure 3.10 were developed assuming that the DCMD system is operated at an inlet feed temperature of 90 ^{o}C and the theoretical amount of produced water that could be treated utilizing the waste heat from NG CS in PA was estimated based on the installed capacity at each compressor station [116]. Transportation of produced water to NG CS sites may be feasible in counties that have several NG CS (e.g., Greene County) as it is likely to have a limited impact on the overall produced water management cost. However, water transportation costs may become significant and prohibitive for counties that do not have NG CS in close proximity (e.g., Susquehanna County in the northwest corner of the state that generates the highest amount of produced water in PA). Future analysis should focus on the economic feasibility of using DCMD for treatment of produced water utilizing waste heat to identify major cost drivers.

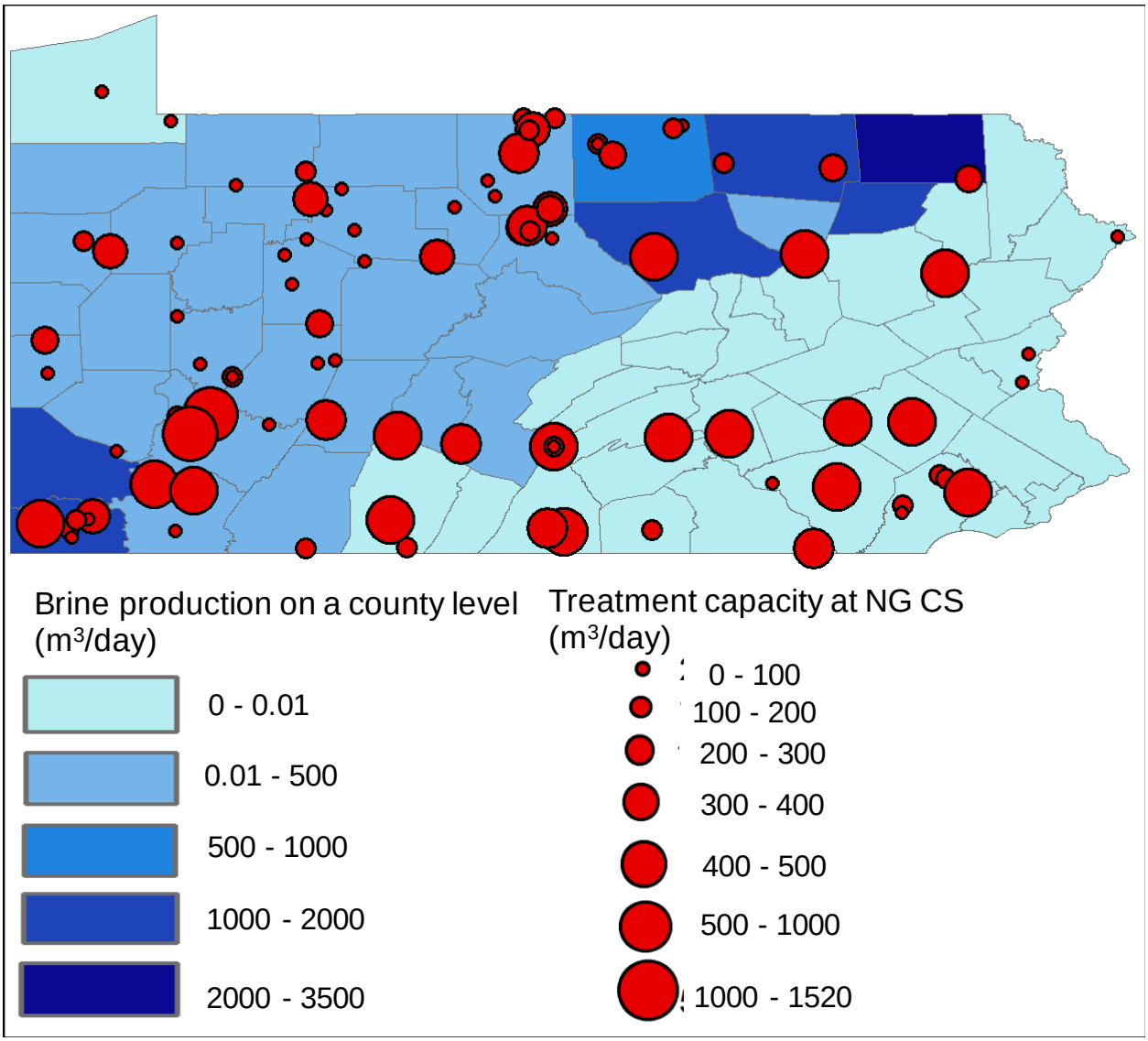

Figure 3.9. Spatial distribution of estimated produced water and treatment capacity using available waste heat at NG CS in PA

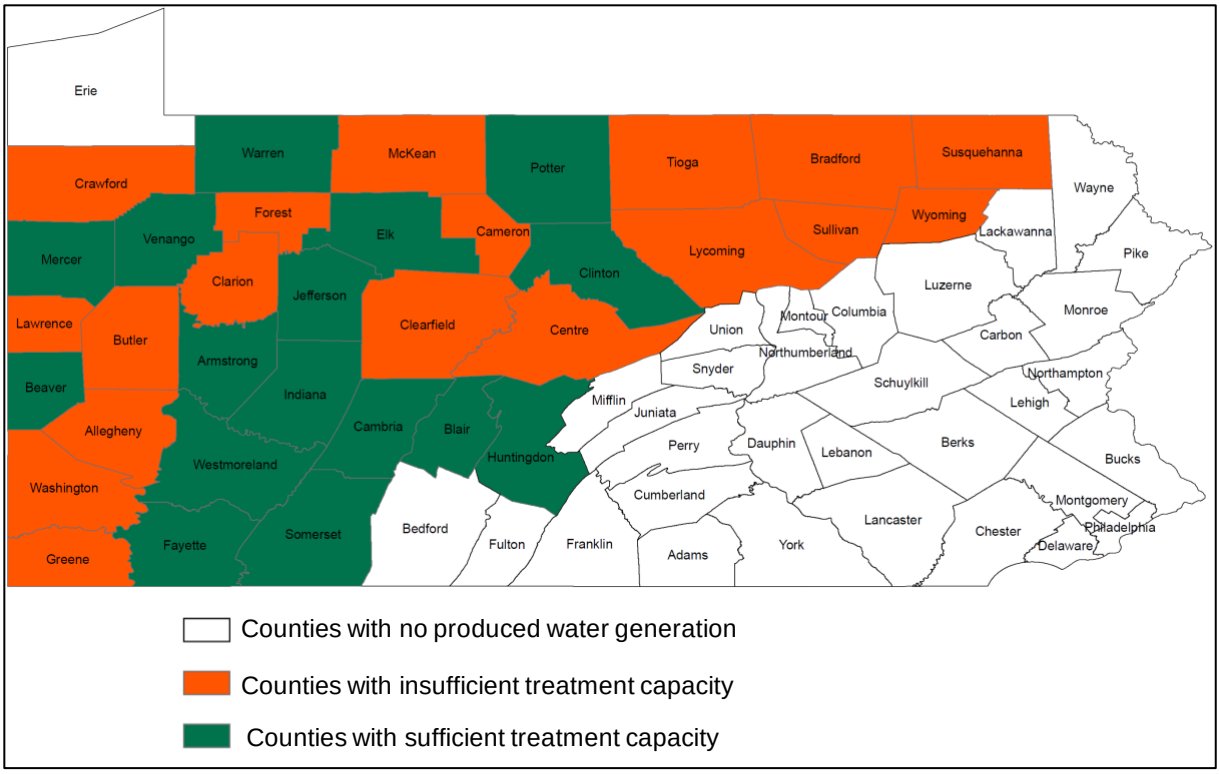

Figure 3.10. Map of PA highlighting the counties that have NGCS with sufficient treatment capacities and those that do not have sufficient treatment capacities.

3.4 CONCLUSIONS

A mathematical model using fundamental heat and mass transfer equations and literature correlations was developed in this study to predict the performance of large scale DCMD systems. The model was calibrated using the results of laboratory-scale studies and the concept of minimum temperature similar to that employed in the design of heat transfer equipment was used to obtain the optimum membrane area when several membrane modules are arranged in series. It was found that a minimum temperature difference of 10 ^{o}C between the feed and the permeate-side streams yielded an optimum membrane area for permeate flux across the membrane. Using sensitivity analysis, it was established that the heat recovery efficiency and permeate flux increase with an increase in the DCMD feed temperature, which reduces the specific thermal energy consumption of this treatment process. A plant scale DCMD system with optimum membrane area, external heat recovery, and utilizing waste heat from NG CS was evaluated for its potential to treat produced water in PA region of Marcellus Shale. It was found that the amount of energy required to concentrate produced water in PA to 30% salinity was much lower than the amount of waste heat available from NG CS irrespective of the produced water salinity. The key findings of this study suggest that DCMD is capable of concentrating all the produced water in PA if the waste heat from NG CS can be utilized. However, the economic feasibility of this approach needs to be evaluated to identify major cost drivers and barriers.

4.0 IMPORTANCE OF FEED RECIRCULATION FOR THE OVERALL ENERGY CONSUMPTION IN MEMBRANE DISTILLATION SYSTEMS

Membrane distillation (MD) has received significant interest for treating high salinity wastewaters, particularly when reverse osmosis is not feasible. MD has low single pass water recovery, which necessitates feed recirculation to achieve a desired overall water recovery. Feed recirculation increases turbulence in the feed channel to reduce polarization effects and membrane fouling. However, it increases the thermal and electrical energy requirements of the system. This study emphasizes the importance of recirculation and demonstrates its impact on the energy consumption of MD, which can be an order of magnitude greater when compared with calculations based on a single pass recovery. For instance, an increase in water recovery in a DCMD module from 10 to 50% for a feed solution containing 100 g/L of NaCl would increase the required recycle ratio by 633% (i.e., from 3 to 22) with a corresponding increase in thermal energy required to heat the recycle stream by 556% (i.e., from 39 to 256 kWh/m^3 of feed). While the electrical energy required for feed recirculation is only a few percent of thermal energy requirements, it may be a significant factor when considering the overall life cycle impacts of the MD process.

4.1 INTRODUCTION

Separation processes based on membrane technology have become an integral part of present day industries. Membrane distillation (MD) is one such technology that has the potential to become a cost effective approach for treating saline water to recover high-quality water. Unlike other membrane technologies, MD is a non-isothermal process which is driven by the vapor pressure difference across a hydrophobic membrane. Although the first MD patent was filed in 1963 [90], research on MD only received significant interest in early 1980s due to availability of membranes with improved characteristics [97]. This process is still in the early stages of the development for large scale applications. MD has been studied on a laboratory scale for the removal of heavy metals from wastewater [46], radioactive contaminants from aqueous solutions [47], desalination of sea water [35, 42, 48], fruit juice concentration [49-51] and acid recovery [52]. Pilot scale studies have been conducted for desalination of sea water and produced water from unconventional resources as well as treatment of groundwater and reverse osmosis concentrates [110, 112, 144-146].

4.1.1 Energy requirements in Membrane Distillation

Like all thermal separation processes, the major energy requirement of MD arises from the latent heat required to evaporate water on the feed side of the membrane. In addition, there are inherent process inefficiencies that result in additional energy requirements of MD. In direct contact membrane distillation (DCMD), these inefficiencies result from the sensible heat loss through conduction by the membrane from the feed side to the permeate side. The energy loss due to conduction can account for 30 to 80 % [76, 137, 147] of the total thermal energy consumption of the process [103]. The conduction heat losses can be reduced by appropriate design of the MD

module and membrane selection, and by optimizing the operating parameters of DCMD [137, 148]. Significantly lower conduction losses can be achieved in vacuum membrane distillation (VMD) and air gap membrane distillation (AGMD) due to low thermal conductivity of gas phase on the permeate side [147, 149].

4.1.2 The Need for Recirculation

Unlike pressure driven membrane separation processes like reverse osmosis and nanofiltration, which can have a single pass water recovery in the range of 50-84% [150-152] depending on the feed chemistries and the driving force, MD has significantly lower single pass water recovery [134, 140]. A single pass MD system can be employed for desalination of sea water, where the objective is to provide fresh water. In such a case, sea water could be fed to the MD unit and the concentrate can be discharged because a large volume of saline water is available as feed for continuous operation. However, when the MD system is used to treat wastewater, an overall recovery factor much greater than that attained in a single pass system would be required. To attain a desired recovery factor, the concentrate (reject) stream leaving the MD system has to be reheated, recycled, and mixed with fresh feed. Concentrate recycling that is required for high recoveries in MD systems [104, 114, 144, 153] will substantially increase the amount of thermal energy for reheating the concentrate stream and electrical energy for pumping it back to the inlet of an MD system. In addition, high recovery factors lead to increase in the feed salt concentration, which lowers the water vapor pressure at the feed side and decreases the evaporation efficiency [100, 124, 154]. While several studies estimated the maximum single pass permeate recovery [104, 112, 134, 139, 140, 155-159] of an MD system, only two previous studies [104, 160] provided the operating

details needed to calculate the recycle ratio. A recycle ratio of 11.8 was estimated using the flow rates reported for the pilot scale DCMD sea water desalination system [104], while the recycle ratio of 10.6 was needed to achieve 66.7% water recovery when treating produced water from unconventional gas extraction [160]. In this study, an ASPEN Plus based model developed previously [160] was used to study the impact of recycle ratio on energy consumption of DCMD without heat recovery. The results from this study highlight the importance of feed recirculation in DCMD and its effect on thermal and electrical energy requirements in a continuous DCMD system used for concentrating high salinity brine.

4.2 THEORY AND METHODOLOGY

4.2.1 Impact of evaporation efficiency on single pass permeate recovery and recycle ratio

For an MD system, the permeate flow across the membrane can be calculated as follows:

$$\text{Permeate flow } \left(\frac{\text{kg}}{\text{s}}\right) = \frac{\text{Evaporation efficiency} * \text{Enthalpy change in the feed } (\frac{\text{kJ}}{\text{s}})}{\text{Latent heat of vaporization } (\frac{\text{kJ}}{\text{kg}})}$$

or,

$$mx = \frac{\eta\left[mC_pT_{in} - m(1-x)C_pT_{out}\right]}{100 * L} \tag{4.1}$$

where, m is the feed flow rate (kg/s), x is the fraction of feed that is recovered on the permeate side, η is the evaporation efficiency of the system, which is equal to the ratio of thermal energy utilized in evaporating the feed to total energy lost to the feed side [80, 161, 162], C_p is the specific heat capacity of water, which is assumed to be constant (4.184 kJ/kg/K), T_{in} and T_{out} are feed inlet

and exit temperatures (°C), respectively, and L is the latent heat of vaporization of water (2,260 kJ/kg). The above equation can be simplified as follows:

$$x = \frac{T_{in} - T_{out}}{\frac{100 * L}{\eta C_p} - T_{out}} \quad (4.2)$$

Hence, the maximum amount of permeate that could be recovered from the feed in a single pass (i.e., single pass permeate recovery) can be calculated if the evaporation efficiency of a system is known.

4.2.2 DCMD simulation in ASPEN Plus platform

An ASPEN Plus (Version 8.8) model developed and validated in a previous study [160] was employed to study the impact of feed recirculation on energy requirements of a DCMD system. The model included fundamental equations of heat and mass transfer to simulate the operation of a countercurrent DCMD system and was used to calculate temperature, concentration and flow profiles of the feed and permeate streams. The equations and algorithm used for simulating DCMD is presented elsewhere (Section 3 [160]). In short, a step-wise modeling approach where the membrane module is divided into sections and energy and mass balance calculations were used to determine temperature and flow rates of feed and permeate streams for each section.

In DCMD, permeate flux can be calculated as follows:

$$J = C(p_{m,f} - p_{m,p}) \quad (4.3)$$

where, J is the permeate flux (kg/m^2/hr), C is the membrane distillation coefficient (kg/m^2/hr/Pa) and $p_{m,f}$ and $p_{m,p}$ are vapor pressures (Pa) at the feed-membrane and permeate-membrane interfaces, which correspond to membrane surface temperatures $T_{m,f}$ and $T_{m,p}$, respectively. Temperatures of the feed and permeate streams entering the DCMD system were used as the initial

guesses of the membrane surface temperatures ($T_{m,f}$ and $T_{m,p}$) and the initial value of the flux (J) was calculated using Equation 4.3 with a membrane distillation coefficient (C) of 5.6 kg/m^2/hr/kPa determined in a previous laboratory-scale study [124]. Properties of the membrane and the spacer used in these experiments are available elsewhere [124, 160] while heat transfer coefficients on the feed and permeate sides were calculated using Nusselt number correlations and used to determine the membrane surface temperatures [160]. These new values for membrane surface temperatures were used to determine the new permeate flux (J′) corresponding to the adjusted membrane surface temperatures and this iterative procedure was repeated until the relative difference between two successive iterations reached a relative difference of 0.1%. The resulting permeate flux was used to determine the thermal energy transferred across the membrane, which is comprised of the latent heat lost with evaporated water and the heat transferred by conduction through the membrane. These results were combined with permeate flux values to calculate mass flow rates and temperatures of the feed and permeate streams leaving the module section. Lastly, the average feed and permeate temperatures in a module segment were determined and the initial guesses of membrane surface temperatures were updated with these values. The whole procedure, from updating the initial values of membrane surface temperatures to obtaining the average feed and permeate temperatures, was repeated until the relative difference between the average feed and permeate temperature estimated in successive iterations was below 0.1%.

Model calibration and validation using the experimental results from a DCMD system operated at different feed temperatures, flow rates and salt concentrations are presented elsewhere [160]. The following assumptions were used in the simulations performed in this study:

1- Process is at steady state.

2- Heat energy lost to the surroundings is assumed to be negligible.

3- Membrane wetting does not occur.

4- Salt rejection is assumed to be 100%.

5- Sodium chloride is the only dissolved constituent in the feed.

6- Membrane area is 0.2 m^2.

7- Membrane distillation coefficient is 5.6 LMH/kPa.

4.3 RESULTS AND DISCUSSION

The evaporation efficiency depends on membrane characteristics, hydrodynamic conditions in the feed and permeate channels, feed salinity and feed and permeate vapor pressures and varies significantly for different MD configurations. As demonstrated in Equation 4.2, evaporation efficiency is a key factor governing single pass permeate recovery of an MD system and it was considered as an independent variable in this study to obtain a general trend in single pass permeate recovery. Figure 4.1(a) shows the effect of evaporation efficiency on the single pass permeate recovery in an MD system with the feed inlet and exit temperatures of 90 and 40 ^oC, respectively. Because of low permeate recovery in a single pass (i.e., below 10%), it is necessary to return the concentrate to the MD module to improve the overall permeate recovery. Recycle ratio is the ratio of mass flow of the recycle stream to the mass flow of the fresh feed to the system. Figure 4.1(a) also shows the recycle ratio as a function of evaporation efficiency when the feed consists of 100 g/L total dissolved solids (TDS) and is concentrated to 200 g/L TDS through a continuous MD system shown in Figure 4.1(b). The recycle ratio increases with decreasing evaporation efficiency as more concentrate has to be recirculated to achieve the same water recovery. The recycle ratio

in this study was calculated based on a mass balance across the MD unit for a given evaporation efficiency as described in the Appendix A2. The range of evaporation efficiencies (without heat recovery) for DCMD, AGMD and VMD shown in Figure 4.1(a) was obtained from the literature [76, 137, 147, 149, 161-164]. As seen in this figure, the percentage of feed recovered as permeate in a single pass cannot exceed 10% even if 100% thermal efficiency could be attained in an MD system. Previous study has shown that the single pass recovery for DCMD is in the range of 2 to 6% [140] while Lin et al. [134] reported that the thermodynamic limit for single pass permeate recovery in DCMD is 6.4% at a feed temperature of 60^{o}C. It is important to note that the data displayed in Figure 4.1(a) are just an example that may not correspond to actual MD systems in operation because there may be other factors that influence the required recycle ratio.

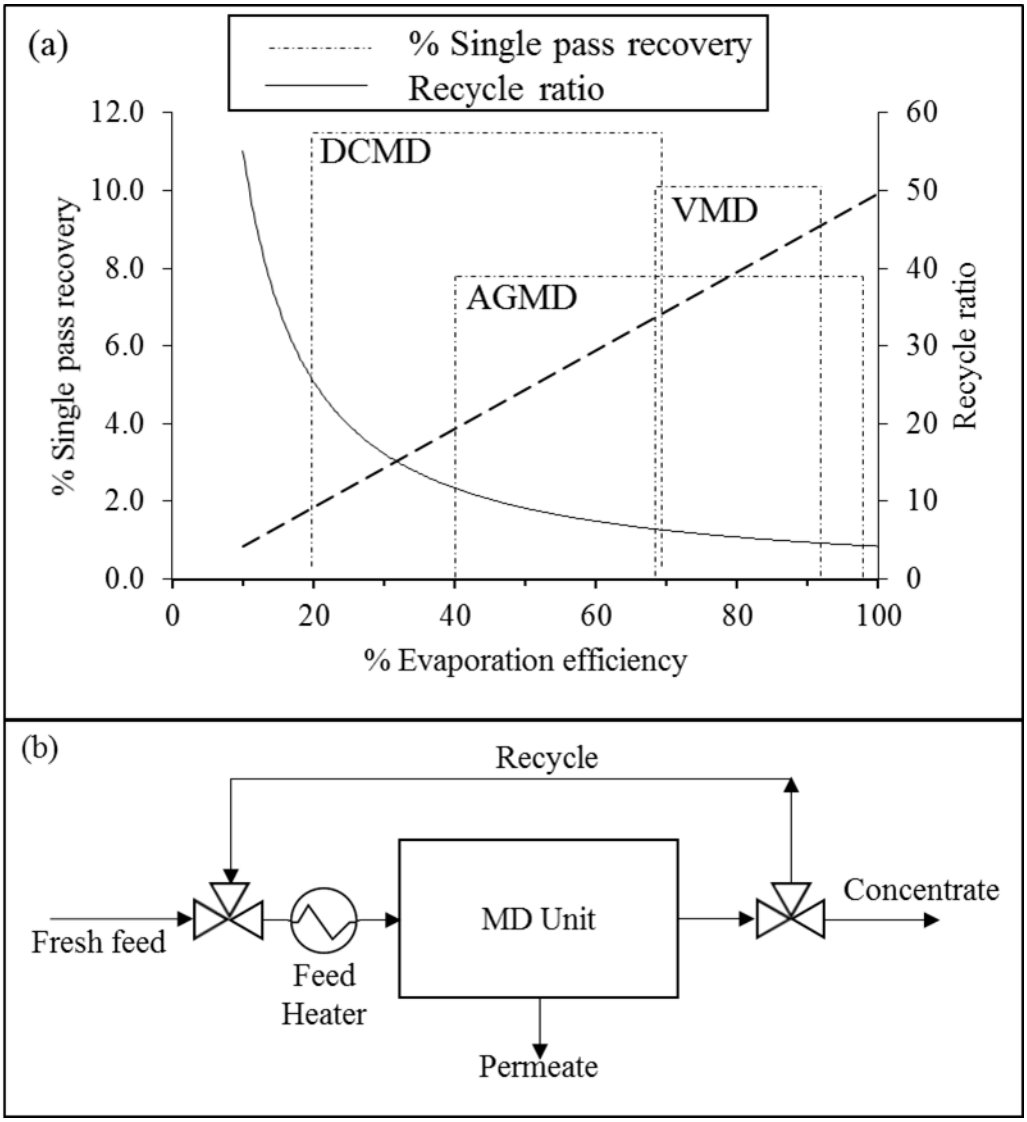

Figure 4.1. (a) Effect of evaporation efficiency on single pass permeate recovery of MD systems without heat recovery. The single pass permeate recovery was calculated for a hypothetical case when the feed enters MD at 90 oC and leaves at 40 oC. The recycle ratio was calculated for a sample case when the feed consists of 100 g/L of dissolved solids and is concentrated to 200 g/L through a continuous MD system shown in Figure 4.2(b) (i.e., 50% water recovery). The material balance calculations can be found in the Appendix A2. Single pass recovery was calculated by varying the evaporation efficiency in Equation 4.2. (b) Schematic diagram of a continuous MD system with recycle and concentrate streams.

A study conducted by Al-Obaidani et al. [137] analyzed the economics of a DCMD treatment plant designed to produce 24,000 m^3/day of pure water with a recovery factor of 80% using seawater as feed. The authors estimated the energy demand of this plant by calculating the energy required to raise the feed temperature from ambient conditions (i.e., 25 ^oC) to an operating temperature of 55 ^oC assuming that the system would be operated without any feed recycle. Based on these assumptions and specified plant characteristics, a specific thermal energy consumption (STEC) of 54.4 kWh/m^3 with respect to permeate can be calculated. As discussed above, it is not possible to achieve the recovery factor of 80% in any MD systems without feed recirculation. If a single pass permeate recovery of 5% and a DCMD feed exit temperature of 25 ^oC were assumed, the recycle ratio required to achieve 80% water recovery would be 15. In that case, the STEC with respect to permeate would be 697 kWh/m^3 even with 100% heat recovery because it is necessary to reheat the concentrate from 25 ^oC to the operating temperature of 55 ^oC after every pass through the MD module. This energy requirement is an order of magnitude greater than that calculated using the single pass approach discussed by Al-Obaidani et al. [137] and would greatly affect the overall economics of the system reported in that study.

Figure 4.2 shows a hypothetical case where the feed enters DCMD at 90 ^oC and is concentrated using a continuous DCMD system shown in Figure 4.1(b). The permeate flux was obtained for a membrane area of 0.2 m^2 using an ASPEN Plus simulation developed in a previous study [160]. Fresh feed with salt concentration of 100 g/L is assumed to be available at 20 ^oC and the final salt concentration reflects the concentrate characteristics. It should be noted that no heat recovery from the permeate stream was considered in these calculations. As seen in Figure 4.2(a), the STEC with respect to permeate decreased sharply with an increase in recycle ratio and eventually reached a plateau. Such behavior can be explained by the fact that the STEC is

comprised of thermal energy requirements of the feed heater, H_F, and the recycle heater, H_R, with the contribution of H_F being more significant at low recycle ratios. The STEC with respect to feed, however, increased steadily with increasing recycle ratio.

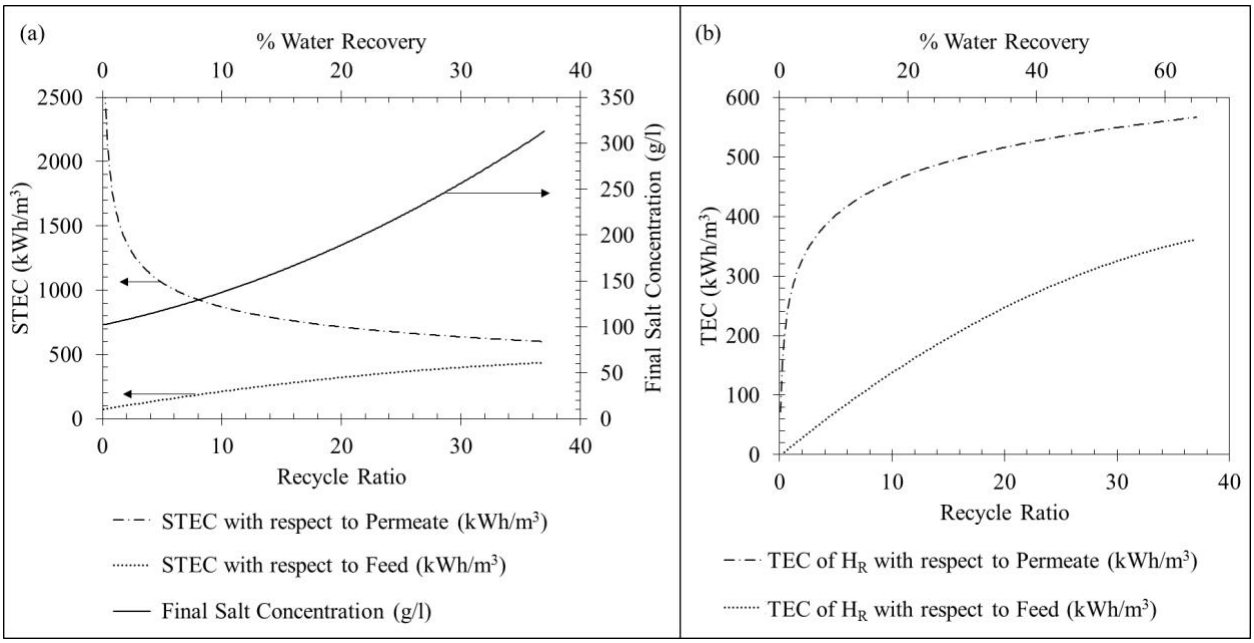

Figure 4.2. Hypothetical case showing the (a) The impact of recycle ratio on STEC with respect to feed and permeate, and (b) The impact of recycle ratio on thermal energy consumption (TEC) of recycle heater, H_R, with respect to feed and permeate for a continuous MD system shown in Figure 4.1(b) with 0.2 m^2 membrane area. The process was simulated for an MD module with a feed inlet temperature of 90 ^oC and flow rate of 1500 kg/hr and permeate inlet temperature of 30 ^oC and flow rate of 1500 kg/hr.

The 'final salt concentration' shown in Figure 4.2(a) increased with both water recovery and recycle ratio, which is due to the impact of water recovery on salt concentration in the concentrate as shown in Equation 4.4.

$$\frac{X}{X_o} = \frac{1}{1-\left(\frac{w}{100}\right)} \tag{4.4}$$

where, X is the concentration of salt in the concentrate, X_o is the salt concentration in the fresh feed and w is the desired water recovery. As can be seen from Equation 4.4, small changes in water recovery lead to large changes in the concentrate salt concentration and this effect is more pronounced at higher water recoveries. For instance, concentrating 100 g/L of feed to 200 g/L corresponds to a 50% water recovery and a STEC of 331 kWh/m^3 with respect to feed whereas concentrating a 200 g/L feed to 300 g/L corresponds to a water recovery of 33.3% and a STEC of 236 kWh/m^3 with respect to feed (not shown in Figure 4.2(a)). While the absolute increase in salt concentration across the MD module is equal in both cases, the difference in water recovery leads to different thermal energy requirements.

The effect of recycle ratio on the overall energy requirements in a DCMD system is not easily discerned from Figure 4.2(a) due to overwhelming contribution of the feed heater, H_F, towards the total thermal energy consumption at low recycle ratios. Hence, thermal energy consumption of the recycle heater, H_R, was calculated as a function of recycle ratio and is shown in Figure 4.2(b). As can be seen in this figure, the recycle ratio and water recovery have significant impact on the energy requirements of H_R. As the recycle ratio increases to 10, the total thermal energy requirement of the recycle heater increases to 460 kWh/m^3 of permeate and then levels off to approach 600 kWh/m^3 as the recycle ratio approaches 40. The increase in thermal energy requirements with respect to feed at low recycle ratios is not as dramatic but it approaches 380 kWh/m^3 of feed as the recycle ratio approaches 40. Since the recycled concentrate is at a lower temperature than the operating temperature of the MD feed stream, the recycled stream must be heated to the operating temperature, which adds to the overall thermal energy requirements of the system. This is true even when heat recovery systems are employed as it is not possible to achieve 100% heat recovery.

Thermal energy consumption is also influenced by the total dissolved solids (TDS) in the feed. For example, 50% water recovery for a feed stream with TDS of 100 g/L (i.e., Concentrate TDS = 200 g/L) requires 256 kWh/m^3 of feed for H_R (Figure 4.2(b)), whereas that when concentrating a feed stream with TDS of 150 g/L (i.e., Concentrate TDS = 300 g/L) requires 376 kWh/m^3 of feed (data not shown). This difference is due to a 31% decrease in evaporation efficiency when the feed TDS increases from 100 to 150 g/L, which decreases the single pass water recovery and increases the recycle ratio from 22 to 27, resulting in much higher thermal energy requirement for H_R. In addition, the specific heat capacity of the feed also influences the evaporation efficiency (Equation 4.1). For example, the specific heat capacity of NaCl solution at 90^{o}C decreases from 3.842 kJ/kgK at 100 g/L to 3.675 kJ/kgK at 150 g/L (ASPEN Plus database). This difference in specific heat capacity results in much lower enthalpy of NaCl solution at higher concentration. The specific enthalpy (i.e., enthalpy per unit mass) of NaCl solution at a reference temperature of 25^{o}C for example decreases from 249.8 kJ/kg at 100 g/L to 238.8 kJ/kg at 150 g/L. Because the latent heat of vaporization of NaCl solution remains constant irrespective of the salt concentration (i.e., 2285.13 kJ/kg at 90^{o}C, ASPEN Plus database), the solution with lower salt concentration will evaporate more water for the same reduction in specific enthalpy (or the same reduction in temperature) when compared to the solution with higher salt concentration (i.e., the solution with 100 g NaCl/L will evaporate 0.0048 kg of water more than the solution with 150 g NaCl/L for a temperature decrease of 65 ^{o}C).

In addition to energy required to reheat the concentrate stream, it is also important to take into account the electrical energy required to recirculate the concentrate stream when calculating the overall energy consumption in an MD system. Figure 4.3 shows the effect of recycle ratio on the specific electrical energy consumption (SEEC) due to additional energy required for pumping

the recycle stream through the MD system. The details of these calculations are included in the Appendix A2. As can be seen in Figure 4.3, the SEEC increases up to 2.9 kWh/m^3 of permeate when the recycle ratio approaches 40. Although the total amount of electrical energy required for concentrate recycling is quite small compared to the thermal energy required to reheat the concentrate, it may be important for the life cycle assessment of the MD system in terms of greenhouse gas emissions and other environmental impacts.

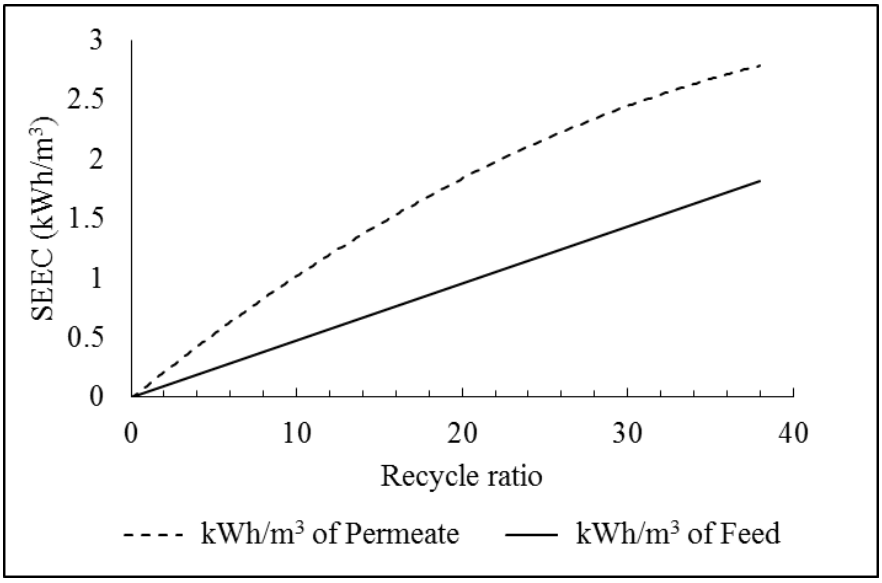

Figure 4.3. Variation of specific electrical energy consumption (SEEC) for pumping the recycle stream for the conditions shown in Figure 4.2. The electricity requirement was calculated assuming a pressure difference of 20 psi and a pump efficiency of 80% (Calculation method is shown in the Appendix A2).

4.4 CONCLUSIONS

Studies focused on MD seldom report the recycle ratio and its impact on the overall energy consumption of this process. A simple approach to estimate the single pass water recovery and the recycle ratio in an MD system based on the evaporation efficiency was used in this study to demonstrate the importance of recirculation on the overall energy consumption of a DCMD system. This study suggests that it is not possible to have a single pass recovery of more than 10%, even with 100% evaporation efficiency and that feed recirculation would be required if higher water recovery is desired. A previously developed ASPEN Plus model that uses fundamental heat and mass transfer equations to simulate DCMD performance was employed to study the effect of feed recirculation on the energy demand of this system. The results from this study indicate that the need for concentrate recycling accounts for a significant fraction of thermal and electrical energy in MD system. For example, an increase in the water recovery in a DCMD module with 0.2 m^2 of hydrophobic membrane with a membrane distillation coefficient of 5.6 LMH/kPa from 10 to 50% for a feed solution containing 100 g/L of NaCl would increase the required recycle ratio from 3 to 22 and a corresponding increase in thermal energy requirements of the recycle heater (H_R) from 39 to 256 kWh/m^3 of feed. This change in the water recovery also corresponds to an increase in the electrical energy consumption from 0.14 to 1.05 kWh/ m^3 of feed.

This study also illustrates that an increase in feed salt concentration reduces evaporation efficiency and single pass water recovery, which increases the recycle ratio required for a given overall water recovery. A 10% water recovery using MD when the feed contains 100 g/L of dissolved salts has significantly lower energy requirements for H_R (58 kWh/m^3 of feed and a recycle ratio of 4) than that when the feed contains 250 g/L of dissolved salts (90 kWh/m^3 of feed and a recycle ratio of 8). Specific heat capacity of the feed was also identified as a factor that

influences system performance because the lower salt concentration in the feed results in greater water evaporation for the same reduction in specific enthalpy or the same reduction in temperature. It is recommended that future laboratory and pilot-scale MD studies should include information on single pass conversion and recycle ratios needed to achieve a desired water recovery as their impact on energy consumption is critical to provide accurate assessment of operating costs and improve the performance of MD systems.

5.0 CONCENTRATION POLARIZATION IN DIRECT CONTACT MEMBRANE DISTILLATION: DEVELOPMENT OF A LASER-BASED SPECTROPHOTOMETRIC METHOD FOR ITS CHARACTERIZATION

Membrane-based processes have gained prominence for environmental and industrial separations, especially in water purification and desalination. In spite of these developments, a fundamental knowledge gap exists with regards to fully understanding the processes that occur at or near the membrane surface. Concentration polarization is a phenomenon that may have a significant impact on mass transfer and formation of solids on the membrane surface. While attempts have been made to experimentally characterize this phenomenon for pressure-driven filtration processes, most studies employ semi-empirical methods to estimate the extent of concentration polarization without actually measuring the concentration of solute near the membrane surface. In addition, the methods developed to study concentration polarization in membrane processes have not been applied to membrane distillation when treating saline wastewaters. This study presents a novel spatially resolved non-intrusive spectrophotometric method developed to measure the concentration profile of solute near the membrane surface in a direct contact membrane distillation system. A custom membrane cell was designed and fabricated for this study which allowed passage of light across the feed channel. This spectrophotometric method was developed and validated using transition metal salt (nickel chloride) in the feed solution to detect the concentration gradient near the membrane surface. The method developed in this study can be extended to other

membrane-based separation processes that experience concentration polarization and for different solutes if the absorption spectra of the solute is known.

5.1 INTRODUCTION

Membrane Distillation (MD) is a thermal separation process that is driven by the vapor pressure difference across a hydrophobic membrane. MD employs hydrophobic membranes with a high liquid entry pressure (LEP), which prevents the passage of water through the membrane when the feed pressure is below the LEP. This process can achieve complete rejection of ions and non-volatile organics as long as the membrane pores are not wetted. MD has immense potential in the desalination of high salinity wastewaters where reverse osmosis is not feasible. As MD is a thermal separation process, polarization effects include both temperature and concentration polarization. The effect of temperature polarization on MD performance has been studied extensively in the past [81, 82]. However, concentration polarization has not been studied in great detail when evaluating MD performance. This is partly because most studies were conducted at low salt concentrations where concentration polarization does not result in a significant mass transfer resistance [81, 94, 165]. Previous work on treatment of high salinity produced water from unconventional gas extraction has shown that the concentration of salts at the membrane surface can be up to 30% higher than that in the bulk when the feed solution approaches saturation conditions [124].

Concentration polarization has been linked to membrane scaling or fouling and can greatly influence the overall performance of membrane-based separation processes [166]. Several studies have been focused on experimentally measuring the concentration polarization [166-168] for pressure driven membrane processes. Refractive index is one of the several properties of a solution

that is affected by the concentration of solutes. Vilker et al. [169] employed an optical shadowgraphic method to measure the change in refractive index of the solution due to concentration gradient for an unstirred dead end ultrafiltration system with bovine albumin serum as the solute. Ethier and Lin [170], and Gowman and Ethier [171, 172] also applied the optical method based on the variation in refractive index to measure the concentration profile of hyaluronic acid in an unstirred dead-end ultrafiltration system. These optical methods were able to measure the concentration profile of the solute to about 100-200μm above the membrane surface. While the resolution obtained by these optical methods was satisfactory, this method cannot be applied to membrane distillation where the presence of temperature polarization can interfere with the refractive index measurements, as refractive index varies with temperature [173].

Holographic interferometry has also been employed as another optical method to evaluate the concentration profile for flat sheet reverse osmosis [174, 175] and ultrafiltration systems [176, 177]. Several studies also reported the use of nuclear magnetic resonance (NMR) imaging to obtain the concentration profile for oil-water emulsion [178, 179] and silica colloidal suspension in water [180] when studying cross-flow hollow fiber microfiltration systems. While NMR requires complex instrumentation, it is a powerful tool which can characterize the concentration profile of colloidal systems with a spatial resolution of up to 10 μm [166]. McDonogh et al. [181] employed a radio-isotope labeled protein to measure the concentration of protein accumulated near the membrane surface using a scintillation detector. This method suffered from the fact that the solute under study needed to be labelled with a radio isotope. Hence, this technique could only be applied for specific solutes which could be labelled with a radio isotope and was not applicable for all types of solutes. The same group of researchers also developed an electronic diode array microscope (EDAM), which uses a collimated near infrared beam of light channeled across a flat

sheet micro-filtration cell to measure the concentration profile of dextran blue in water [181]. The concentration of solute (dextran blue) was measured by the intensity of light detected by a CCD detector. While this technique was very simple and effective, the authors reported up to 23% relative error in the measurement of concentration. The authors of that study [181] also did not compare their results with theoretical models of estimating concentration polarization. Kroiß et al. [167] described three optical methods to measure the concentration profile in membrane distillation and reverse osmosis. However, experiments were only conducted with a reverse osmosis setup to check the validity of the proposed methods. Although studies available in the literature have been focused on measuring the solute concentration profile for pressure driven membrane systems, no study has attempted to measure the concentration polarization in membrane distillation, especially when operating with high salinity feed solution.

This study is focused on developing a simple optical technique to measure the concentration of solute in the concentration polarization layer in a direct contact membrane distillation (DCMD) system. To achieve this objective, a visible spectrophotometer with a spatial resolution of 4.5 μm was developed based on the optical method used by McDonogh et al. [181] using a collimated laser beam as the light source and a CCD line camera as the detector. A membrane cell with a transparent feed channel was constructed to measure the concentration of solute near the membrane surface and within the boundary layer of the feed stream. The DCMD module was mounted on adjustable support to precisely position it between the light source and the detector such that the incident light is parallel to the membrane surface and the transmitted light is captured by the detector. The entire experimental system was mounted on an optical breadboard with passive dampeners to reduce impact of vibrations on the spectrophotometric analysis. Light absorption near the membrane surface that is proportional to the concentration of

dissolved ions was used to analyze their concentration. The optical system developed in this study presents a simple yet powerful method of characterizing concentration polarization in membrane-based systems.

5.2 MATERIALS AND METHODS

5.2.1 Detection of concentration polarization by visible light

A DCMD cell with a transparent feed channel was fabricated to facilitate measurement of solute concentration near the membrane surface and within the boundary layer on the feed side of the membrane module. The cell was equipped with a custom spectrophotometer and mounting system that facilitated positioning of the light source and the detector parallel to the membrane surface and perpendicular to the direction of feed flow. A schematic diagram of the principle of operation is shown in Figure 5.1. The DCMD cell was positioned between the light source and the detector such that the incident light is parallel to the membrane surface and the transmitted light was captured by the detector.

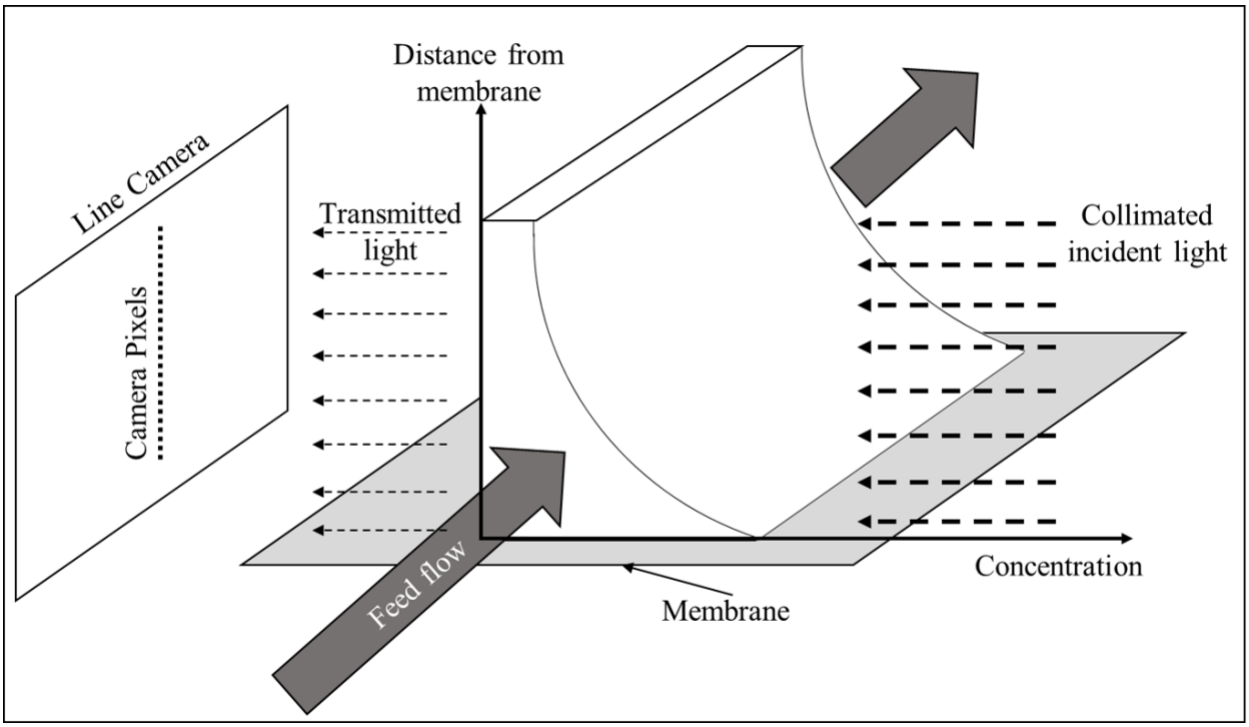

Figure 5.1. Schematic diagram of the optical setup used for measuring the concentration of solute close to the membrane surface. The light rays pass through the hydrodynamic boundary layer where it is partially absorbed by the solute and the transmitted light is captured by the detector.

5.2.2 Solute selection

Most MD studies are focused on separation of salts from water with sodium chloride as the dominating salt [61, 160, 182]. While sodium chloride would be an ideal salt for this study, it exhibits a negligible change in absorption with varying concentration [183, 184]. Hence, as transition metals absorb light in the ultraviolet and visible (UV-Vis) spectrum [185], transition metal chloride salts, namely cobalt chloride ($CoCl_2$), copper chloride ($CuCl_2$) and nickel chloride ($NiCl_2$), were initially selected for measuring concentration polarization with the proposed method. The metal salts were obtained from Acros Organics (New Jersey, USA). Preliminary absorbance measurements of these salts were obtained by using a UV-Vis Spectrophotometer (Genesys 10S,

Thermo Fisher Scientific, Waltham, MA) in the wavelength range of 200 to 1100 nm. The data obtained from the Genesys 10S system was utilized only to select a single salt that could be used in the optical system.

5.2.3 MD cell

Figure 5.2 shows the cross-sectional side view and the top view of the membrane cell. The membrane cell was fabricated from clear acrylic material. The membrane was sandwiched between two acrylic halves which were lined with a thin layer of PTFE (Teflon) tape. The PTFE tape acted as a gasket to seal the two halves of the cell. As concentration polarization occurs near the membrane surface, it was necessary to construct a transparent channel for the feed in the vicinity of the membrane to facilitate the passage of light for probing this layer. Hence, the channel in the top half of the cell was open along the length while the bottom half of the cell was similar to a conventional membrane cell. The hydrophobic microfiltration membrane was secured in place by folding around the bottom half of the cell. Shims with different thicknesses were cut for both halves of the cell to adjust the channel depth and secured in their position using flat head screws.

As the channel in the top half of the cell was open, a transparent side was needed to contain the liquid inside. Hence, the two halves of the acrylic cell were sandwiched between $1/8^{th}$ inch glass plates, which were lined with a silicone gasket along the edges. The glass plate was secured to the cell using metal holding plates with opening in the center. The metal plates were fixed to the two halves of the cell using screws. The opening in the metal plate allowed light to pass through the feed channel (i.e., the channel formed by the top half of the membrane cell). It should be noted that the metal plate, too, was lined with a silicone gasket. The purpose of this gasket was to provide

uniform pressure against the glass plate so that the glass plate does not crack or break when the metal plate was tightened using screws.

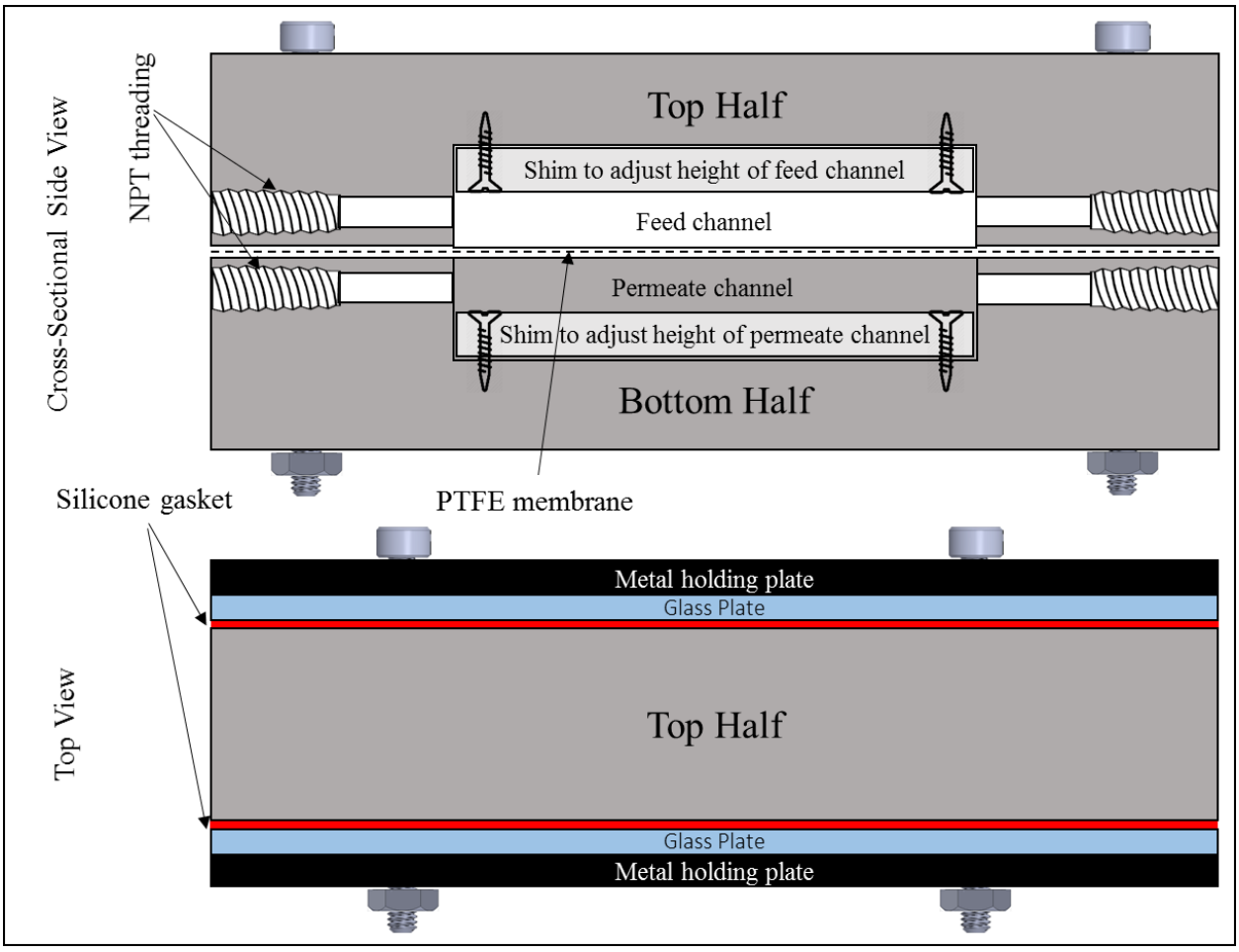

Figure 5.2. Cross-sectional side view and top view of the membrane cell.

The membrane cell was assembled by first tightly wrapping the membrane around the bottom half of the cell. Next, the top half of the cell was secured using nuts and bolts while making sure that the membrane surface was visibly flat and devoid of any kinks. Glass plates lined with a silicone gasket were then secured on the sides of the membrane cell with the metal holding plate using screws. The whole cell was secured to a metal mounting plate which rested on thumbnuts

attached to threaded studs. The thumbnuts were used to ensure that the position of the cell did not change throughout the experiments. The threaded studs were fixed to the optical breadboard (MB1218, Thorlabs, Newton, NJ). This arrangement acted as a gimbal which was used to position the membrane parallel to the beam of light passing through the top half of the membrane cell. A 3D figure of the membrane cell can be seen in Figure 5.3.

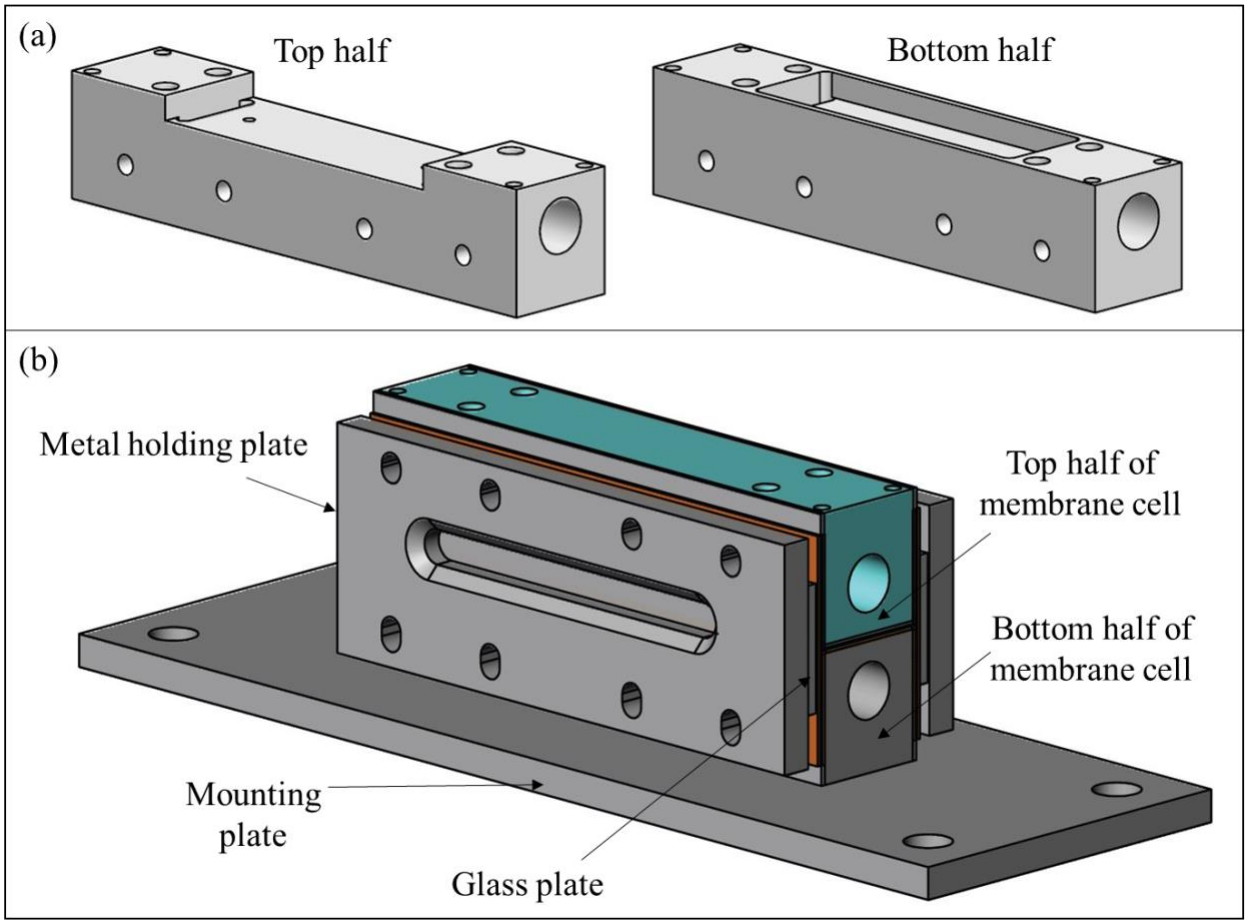

Figure 5.3. 3-D illustration of the (a) top and bottom half of the membrane cell, (b) assembled membrane cell mounted on the metal mounting plate.

A 0.2µm pore size polytetrafluoroethylene membrane with a polypropylene support, obtained from Sterlitech (Kent, WA), was used for all the experiments in this study. A spacer was

used on the permeate side, while the feed channel was open without any spacer. The channel dimension was 24mm x 70mm with a depth of 5mm on the feed side and 20mm x 70mm with a depth of 1mm on the permeate side. The characteristics of membrane and spacer are shown in Table 5.1. The feed channel was painted black from inside to prevent light scattering and reflection within the channel.

Table 5.1. Characteristics of spacer and membrane used in this study.

Spacer thickness (mm)	1
Filament thickness (mm)	0.5
Spacer angle	90^{o}
Mesh size (mm)	1.6
Spacer porosity	0.75
Membrane mass transfer coefficient (LMH/kPa)	4.4 [124]

5.2.4 Light source and collimation

Light emitting diode (LED) having a 660 nm wavelength (LED660L, Thorlabs, Newton, NJ) was initially selected as the light source for the optical setup. However, as the LED was not a true point source, the collimation of LED was poor resulting in a slightly diverging beam. Due to beam divergence it was not possible to obtain a beam parallel to the membrane surface. A laser source, which acts as a true point source, with a wavelength of 670 nm (CPS670F, Thorlabs, Newton, NJ) was therefore selected for this application. Laser light emitted from the laser diode was collimated by a spherical lens into the free space. The collimated beam had an elliptical beam profile with the ratio between its two semi-major axes of 4.6. The beam was reflected twice by two silver mirrors

with horizontal and vertical tilt adjustability. The two mirrors together enabled full control of the position and angle of the laser. The resulting beam was focused onto a single mode fiber by another spherical lens. The laser beam was simply focused onto the fiber core for coupling regardless of the shape and spot size of the beam spot. This is because the laser used in this setup delivered sufficient intensity exiting the fiber even with a low coupling efficiency. Improvement of the coupling efficiency can be made by using anamorphic prisms to change the beam profile to a spherical shape and adjust the beam spot size to fill the fiber core after focusing. The beam size can be changed by adding a pair of lenses configured as a telescope. The schematic representation of the optical assembly used in this work for coupling the beam is shown in Figure 5.4. The beam exits the single mode fiber from the other end into the experimental setup. It is again collimated and propagated into free space using a fixed collimation lens (F810FC-780, Thorlabs, Newton, NJ) which had a coupling beam diameter of 7.5 mm. The use of single mode fiber allowed the laser source assembly to be isolated from the main optical system. Moreover, since the single mode fiber is designed to carry a single wavelength of light, all other wavelengths are prevented from entering the setup.

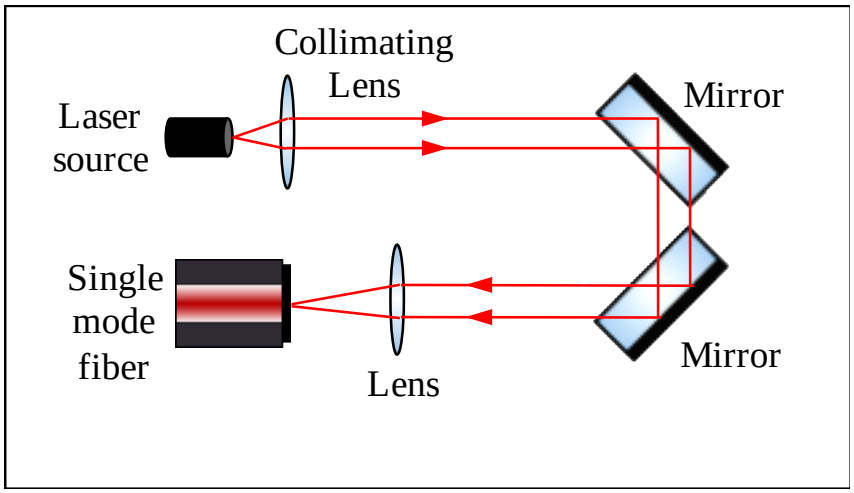

Figure 5.4. Schematic representation of the assembly used to obtain the laser source in a single mode optical fiber.

The intensity of light registered by the high sensitivity CCD line camera (Thorlabs LC100) when using LED and laser as the light source is shown in Figure 5.5. In Figure 5.5, the x-axis denotes the camera pixel number, which represents the position of each individual sensor of the camera (i.e., also known as pixel). The figure shows that beam intensity was not uniform for the LED and exhibited an unstable intensity profile. The laser, however, resembles a Gaussian beam with a relatively smooth profile.

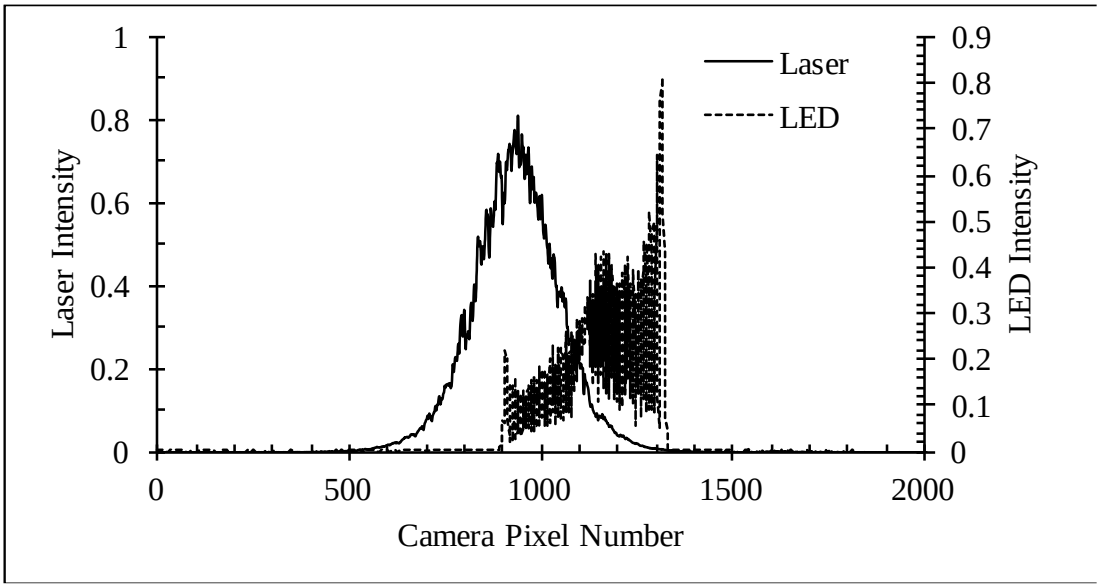

Figure 5.5. Comparison between the LED and laser patterns when the membrane cell was absent

5.2.5 Experimental System

All the components of the optical setup were obtained from Thorlabs (Newton, NJ). The schematic of the optical setup is shown in Figure 5.6. As discussed above, a fiber coupled laser with a wavelength of 670 nm was used as the light source. The laser was collimated by using a fiber collimation package (Thorlabs F810FC-780) which provided an output laser beam with a 7.5 mm diameter. The collimated beam was directed to an iris and absorptive neutral density (ND) filters before entering the membrane cell. The iris was used to control the size of the beam that entered

the membrane cell, while the ND filters blocked a fraction of light to ensure that the camera pixels were not saturated. A set of ND filters with absorbance ranging from 0.3 to 3 were used to adjust the intensity of light detected by the camera. For each set of experiment, the ND filter arrangement was kept constant to avoid any variation in the light path. A set of lenses with focal lengths of 30mm and 100mm (Lens1 and Lens2, respectively, in Figure 5.6(a) were used to magnify as well as focus the light rays entering the camera. As shown in Figure 5.6 (b), the lenses were held together through an adjustable length lens tube which was mounted directly onto the camera. The lenses were arranged such that the focal plane of lens 1 (see Figure 5.6 (a)) was close to the edge of the membrane cell, while that of the lens 2 was on the camera pixels. This arrangement enabled a sharp image on the camera with a 3x zoom which was then recorded as an intensity profile. The camera used for this application was a high sensitivity CCD line camera with 2048 pixels arranged vertically in a single line. Each pixel had a width of 56µm and a height of 14µm. The camera integration time, which is the duration for which the pixels are exposed to light, could be varied from 1ms to 50s and could detect wavelength in the range of 350-1100 nm. The setup was mounted on an optical breadboard (MB1218, Thorlabs) with sorbothane feet (AV4, Thorlabs) which acted as dampeners to reduce the impact of vibrations. The whole assembly was covered in a box lined with a light absorbing black paper from inside to prevent stray light from entering the setup.

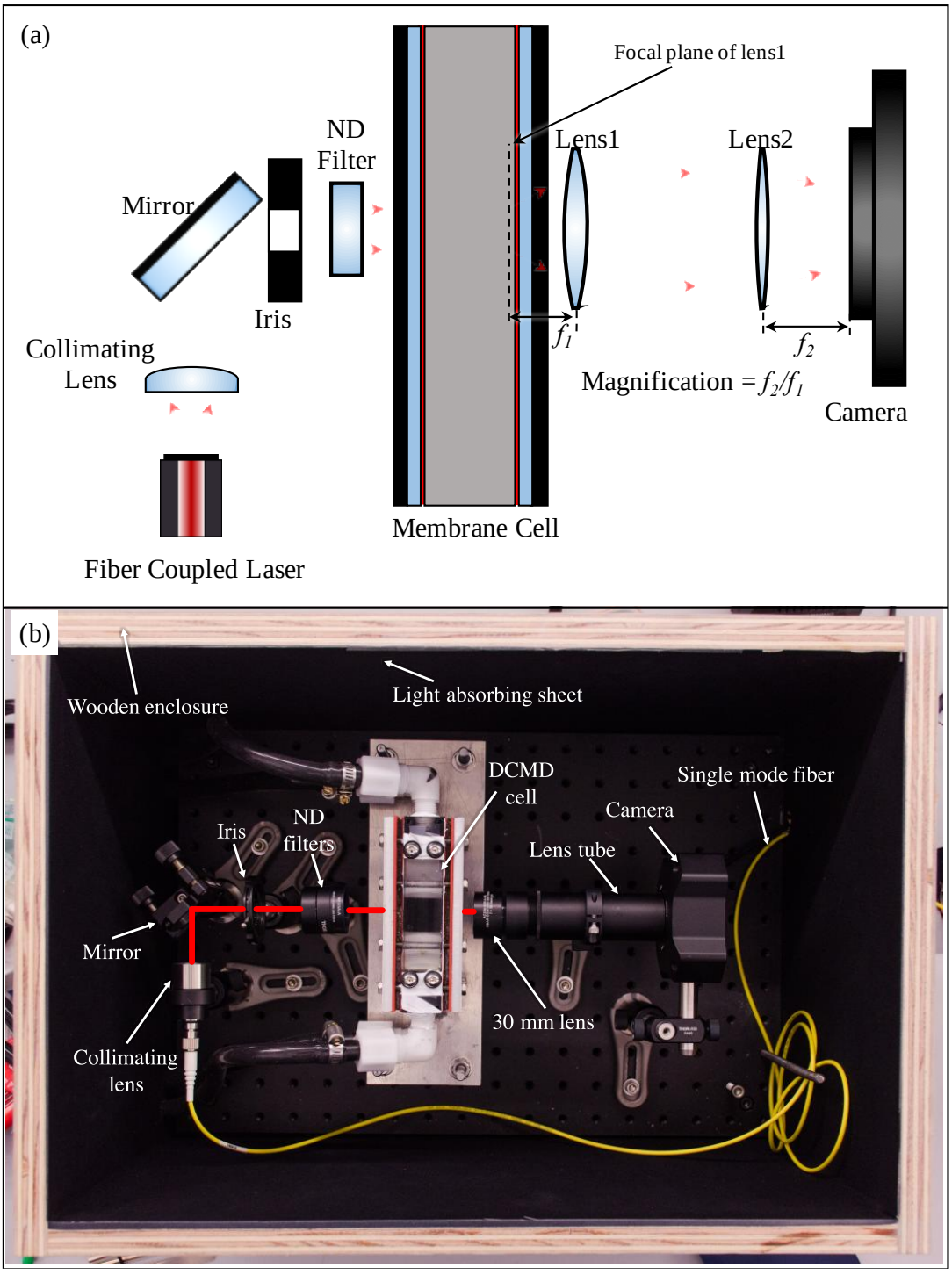

Figure 5.6. (a) Schematic diagram of the experimental optical setup, (b) picture of the experimental setup.

Due to the 3x zoom obtained by the lens system, each camera pixel was estimated to measure about 4.7 μm (i.e., one third of the 14 μm height of each pixel) of the image. A micrometer scale (MR095, Amscope, Irvine, CA) with a least count of 10 μm was used to calibrate the distance corresponding to each camera pixel and calculate the actual magnification obtained through the lens system. It was found that each pixel on the camera corresponded to 4.5 μm of vertical distance with respect to the membrane surface. Therefore, the actual magnification of the camera was in fact 3.1x (i.e., 14/4.5), which is very close to the expected magnification of 3x.

The experimental system for DCMD was similar to a previous study [124] and showed highly reproducible experiments with a maximum standard deviation of ±0.3 LMH in the permeate flux. All the DCMD experiments were carried out in a countercurrent manner with a flat sheet membrane. Black pipes were used for connecting the membrane cell to the pumps and feed and permeate tanks to avoid stray light from entering the setup. The pipes passed through the walls of the box, which contained the optical parts, with minimum clearance to prevent any stray light from entering the setup.

5.2.6 Membrane positioning

Positioning the membrane surface parallel to the collimated laser beam is critical to enable measurement of solute concentration close to the membrane surface. As shown in Figure 5.7, a significant portion of the incident light is blocked by the membrane and fewer pixels in the camera are able to detect light when the membrane is not completely parallel to the beam of light (Figure 5.7(a) and (b)). However, for a given direction of light path, there exists a membrane position when maximum number of pixels are exposed to the incident light. This position marked the position of membrane when it was parallel to the light rays (Figure 5.7 (c)). To achieve such alignment, the

membrane cell was incrementally tilted along the longitudinal axis in both directions while monitoring the intensity patterns recorded by the camera. Optimal positon of the cell was achieved when maximum number of pixels on the camera detected the light and tilting the membrane cell in any direction from this position resulted in blocking of light rays.

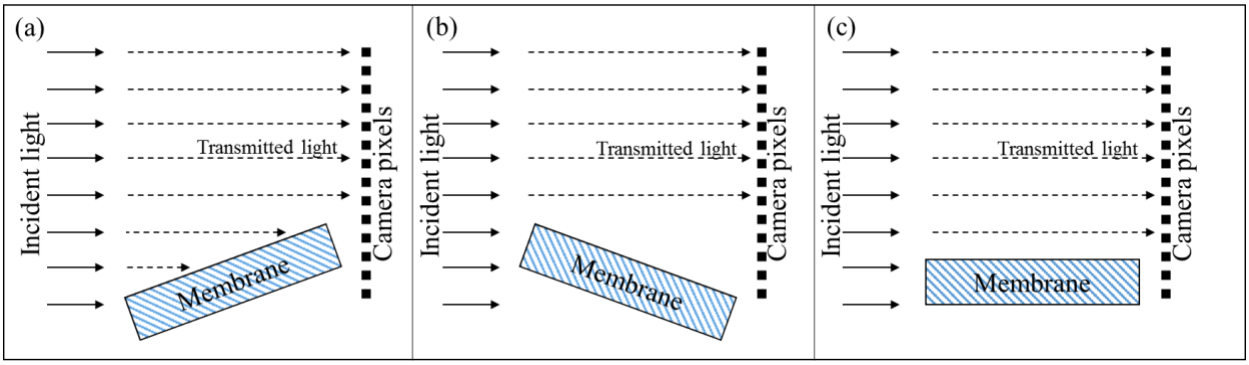

Figure 5.7. Schematic representation of light path when (a-b) membrane is tilted and (c) membrane is parallel to the beam of light.

5.3 RESULTS AND DISCUSSION

5.3.1 Solute selection

As mentioned before, the Genesys 10S UV-Vis spectrophotometer was used for salt selection among several transition metal salts. The UV-Visible spectrum obtained from Genesys 10S for different transition metal salts has been shown in Appendix A3. The UV-Visible spectrum of copper chloride (shown in Appendix A3) showed a very high absorbance at wavelength below 400 nm and above 600 nm. The absorption was so high (i.e., greater than 3) that the spectrophotometer was not able to provide accurate results beyond a concentration of 25 g/L. Cobalt chloride

exhibited an absorbance of 0.075 to 1.95 in a narrow range of wavelength (about 450 to 550 nm) when the concentration varied up to 55 g/L. Nickel chloride (Figure 5.8), on the other hand, showed high absorbance at 400 nm and a much lower absorbance in the wavelength range of 600 - 800 nm. The absorbance of light by nickel chloride solution with respect to concentration and the correlation between absorbance and concentration at specific wavelengths is shown in Figure 5.8. Copper chloride showed much greater variation of absorbance with concentration, which would be beneficial in detecting small changes in the solute concentration. However, very high absorbance meant that the light detector (i.e., camera) would need to have a very high dynamic range to provide accurate results throughout the entire concentration range that was selected for this study. While Cobalt chloride showed absorbance similar to nickel chloride, the range of wavelength in which cobalt chloride exhibited absorbance was very narrow resulting in a limited choice in the selection of light source for the optical method. Relatively low absorbance of nickel chloride in a much broader visible wavelength range (i.e., 600 - 800 nm) as well as a linear change in absorbance with a very high coefficient of correlation (shown in Figure 5.8 (b)) was the main reason why nickel chloride was chosen for this study.

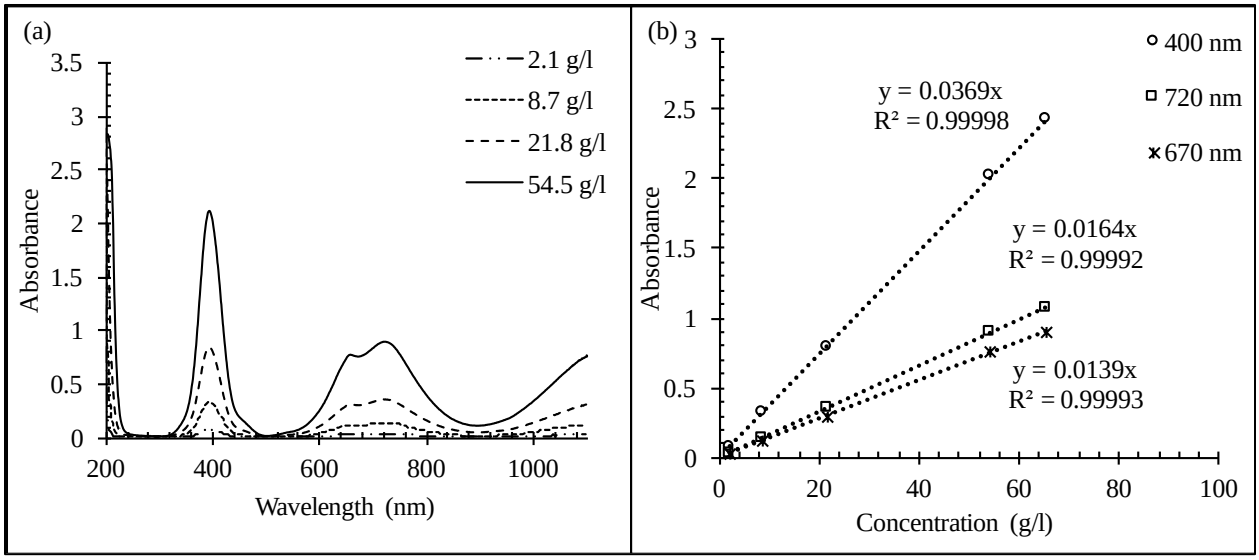

Figure 5.8. (a) UV-visible absorption spectra for nickel chloride in de-ionized water, (b) correlation between light absorbance and nickel chloride concentration at different wavelengths.

5.3.2 Light absorbance in MD cell

The refractive index of a salt solution changes with varying salt concentration [186]. As the change in refractive index can lead to variation in the direction of light while traveling through different phases, i.e. air to glass to liquid in the membrane channel in this case, it was important to analyze the magnitude of this variation at different salt concentrations that will be used in this study. The change in the light pathway due to change in concentration of solute (i.e, drift) was analyzed by recording the intensity pattern of light observed by the camera at varying nickel chloride concentrations. The membrane cell was first positioned between the light source and camera and the membrane was aligned parallel to the path of laser. A change in the light direction can be detected more effectively if a small beam of laser is used. Hence, a 1.5 mm collimating lens was used in this case so that the whole beam could pass through the membrane cell (as the channel height was 5 mm) and distinguishable peaks would be recorded by the camera. Any change in the

direction of light due to changing concentration would result in a shift in the peaks recorded by the camera. Nickel chloride solution in the concentration range from 40 to 65 g/L was pumped through the membrane cell at room temperature and flow rate of 0.5 liter/min (LPM). The light intensity detected by the camera for varying solute concentration is shown in Figure 5.9. As expected, the light intensity reaching the camera decreased with increasing salt concentration due to absorption of light by the salt. However, the absence of any shifting of intensity peaks meant that the changing refractive index due to changing solute concentration did not affect the path of the light and the light rays were perfectly perpendicular to the membrane cell.

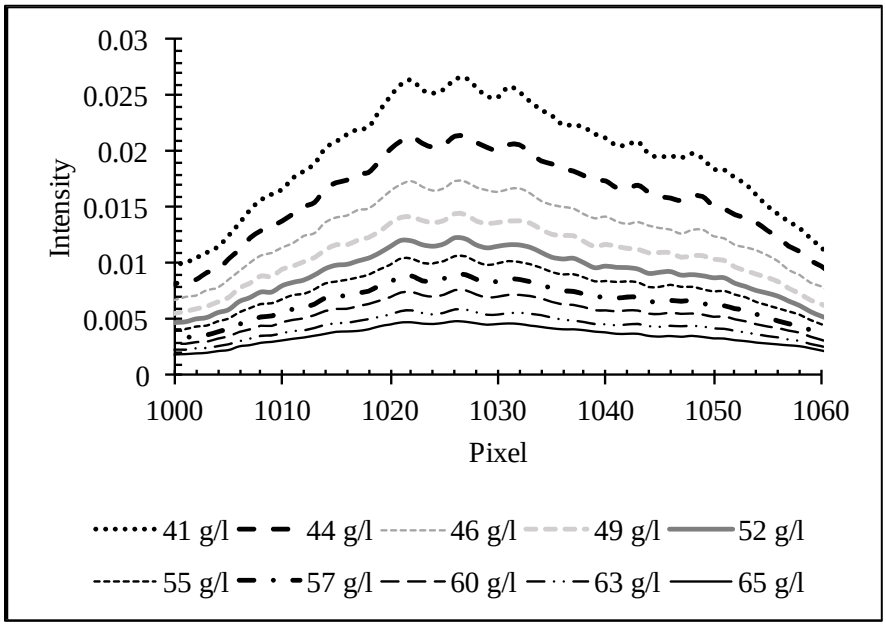

Figure 5.9. Light intensity recorded by the camera for varying nickel chloride concentrations flowing through the feed channel (Temperature = 23 ^{o}C; Feed flow rate = 0.5 LPM; Permeate flow rate = 0.2 LPM).

5.3.3 Effect of temperature and flow rate on absorbance

In addition to concentration polarization, DCMD also exhibits temperature polarization which results in a temperature gradient near the membrane surface [187]. Hence the absorbance measurements using the optical method needed to be unaffected by the temperature of the feed solution. Moreover, the flow rate of feed would also be significantly lower near the membrane surface and within the boundary layer and the absorbance measurements needed to be unaffected by the feed flow rate too. Hence, to evaluate the effect of temperature and flow rate on absorbance measurements, several tests were carried out with the 7.5 mm collimating lens at experimental conditions relevant for the operation of DCMD module. Figure 5.10 shows the absorbance as a function of $NiCl_2$ concentrations at varying feed temperatures and flow rates across the feed channel. The calibration curves shown in Figure 5.10 were obtained for triplicate results at each temperature and flow rate. The following equation was used to obtain the light absorbance of the salt solutions [188]:

$$Absorbance = \log\left(\frac{I_o}{I}\right) \tag{5.1}$$

where, I_o is the intensity of light recorded when the feed channel was filled with deionized water and I is the intensity of light recorded when the feed channel was filled with salt solution. Although the variation in feed temperature and flow rate had virtually no impact on absorbance as indicated by almost identical slopes at different temperatures, statistical analysis was carried out to investigate the level of variation in the absorbance measurements due to these factors. The results from the statistical analysis are shown in the Appendix A3. According to the analysis, the variation in the absorbance due to changing temperature and flow rates was less than 8% in all the cases studied in this work. Hence, the effect of feed temperature and flow rate is regarded as completely

random and bulk feed concentration will be considered as the only factor affecting the measurement of absorbance values. Additionally, to prevent any errors in measurements due to changing temperature or flow rates, calibration curves (i.e., absorbance vs concentration) were generated for each experiment that was carried out with the optical setup.

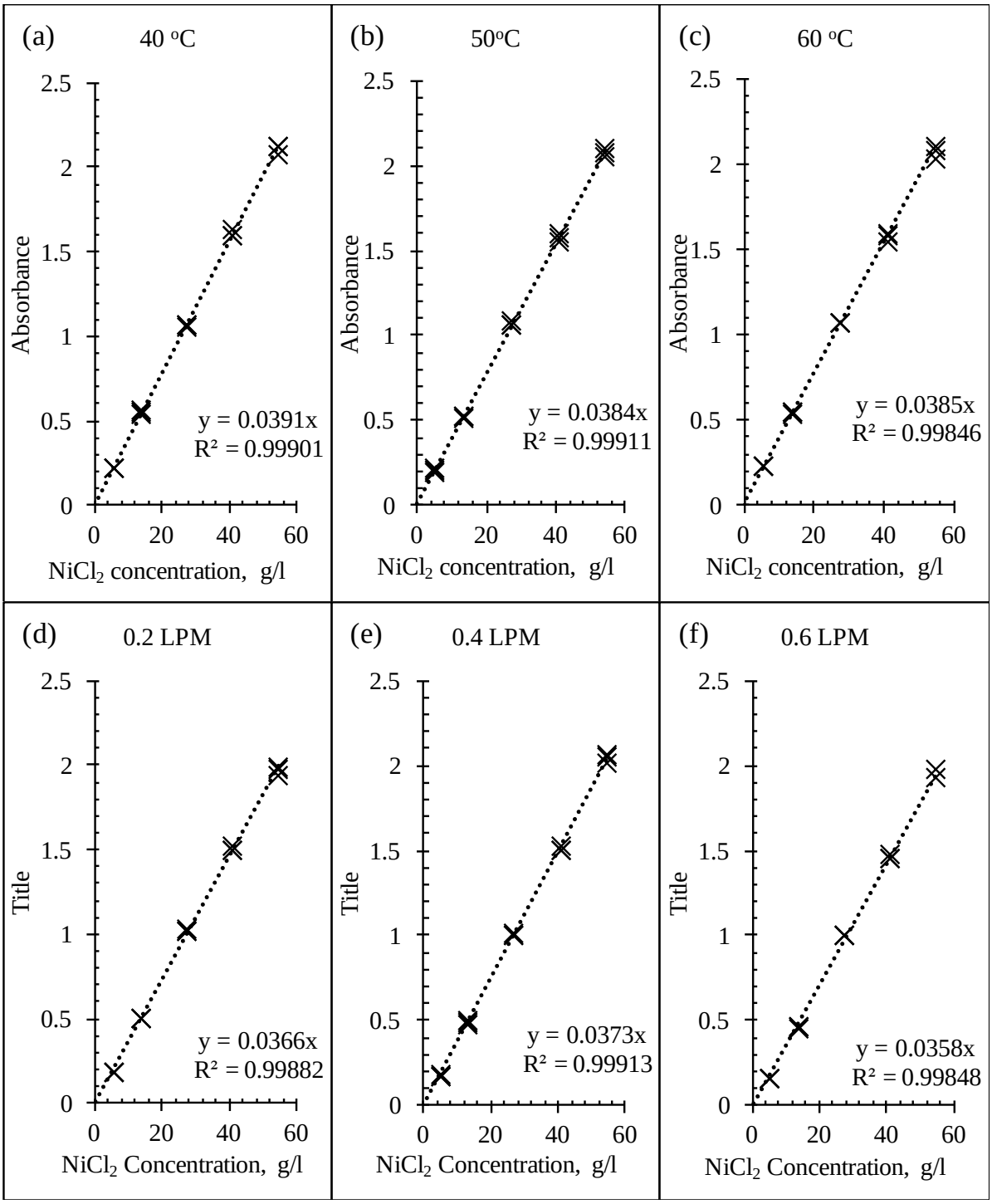

Figure 5.10. Correlation of absorbance with nickel chloride concentration at feed temperatures of (a) 40 °C, (b) 50 °C and (c) 60 °C when the feed flow rate was 0.5 LPM and at feed flow rates of (d) 0.2 LPM, (e) 0.4 LPM and (f) 0.6 LPM when the feed temperature was 50 °C.

5.3.4 Evaluating the concentration gradient in MD cell

DCMD experiments at a feed temperature of 60^{o}C and feed flow rate of 0.5 LPM were carried out to evaluate the solute concentration profile using the optical system developed in this study. The permeate-side temperature and flow rate were maintained at 20^{o}C and 0.2 LPM, respectively. Pure water was initially supplied on the feed side of the cell at 60^{o}C to record the light intensity pattern which would be used as the reference for absorbance calculations. Salt solution was then introduced at the feed temperature of 60^{o}C to obtain the concentration profile near the membrane surface. Figure 5.11 shows the concentration profile obtained with the optical setup when the feed concentration was varied from 27.3 g/L to 54.5 g/L. The x-axis, in Figure 5.11, represents the distance from the membrane surface in to the bulk feed stream. As mentioned above, a micrometer scale was used to evaluate the actual scale of measurement. The pixels were converted into distance by means of this scale (one pixel was equivalent to 4.5 μm of vertical distance from the membrane surface). To obtain the concentration of solute shown on the y-axis in Figure 5.11, the intensity recorded by the camera at different solute concentrations was first converted to absorbance by Eqn. 1. The absorbance was then converted to concentration by using the calibration curve shown in Figure 5.10.

As shown in Figure 5.11, the concentration of $NiCl_2$ is significantly higher at the feed-membrane interface. For instance, at a feed concentration of 54.5 g/l, the concentration of solute at the feed-membrane was 80 g/l, i.e. 47 % higher than the bulk feed concentration. The concentration gradient can be clearly seen at all three concentrations. At feed concentrations in excess of 100 g/l, the intensity could not be recorded by the camera without removing the ND filters. Removing the ND filter would mean that the light path would be slightly altered. This was important as all the intensity profiles recorded by the camera were compared to pure water intensity

profile (which needed ND filters in order to prevent saturation of camera pixels). Hence, the intensity profile at concentrations beyond 100 g/l without ND filters could not be compared with the intensity of pure water with ND filters. The feed concentration was therefore limited to 100 g/l to accurately measure the concentration of salt at the membrane surface.

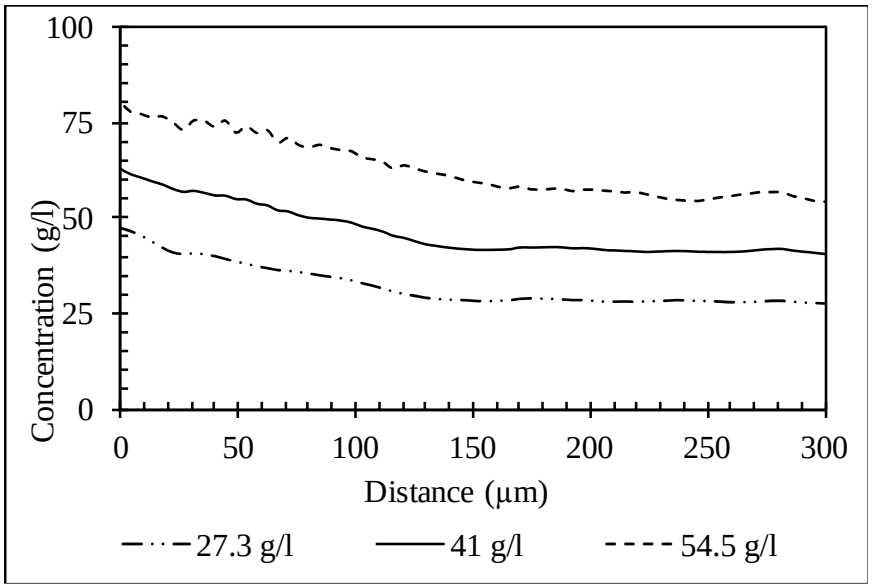

Figure 5.11. Concentration profile of $NiCl_2$ near the membrane surface. The feed and permeate flow was 0.5 and 0.2 LPM respectively, while the feed and permeate temperatures were maintained at 60 and 20 ^{o}C respectively.

This work demonstrates the capability of a novel spectrophotometric method for evaluating the concentration polarization phenomenon in membrane processes. The technique developed in this study can measure the concentration of nickel chloride solutions up 100 g/l and can be used for studying concentration polarization in other membrane based processes and for other solutes which absorb light. An important aspect of this technique is that it is unaffected by the temperature of feed solution, which has not been addressed in studies focused on developing such concentration measurement techniques within the boundary layer. As a continuation of this study will be, a future

work will be focused on nickel chloride concentrations below 100 g/L to study the dynamics of concentration polarization where the impact of feed flow rate, temperature and salt concentration on the concentration polarization layer will be evaluated. In addition, the experimentally obtained concentration polarization coefficient and the thickness of the polarization layer will be validated against semi-empirical models that are used currently.

5.4 CONCLUSIONS

The potential of a spectrophotometric technique for characterization of the concentration polarization layer in DCMD (i.e., thickness and concentration profile) has been demonstrated in this study. To realize the novel technique, a custom membrane cell was fabricated which allowed passage of light perpendicular to the feed flow and parallel to the membrane surface. A spatially resolved visible (wavelength – 670 nm) spectrophotometer with a resolution of 4.5 μm was constructed with a laser as the light source and a linear CCD camera as the sensor. The workability of this technique was demonstrated by testing with nickel chloride solutions up to 55 g/l; the concentration gradient near the membrane surface was clearly visible for the results presented in this study. The experimental system developed in this study was limited to concentrations below 100 g/L of salt concentration in the feed due to the high absorbance at high salt concentrations. The applicability of this novel technique to evaluate concentration polarization in membrane distillation was validated by using statistical analysis. The results from statistical analysis indicated that feed temperature and flow rate had a negligible effect on the absorbance measurements by the optical setup and that the method described in this work can measure the concentration polarization coefficient and boundary layer thickness irrespective of temperature and flow rate. Future work

will be aimed at using the spectrophotometric technique to evaluate the effect of feed temperature, hydrodynamic conditions and salt concentration on the extent of concentration polarization.

6.0 CONCENTRATION POLARIZATION IN DIRECT CONTACT MEMBRANE DISTILLATION: QUANTITATIVE ANALYSIS AND COMPARISON WITH CONVENTIONAL APPROACH OF ESTIMATION

Concentration polarization occurs in almost all membrane based separation processes. In this study the concentration profile of dissolved salt has been accurately characterized using a laser based spectrophotometric method. The spectrophotometric method developed previously is a non-intrusive method customized for a direct contact membrane distillation system, wherein the feed solution contained a transition metal salt. The amount of light absorbed by the salt at a particular wavelength was correlated to the salt concentration that was measured along the distance from the membrane surface using a linear CCD camera. This spectroscopic method can probe the solute concentration profile near the membrane surface with a spatial resolution of 4.5 μm. The objective of the current work was to probe the concentration profile of solute and analyze the impact of operating parameters, such as feed concentration, hydrodynamic conditions and feed temperature, on the solute concentration profile in the boundary layer. This study also examined the validity of the conventional approach where semi-empirical models are used to estimate the boundary layer thickness (BLT) and concentration polarization coefficient (CPC) against experimental results. Nusselt correlations were developed specifically for the membrane cell and validated through experimental observations at the operating conditions used in this study. A key finding of this study is that the conventional approach of estimating the effect of concentration polarization

severely under predicts the BLT and CPC. The results of this study highlight the need to develop new methods to estimate the BLT and CPC as the conventional approach of using the parameters of Nusselt correlation for the Sherwood correlation does not agree with experimental observations obtained for a membrane distillation system.

6.1 INTRODUCTION

Membrane distillation (MD) is an evaporative process that uses microporous hydrophobic membranes for the recovery of high purity permeate. While there are several configurations in which MD can be operated [189], direct contact membrane distillation (DCMD) is regarded as the simplest one. In DCMD, the hydrophobic membrane is in direct contact with a saline feed stream on one side and a pure permeate stream on the other. The feed stream is at a much higher temperature than the permeate stream and this temperature difference creates a vapor pressure difference across the hydrophobic membrane, which is the driving force for MD operation. Because the membrane is hydrophobic, the liquid phase saline feed remains in the feed side while water vapor can traverse across the membrane to the permeate-side. As only vapors are transported across the membranes, MD exhibits almost complete rejection of salts and other non-volatile compounds as long as the membrane retains its hydrophobicity. Although DCMD is predominantly studied for desalination of sea water [35, 42, 48], it has also been studied for concentration of fruit juice [49-51], recovery of acid [52], separation of heavy metals from water [46], removal of radioactive contaminants from wastewater [47] and recovery of fresh water from high salinity produced water [62, 124, 160].

The presence of temperature polarization in an MD process (i.e., the temperature difference between the feed and permeate-side at the membrane surface is much smaller than that in the bulk) can results in a significant flux drop due to a reduction in the driving force (i.e., vapor pressure difference between the feed and permeate-side). This phenomenon has been well studied in MD literature [81, 82, 187, 190, 191]. However, MD experiences another polarization phenomenon known as concentration polarization (CP), where the concentration of the solute is much higher at the feed-membrane interface than that in the feed bulk. CP is exhibited only on the feed side in MD, as the permeate side is virtually devoid of salts. Significant importance has been given to CP in pressure-driven membrane processes such as ultrafiltration and reverse osmosis [175, 177] as the flux decline due to this effect can be severe. However, only a few studies focused on the impact of CP in membrane distillation [81, 94, 165]. It is generally believed that CP does not affect the permeate flux in membrane distillation significantly because the impact of concentration on the feed vapor pressure is considered minimal. However, CP may facilitate salt crystallization at the membrane surface when the feed concentrations are close to the saturation limit of the dissolved salts [79]. The importance of accurately characterizing CP in MD has been emphasized recently [109] to improve understanding of MD systems and facilitate accurate prediction of their performance.

In a previous section (Section 5), a non-intrusive laser-based spectrophotometric technique was developed to measure the concentration profile of salt near the membrane surface in a DCMD cell. This method was able to accurately characterize the concentration of solute near the membrane surface and was unaffected by temperature polarization and other operating parameters (i.e. flow rate, temperature, etc.). Nickel chloride ($NiCl_2$) was used as a solute for the development of this technique due to its ability to absorb light in the visible range and also because the light

absorbance by $NiCl_2$ exhibited an almost perfect linear correlation with a wide range of concentrations. The current study is aimed at probing the concentration profile near the membrane surface to directly evaluate the effect of feed concentration, flow rate and temperature on CP. The CP effect is generally estimated using semi-empirical heat transfer (i.e., Nusselt correlation) and mass transfer (i.e., Sherwood correlation) models without actually measuring the solute concentration profile. Because of the high spatial resolution of the method developed previously, it is now possible to investigate the validity of these models for estimating the CP effect. A Nusselt correlation was developed specifically for the membrane cell used in the DCMD setup. The Nusselt correlation was validated by comparing the permeate flux estimated by the model with that obtained from pure water DCMD tests at different operating conditions. Furthermore, the experimentally observed concentration profiles of solute near the membrane surface was compared to that predicted by the model and the effect of operating conditions on CP was assessed in this study.

6.2 THEORY AND METHODOLOGY

6.2.1 Experimental Setup

The details of the counter current DCMD system with the optical setup and the experimental protocol for measurement of concentration profile have been discussed previously (Section 5). While the permeate channel of the membrane cell contained a spacer, feed channel was empty to facilitate passage of light across the channel. The extent of CP effect was studied in this work for nickel chloride ($NiCl_2$) solutions with concentrations ranging from 5.4 to 54.5 g/l. Additionally,

the effect of feed temperature and flow rate on concentration profile was also studied in the temperature range of 40 to 60 ^{o}C and feed flow rate of 0.2 to 0.6 LPM (the corresponding range of feed velocity is 0.028 to 0.083 m/s).

6.2.2 Developing a Nusselt correlation for the membrane cell:

The importance of precisely characterizing convective heat transfer in membrane distillation has been addressed in several studies [94, 192]. Phattaranawik et al. proposed replacing the membrane in a MD cell with an impermeable membrane to determine the appropriate heat transfer correlation for the MD cell [77]. In their method, the experimental 'overall heat transfer coefficient' (U_{exp}), which is calculated from energy balance across the MD cell, is compared to the 'overall heat transfer coefficient' estimated using different Nusselt correlations (U_{corr}) obtained from the literature. The Nusselt correlation that resulted in U_{corr} values closest to the U_{exp} values is chosen as the best correlation that can be used to describe the convective heat transfer. However, as mentioned by Leitch et al. [192], this method may not be applicable for a wide range of experimental conditions because it assumes that a previously established Nusselt correlation can satisfactorily describe the heat transfer in the membrane cell. In this study, the idea of using an impermeable membrane was applied to develop the Nusselt correlations that can adequately estimate the heat transfer coefficient for the membrane cell. However, unlike the original Phattaranawik's method, two Nusselt correlations had to be developed because the geometry of the feed (without spacer) and permeate (with spacer) channels in the MD cell used in this study were different. To develop a Nusselt correlation for the feed side, the spacer from the permeate channel was removed and the height of the permeate channel was adjusted to 5 mm (i.e., equal to the feed channel) by removing the shims. A 127 μm thick impermeable PTFE membrane (thermal

conductivity = 0.25 W/m/K [159]) was inserted in the membrane cell and DI water was used as feed. A total of 16 tests at three different feed temperatures (i.e., 60, 50 and 40 ^{o}C) and fixed permeate temperature of 20 ^{o}C with identical Reynolds numbers in feed and permeate channels ranging from 200 to 1400 were performed in duplicate. Identical tests were repeated to develop a Nusselt correlation for the permeate channel where spacers were inserted in both the feed and permeate channels and the height of both channels was adjusted to 1 mm using shims. The following procedure was used to obtain the Nusselt correlation for this study:

a. The physical properties of the feed and permeate-side streams were calculated at the average (i.e., average of inlet and exit streams) bulk temperature [193].
b. The overall heat transfer coefficient was calculated using the experimental data by first calculating the rate of heat transfer (Q, Watts):

$$Q = \dot{m}_f \cdot C_p \cdot \left(T_{f,i} - T_{f,o}\right) = \dot{m}_p \cdot C_p \cdot \left(T_{p,o} - T_{p,i}\right) \tag{6.1}$$

The overall heat transfer coefficient (U, W/m^2/K) is calculated as:

$$U = \frac{Q}{A \cdot \left[\frac{\left(T_{f,i} - T_{p,o}\right) - \left(T_{f,o} - T_{p,i}\right)}{ln\left(T_{f,i} - T_{p,o}\right) - ln\left(T_{f,o} - T_{p,i}\right)}\right]} \tag{6.2}$$

where, $\dot{m}_f$ and $\dot{m}_p$ are the feed and permeate-side flow rates (kg/s), C_p is the specific heat of water (i.e., 4180 J/kg/K), $T_{f,i}$ and $T_{f,o}$ are the feed inlet and exit temperatures (K), respectively, $T_{p,o}$ and $T_{p,i}$ are the permeate inlet an exit temperatures (K), respectively and A is the membrane area (m^2).

c. The feed and permeate heat transfer coefficients were obtained from the following equation:

$$\frac{1}{U} = \frac{1}{h_f} + \frac{1}{k'/_{\delta'}} + \frac{1}{h_p} \tag{6.3}$$

where, h_f and h_p are feed and permeate-side heat transfer coefficients (W/m^2/K), k' is the thermal conductivity of the impermeable PTFE membrane (W/m/K) and δ' is the thickness of the impermeable PTFE membrane (m). Since both the feed and permeate sides had identical geometries and Reynolds number, the heat transfer coefficients were assumed to be equal on both sides.

d. The Nusselt number (Nu) was calculated as follows:

$$Nu = \frac{h \cdot d_h}{k_f} \tag{6.4}$$

where, h is the heat transfer coefficient (W/m^2/K) for either the feed (h_f) or permeate side (h_p), d_h is the hydraulic diameter of the channel (m), k_f is the thermal conductivity of the fluid (W/m/K).

e. Reynolds number (Re) and Prandtl number (Pr) were calculated as follows:

$$Re = \frac{d_h \cdot v \cdot \rho}{\mu} \qquad \text{Pr} = \frac{C_p \cdot \mu}{k_f}$$

where, v is the fluid velocity (m/s), ρ is the fluid density (kg/m^3), μ is the fluid viscosity (Pa·s).

f. The following form of Nusselt correlation was used in this study:

$$Nu = A \cdot Re^b \cdot Pr^c \tag{6.5}$$

The Nusselt correlation was developed by plotting log(Nu/Pr^c) versus log(Re^b) to obtain the values of A, b and c. In their study with hollow fiber DCMD, Bui et al. [99] varied the exponent 'c' between 0.30 and 1. The authors reported that a higher value of 'c' improves the linearity of the plot shown in Figure 6.1, but worsens the ability of the model to predict mass transfer in DCMD. The exponent value of 0.33 for Prandtl number has been used extensively for Nusselt correlations in the literature [77, 192, 194-196] and was used in this study.

Figure 6.1 shows the result of regression analysis to obtain the coefficient 'A' and the exponent 'b' for the Nusselt correlations for feed and permeate sides of the MD cell. As seen in the figure, a correlation coefficient of 0.899 and 0.936 were obtained for the linear plots for 5 mm channels without spacers and 1 mm channels with spacers, respectively. The constant and exponents obtained for the Nusselt correlation are listed in Table 6.1.

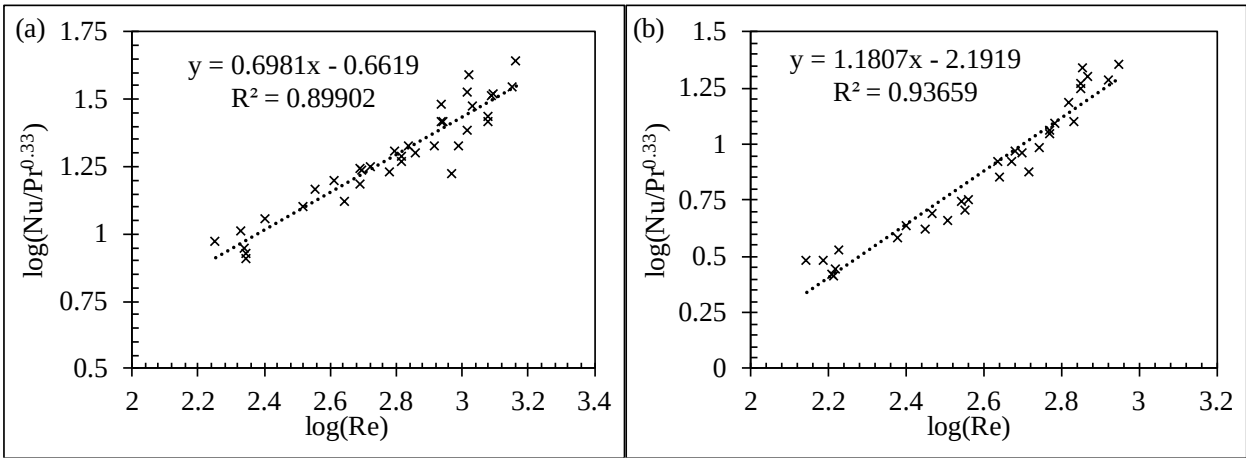

Figure 6.1. Plots of $\log(Nu/Pr^{0.33})$ vs log(Re) for membrane cell when (a) feed and permeate channels were empty and the channel height was 5 mm and (b) feed and permeate channels contained spacers and the channel height was 1 mm.

Table 6.1. Values of constants for the semi-empirical Nusselt correlation (Eqn. 5).

Channel height	**A**	**b**	**c**	**R^2**
5 mm, without spacer	0.2178	0.6981	0.33	0.899
1 mm, with spacer	0.0064	1.1807	0.33	0.936

6.2.3 Model validation:

Pure water DCMD tests were carried out using a hydrophobic PTFE membrane with a pore size of 0.2 μm to validate the Nusselt correlations obtained for the membrane cell. The properties of the PTFE membrane are listed in Appendix A4. The permeate channel was adjusted to a channel height of 1mm and the spacer was added while the feed channel was used without a spacer with a channel height of 5 mm. A model developed in previous study [160] was used to validate the Nusselt correlation. The procedure for estimating the permeate flux using this model is discussed in SI. For model validation, DCMD tests were carried out with pure water as feed while varying the feed temperature and feed and permeate flow rates. The details of the experimental conditions used for model validation are listed in Table A7 in the Appendix A4. Figure 6.2 compares the permeate flux obtained from the model with that obtained experimentally. As seen in this figure, the model prediction matches the experimentally observed permeate flux with a root mean square error of 7%. The model based on the Nu correlation with coefficients listed in Table 6.1 was therefore used for future calculations without any additional calibration.

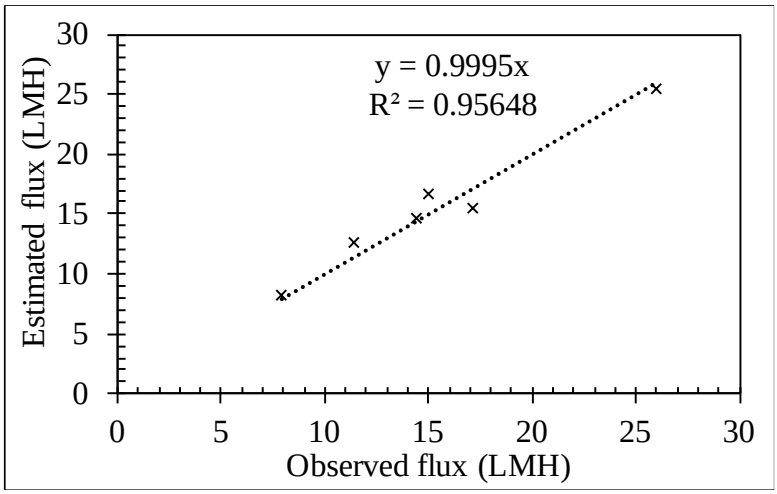

Figure 6.2. Comparison of model prediction with experimentally observed flux.

6.2.4 Boundary layer thickness and concentration polarization coefficient

The effect of CP is generally represented by the concentration polarization coefficient (CPC), which is the ratio of concentration of solute at the feed-membrane interface ($C_{m,f}$) to the concentration of solute in the bulk feed stream ($C_{b,f}$) [81, 97, 190].

$$CPC = \frac{C_{m,f}}{C_{b,f}} \tag{6.6}$$

The concentration at the feed-membrane interface can be obtained using the film theory and Sherwood correlation [190, 197]. Mass transfer across a membrane can be calculated from a material balance according to [198]:

$$J_s = D\left(\frac{dC}{dx}\right) + \frac{JC}{\rho} \tag{6.7}$$

where, J_s is the solute flux across the membrane (m/s), D is the solute diffusion coefficient (m^2/s), C is the solute concentration (g/l), x is the distance measured from the membrane surface (m), J is the solvent flux through the membrane ($kg/m^2/s$), ρ is the density of the fluid (kg/m^3). Due to the very high salt rejection in MD, the solute flux (J_s) across the membrane is negligible (i.e., zero). Equation 6.7 can be used to obtain the concentration profile of solute within the boundary layer. The following boundary conditions apply:

$$C\ [x = 0] = C_{m,f} \tag{6.8}$$

$$C\ [x = \delta] = C_{b,f} \tag{6.9}$$

where, δ is the boundary layer thickness (BLT) (m).

Integrating Equation 6.7 and using the boundary layer conditions (i.e., Equations 6.8 and 6.9) yields:

$$C_{m,f} = C_{b,f} \cdot exp\left(\frac{J\delta}{D\rho}\right) \tag{6.10}$$

The boundary layer thickness (δ) is unknown and can be estimated from the film-diffusion mass transfer coefficient, K ($K = D/\delta$) that can be obtained from Sherwood correlation which is derived from the mass transfer and heat transfer (Nusselt correlation) analogy [81, 97, 198].

$$Sh = A \cdot Re^{b} \cdot Sc^{c} \tag{6.11}$$

The values of constants A, b and c are listed in Table 6.1. Sherwood number (Sh) and Schmidt number (Sc) were calculated as follows:

$$Sh = \frac{K d_h}{D} \qquad Sc = \frac{\mu}{\rho D}$$

6.3 RESULTS AND DISCUSSION

As mentioned above, $NiCl_2$ was used as the solute to study the CP phenomenon in a DCMD cell. Figure 6.3 shows the variation in the concentration of $NiCl_2$ near the membrane surface as measured by the optical system described previously (Section 5). This figure also shows the concentration profile predicted by the model discussed above. It should be noted that the physical-chemical properties of $NiCl_2$ solutions at varying temperature and concentration (i.e., viscosity, density, specific heat, thermal conductivity) were obtained from the literature [199-202] and were incorporated in the model. Because $NiCl_2$ diffusion coefficient as a function of concentration and temperature is not readily available in the literature and because the diffusion coefficient does not vary significantly with concentration, a constant value of 1.05 x 10^{-9} m^2/s [199, 203] was used in these calculations. The same approach of using a single value of the diffusion coefficient was previously used in modelling a reverse osmosis system [204]. Experimental conditions in Figure 6.3 and in subsequent figures do not include information about the Reynolds number in feed and

permeate channels but include information about the flow rate (LPM) and fluid velocity (m/s). Such approach is adopted because the flow rate and fluid velocity remain constant irrespective of the feed concentration while the Reynolds number changes significantly due to changes in the viscosity and density of the fluid with solute concentration. However, the Reynolds number has been mentioned when discussing the results obtained at specific concentrations of feed.

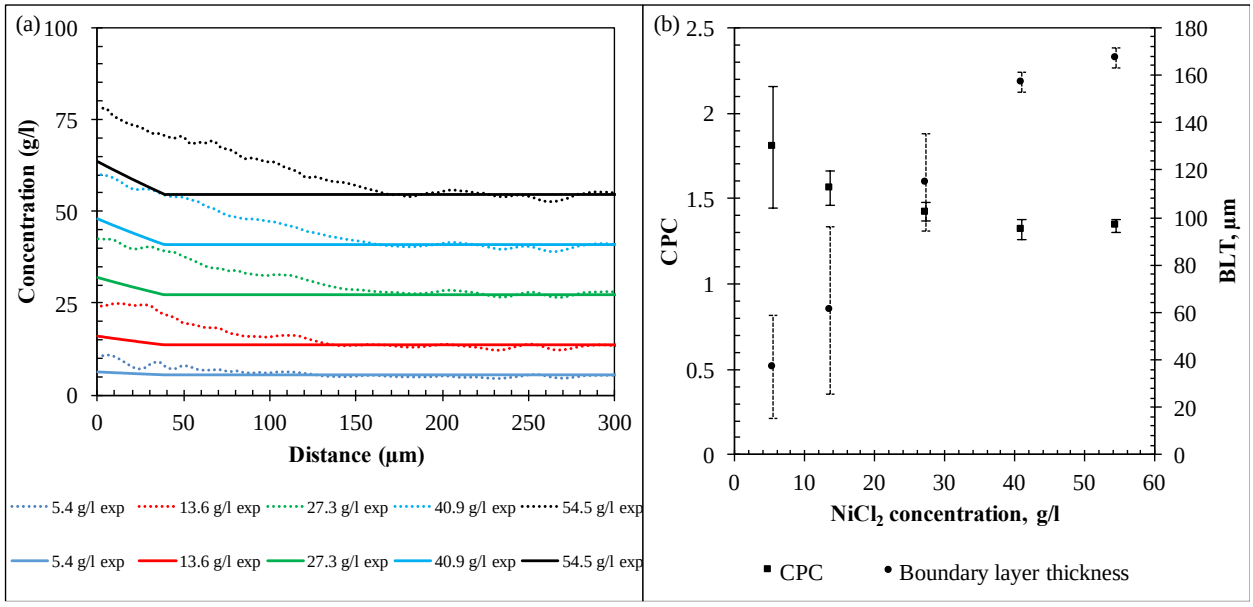

Figure 6.3. (a) Variation of $NiCl_2$ concentration near the membrane surface at a feed flow rate of 0.5 LPM (i.e., v = 0.07 m/s), permeate-side flow rate of 0.2 LPM (i.e., v = 0.22 m/s), feed temperature of 50 ^oC and permeate temperature of 20 ^oC. Bold lines denoted as 'theo' represent the concentration profile predicted by the mathematical model while the dotted lines represent the concentration profile measured using the optical setup. (b) Experimentally observed variation in CPC and BLT as a function of $NiCl_2$ concentration in the feed.

As seen in Figure 6.3, the concentration of solute is significantly higher at the feed-membrane interface and the BLT increases substantially with increasing solute concentration. The theoretical model predicts minimal increase in the BLT at higher concentrations (i.e., BLT increased from 37.8 to 38.9 μm when the feed concentration increased from 5.4 to 54.5 g/L), which is not even discernable in Figure 6.3(a). Although the theoretical model (Equation (6.10) predicts

an exponential increase in the concentration profile within the boundary layer [190, 197], the relationship shown in Figure 6.3(a) appears to be linear, which can be attributed to a very low permeate flux in the DCMD cell (i.e., higher value of permeate flux (J) in Eqn. 6.10 would result in a larger exponent and a typical exponential increase in solute concentration in the boundary layer). While the experimental data and model predictions follow a similar trend of concentration profile and BLT with changing feed concentration, the extent to which CP occurs is significantly under-predicted by the model. For example, the experimentally obtained $C_{m,f}$ for a feed concentration of 54.5 g/l in Figure 3(a) is 78 g/l, whereas the value predicted by the model is 63 g/l. This 19 % difference in the $C_{m,f}$ estimate using the theoretical model is unexpectedly large considering that the Nusselt correlation (and Sherwood correlation) that was developed for the same membrane cell and operating conditions used in this study was used in the model. Figure 6.3(b) shows experimentally measured CPC and BLT under the experimental conditions denoted in Figure 6.3 (a) at different solute concentrations. The error bars shown in Figure 6.3(b) represent the standard deviation for three replicates. As seen from this figure, the CPC is very high at low solute concentrations and decreases with an increase in the solute feed concentration. The BLT increases significantly at higher solute concentrations in the feed, whereas the theoretical model predicts almost no change in the BLT (i.e., increase from 37.8 to 38.9 μm). It is important to note that the standard deviation of both CPC and BLT measured from three replicates are higher at low solute concentration and decreases at higher concentrations. While the reliability of results obtained using the optical system developed in this study improves at higher solute concentrations (i.e. $\geq$ 20 g/l), increasing the feed concentration beyond 100 g/l results in a significant increase in the signal to noise ratio and reduces measurement accuracy (Se). The feed solute concentration

was therefore limited to 54.5 g/l to accurately characterize the concentration profile as the $C_{m,f}$ was measured in excess of 80 g/l when the feed concentration was 54.5 g/l.

Experimentally observed permeate flux as a function of $NiCl_2$ concentration and feed temperature is shown in Figure 6.4. Feed temperature has a significant influence on permeate flux while the feed concentration has a minor impact. For instance, increasing the feed temperature from 40 to 50 ^oC at the feed concentration of 27 g/l increased the permeate flux from 8.1 to 16.6 LMH (i.e., 105% increase). However, increasing the feed concentration from 0 to 54.5 g/l at the feed temperature of 50 ^oC decreased the permeate flux from 17.9 to 15.9 LMH (i.e., 7% decrease). Increasing the feed temperature has a much more pronounced impact on feed vapor pressure increase than vapor pressure depression caused by an increase in the feed solute concentration. Figure 6.5 shows the impact of temperature on CPC and BLT at different concentrations of $NiCl_2$ in the feed. As can be seen in this figure, experimentally determined CPC and BLT exhibited exponential changes with solute concentration and flattened as feed concentration approached the highest levels evaluated in this study. However, the theoretical model (Equations (6.10) and (6.11)) shows minimal dependence of CPC and BLT on the feed solute concentration. At a feed temperature of 50 ^oC, the theoretical model predicted a 2.5% decrease in CPC (i.e., from 1.19 to 1.16) when the feed concentration increased from 5.4 to 54.5 g/l (i.e., 10-fold increase). However, experimentally determined CPC decreased by 25% (i.e., from 1.80 to 1.34) for the same increase in the feed concentration. Similar discrepancy between experimentally determined BLT and that calculated using a theoretical model is shown in Figure 6.5(b).

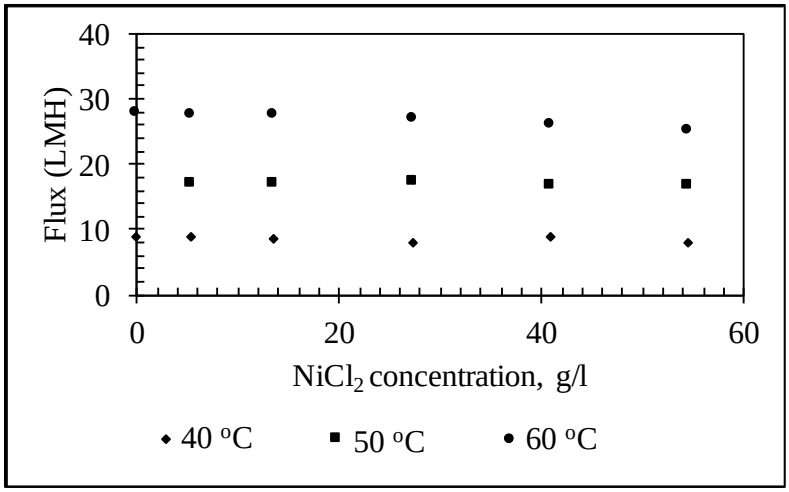

Figure 6.4. Permeate flux as a function of $NiCl_2$ concentrations in the feed at feed temperatures of 40, 50 and °C. The permeate temperature was maintained at 20 °C, while the feed and permeate flow rates were 0.5 LPM (i.e, v = 0.07 m/s) and 0.2 LPM (i.e., v = 0.22 m/s) respectively.

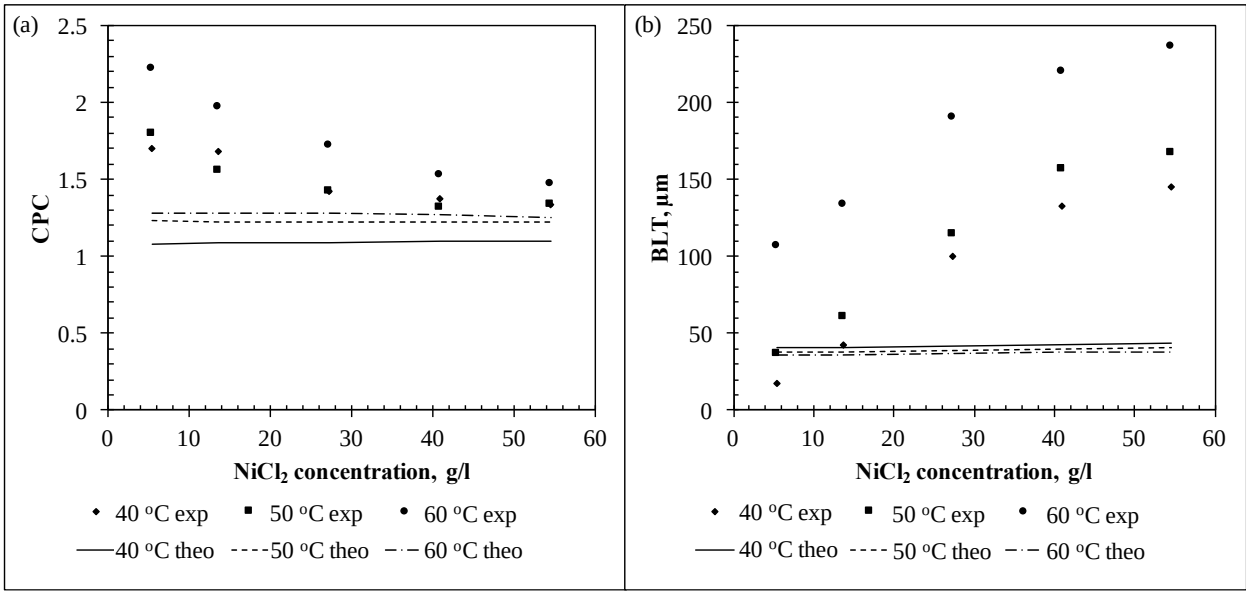

Figure 6.5. Variation of (a) CPC and (b) BLT with $NiCl_2$ concentration at a feed temperature of 40, 50 and 60 °C. Lines represent model prediction. Permeate temperature was maintained at 20 °C, while the feed and permeate flow rates were 0.5 LPM (i.e, v = 0.07 m/s) and 0.2 LPM (i.e., v = 0.22 m/s), respectively.

As seen in Figure 6.5, the change in feed temperature from 40 to 50 °C had much lower impact on CPC and BLT when compared to the impact observed when the feed temperature

increased from 50 to 60 ^{o}C. At a feed concentration of 27 g/l for example, experimentally determined CPC changed very little when the feed temperature increased from 40 to 50 ^{o}C while it increased by 21% (i.e., from 1.42 to 1.73) when the feed temperature increased from 50 to 60 ^{o}C. Similarly, the BLT increased by 15% (i.e., from 100 to 115 μm) when the feed temperature increased from 40 to 50 ^{o}C while it increased by 65% (i.e., from 115 to 190 μm) when the feed temperature increased from 50 to 60 ^{o}C. This pronounced impact of temperature on CPC and BLT at higher temperatures can be attributed to exponential dependence of permeate flux on feed temperature due to exponential dependence of water vapor pressure on temperature. Such behavior is also true for the permeate flux showed in Figure 6.4; permeate flux in the case of DI water (i.e., feed concentration of 0 g/l) increased by 8 LMH when the feed temperature increased from 40 to 50 ^{o}C while it increased by 10.7 LMH when the feed temperature increased from 50 to 60 ^{o}C. The increase in permeate flux with an increase in feed temperature results in higher CPC and thicker boundary layer because more solute is transported towards the membrane where it is completely rejected and hence, more solute has to diffuse back to the bulk solution.

The effect of feed flow rate on permeate flux at different $NiCl_2$ concentrations in the feed is depicted in Figure 6.6. As the feed flow rate increased from 0.2 to 0.4 LPM, a slight increase in the permeate flux is observed. However, further increase in the feed flow rate has negligible impact on permeate flux. Such an asymptotic trend of flux with increasing feed flow rate has been observed previously and is attributed to the reducing polarization effects at higher feed flow rates [95, 119]. In addition, the effect of feed flow rate on flux is significantly lower when compared to the effect of feed temperature as increasing feed temperature directly affects the driving force whereas increasing feed flow rate just improves the efficiency of mass transfer by reducing the polarization effects [160, 205]. Figure 6.7 shows the influence of feed flow rate on the CPC and

BLT at different $NiCl_2$ concentrations in the feed stream when all the other parameters (i.e., feed and permeate-side temperatures, permeate-side flow rate) were maintained the same between the tests. As can be seen in Figure 6.7(a) the CPC decreases with increasing feed solute concentration, which is similar to the results discussed in Figure 6.5(a). The CPC also decreases with increasing feed flow rate. At a feed concentration of 54.5 g/l, experimentally determined CPC decreased by 9% (i.e., 1.43 to 1.3) when the feed flow rate increased from 0.2 LPM (i.e., v = 0.028 m/s, Re = 390) to 0.4 LPM (i.e., v = 0.056 m/s, Re = 780) while there was almost no effect when the feed flow rate was increased from 0.4 LPM to 0.6 LPM (i.e., at 0.6 LPM, v = 0.083 m/s and Re = 1150). In the same way, the BLT decreased by 26% (i.e., from 215 to 160 μm) when the feed flow rate was increased from 0.2 to 0.4 LPM, while it only decreased by 15% (i.e., from 160 to 135 μm) when the feed flow rate was increased from 0.4 to 0.6 LPM. The effect of feed flow rate on CPC and BLT is more pronounced when feed flow rate is increased from 0.2 to 0.4 LPM while little change in CPC and BLT is observed when the feed flow rate is increased from 0.4 to 0.6 LPM. This trend is similar to that observed in Figure 6.6 where the increase in feed flow rate from 0.2 to 0.4 LPM affects permeate flux, but further increase in flow rate has little or no effect. As the feed flow rate increases, the higher Reynolds number leads to a much lesser boundary layer thickness as evident from Figure 6.7(b) which in turn results in a lower CPC. Increasing the feed flow rate leads to a slightly lesser BLT due to higher Reynolds number, whereas the higher permeate flux due to increased feed flow would mean that the BLT would be thicker. Hence, this effect may oppose the effect of Reynolds number on the boundary layer thickness as more solute has to diffuse back to the bulk and eventually, there would be a value of flow rate after which increasing the flow would has no effect on BLT. In all cases, theoretical model under predicts the extent of CP at the feed-membrane interface. As shown in Figure 6.7, a significant discrepancy is observed between

the CPC and BLT predicted by the model and that observed in the optical experiments. For example, at a feed concentration of 27 g/l, the model underestimates CPC by 23% and BLT by 64% when the feed flow rate is 0.2 LPM (i.e., v = 0.028 m/s, Re = 400). The CPC and BLT values vary drastically with feed concentration as well as with feed flow rate. However, the model predicts little or no change in CPC and BLT values as a function of feed concentration and feed flow rate. While the trends of experimentally measured CPC and BLT with varying feed concentration, temperature and flow rate in Figure 6.7 and Figure 6.5 are similar to that estimated by the model, the extent of CP is severely under-predicted for all experimental conditions evaluated in this study.

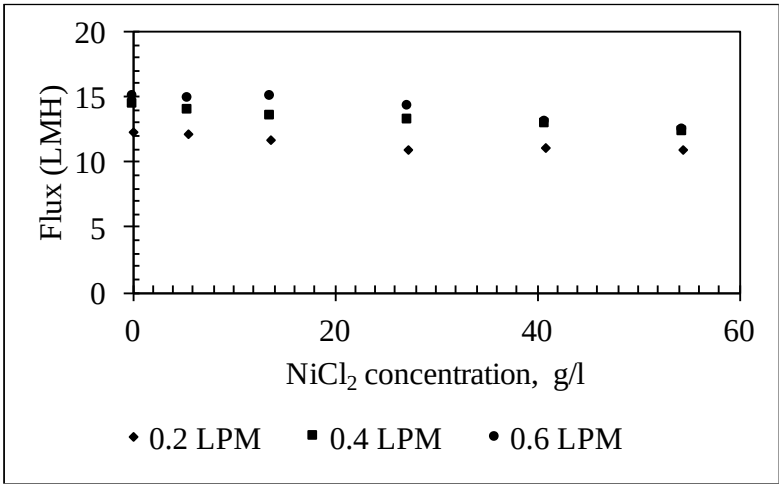

Figure 6.6. Permeate flux as a function of $NiCl_2$ concentrations at feed flow rates of 0.2, 0.4 and 0.6 LPM (v = 0.028, 0.056 and 0.083 m/s, respectively). The feed and permeate-side temperatures were maintained at 50 and 20 ^{o}C respectively, while the permeate-side flow rate was 0.1 LPM (v = 0.11 m/s).

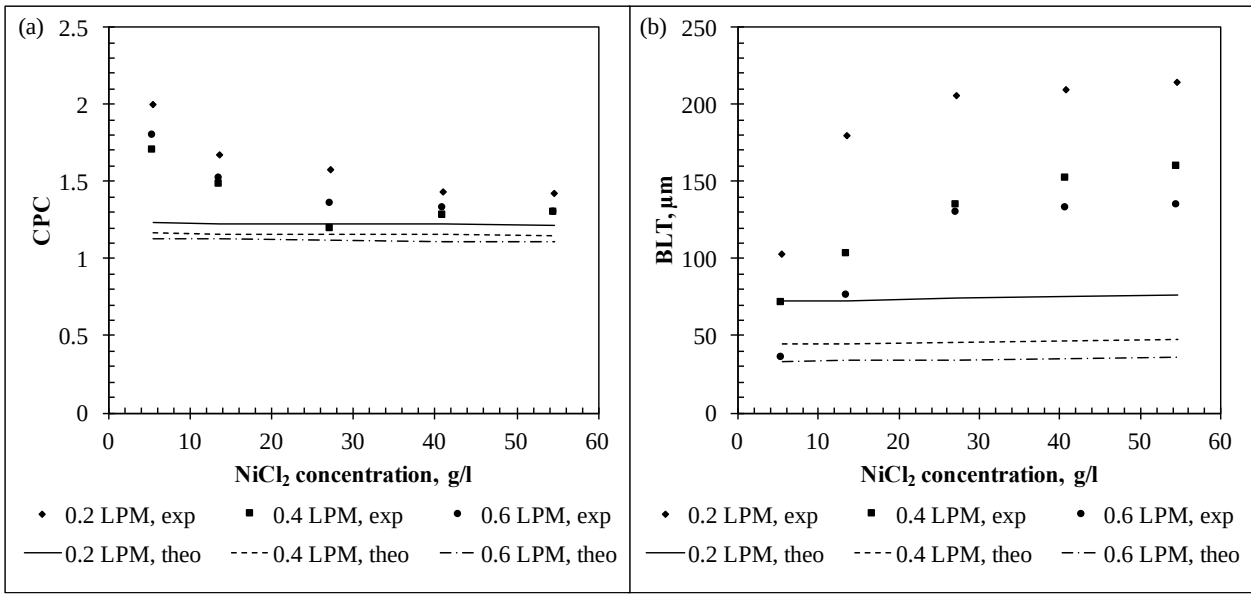

Figure 6.7. Variation of (a) CPC and (b) BLT with $NiCl_2$ concentration at feed flow rates of 0.2 LPM, 0.4 LPM and 0.6 LPM (v = 0.028, 0.056 and 0.083 m/s respectively). Lines represent model prediction. Feed and permeate temperatures were 50 and 20 ^oC respectively, while the permeate flow rate was 0.1 LPM (v = 0.11 m/s).

A slight increase in the solute concentration at the membrane surface should not have a major impact on the permeate flux because the mass transfer in MD is driven by the vapor pressure across the hydrophobic membrane. Several previous studies suggested that the effect of CP is negligible in an MD system [81, 94, 165]. Martínez-Díez et al. [81] studied the effect of temperature and concentration polarization in DCMD with sodium chloride concentrations up to 1.67 moles/l (i.e., about 98 g/l). The authors reported that the salt concentration at the membrane surface can be up to 4% higher compared to the bulk concentration. According to their calculations, this 4% higher concentration would result in just 0.2 % decrease in the driving force. In the current work, nickel chloride exhibited up to 47% higher $C_{m,f}$ when compared to $C_{b,f}$ (i.e. CPC = 1.47) at the highest concentration studied (i.e. 54.5 g/l) which is significantly higher than that reported by Martínez-Díez et al. for sodium chloride. This is likely due to the higher diffusivity of sodium

chloride in water when compared to nickel chloride. Nickel chloride has a diffusivity of 1.05 x 10^{-9} m^2/s [199, 203] while that of sodium chloride is about 1.5 x 10^{-9} m^2/s [206]. Therefore, sodium chloride diffuses about 45% faster than nickel chloride in water which results in a much faster diffusion of salt towards the bulk feed stream and hence a lower CPC is observed. The influence of high salt concentration on the mass transfer coefficient and permeate flux was analyzed by Yun et al [79]. The authors reported that the solute accumulated near the membrane surface in DCMD. The results from their study indicated that the salt concentration at the membrane surface reached saturation even when the bulk feed concentration was under the saturation limit. A previous study on DCMD with high salinity produced water also reported up to 30% higher concentration of solute at the membrane surface when compared to bulk concentration which resulted in a 10 % flux drop due to concentration polarization when the feed TDS was 270,000 mg/l [124]. CP becomes an important issue with regards to membrane fouling as well as flux decline when high salinity water is treated by using MD. Other applications of MD such as concentration of fruit juices can exhibit severe flux decline at high concentrations due to CP which arises as a result of high viscosity of the feed [207]. In such cases, it is important to accurately characterize CP to be able to account for flux decline as well as prevent membrane fouling and solute crystallization. As demonstrated in this study the current approach of using the parameters of heat transfer correlation (i.e. A, b and c from Nusselt correlation, Equation 6.5) to describe the mass transfer through the Sherwood correlation severely underestimates the effect of CP. An improved method of characterizing CPC and BLT is therefore required in order to accurately estimate these parameters.

6.4 CONCLUSIONS

The concentration polarization phenomenon, which occurs in all membrane based separation processes, was evaluated in detail in this study focused on DCMD system using a novel experimental approach that allowed accurate measurement of solute concentration within the boundary layer. The experimental work was combined with theoretical model to understand the effect of feed concentration, hydrodynamic conditions and feed temperature on the extent of concentration polarization and the thickness of the boundary layer. It was found that increasing the feed temperature significantly increases the CPC and BLT, which is predominantly due to the increase in permeate flux at higher feed temperatures. A 20 ^{o}C increase in the feed temperature (i.e., from 40 to 60 ^{o}C) can lead to a 10 to 30% increase in the CPC and a 60 to 490% increase in the BLT when the feed concentration changes from 5.4 to 54.5 g/l respectively. The permeate flux increase leads to enhanced solute transport towards the membrane surface. Because the solute is completely rejected by the hydrophobic membrane, greater mass of solute has to diffuse back to the bulk solution, which results in higher solute concentration at the feed-membrane interface and a thicker boundary layer. Both CPC and BLT decrease with an increase in the feed flow rate (or feed velocity) that enhances mixing in the feed channel. A 0.4 LPM increase in feed flow rate (i.e, Re increase by about 200%) can lead to a 10 to 7% decrease in the CPC and a 65 to 37% decrease in the BLT when the feed concentration changes from 5.4 to 54.5 g/l respectively. On the other hand, increasing the solute concentration in the feed increases the solute concentration at the membrane surface and BLT due to greater mass of solute molecules in the feed stream. Overall, the feed temperature had the largest impact on concentration polarization followed by the feed flow rate and solute concentration. This finding should be considered when there is a possibility

of salt crystallization on the membrane surface (i.e., when the solute concentration if near the saturation limit).

A Nusselt correlation was developed specifically for the DCMD module used in this study to investigate the validity of the conventional approach for estimating the CP effect that is based on the similarity of heat and mass transfer phenomena. The Nusselt correlation was validated by comparing the permeate flux estimated by the model with that obtained from DCMD tests with pure water conducted at different feed temperatures and flow rates. The parameters of the Nusselt correlation were then used for the Sherwood correlation to obtain the mass transfer coefficient and evaluate the BLT and CPC. In all the cases evaluated in this study (i.e., varying feed temperature, flow rate and solute concentration), general trends of the CPC and BLT calculated using the conventional modeling approach were similar with experimentally determined values. However, in all instances, the CPC and BLT were severely under predicted by the conventional approach. This drastic discrepancy in the model predictions and experimental observations prove that the conventional approach of using the correlation parameters from Nusselt heat transfer correlation for Sherwood mass transfer correlation is not a sound approach of estimating the extent of concentration polarization in DCMD system operated at high solute concentrations. Hence, a novel approach is required to understand the effect of concentration polarization and to estimate the CPC and BLT in these membrane systems.

7.0 SUMMARY AND CONCLUSIONS

The overall goal of this work was to evaluate the feasibility of membrane distillation for desalination of high salinity brines with a focus on understanding the fundamentals of mass transfer in the process. The work described here was divided in to five parts: (1) Evaluate the performance of commercially available hydrophobic microfiltration membranes in a direct contact membrane distillation system for treating very high salinity (i.e., up to 300,000 mg/L total dissolved solids) produced water. This part also focused on studying the effect of membrane fouling when treating real produced water brines. (2) Assess the potential of direct contact membrane distillation for treatment of produced water generated during extraction of natural gas from unconventional (shale) reservoir by using waste heat from natural gas compressor stations as the source of thermal energy. (3) Emphasize the importance of recirculation in membrane distillation and demonstrate its impact on the energy consumption of MD. (4) Develop a novel spatially resolved non-intrusive spectrophotometric method developed to measure the concentration profile of solute near the membrane surface in a direct contact membrane distillation system. (5) Probe the concentration profile of solute and analyze the impact of operating parameters, such as feed concentration, hydrodynamic conditions and feed temperature, on the solute concentration profile in the boundary layer; examine the validity of the conventional approach of estimating boundary layer thickness and concentration polarization coefficient.

1. Chapter 2 aims to evaluate the potential of DCMD to treat very high salinity produced water from unconventional onshore natural gas extraction. Several commercially available hydrophobic membranes were screened by using pure water and produced water as feed in DCMD tests to identify those membranes with high permeability suitable for this challenging application. The MD coefficients for the membranes was evaluated using pure water tests and compared as a function of membrane properties. Several membranes with significantly higher MD coefficients than those previously reported in the literature were identified for MD application. PTFE membranes used in this study exhibited substantially higher flux than that reported before for feed waters with a fairly high TDS content. It was found that the properties of the membrane support layer (e.g., thickness and porosity) greatly influence the permeate flux and that highly porous support should be considered when selecting membranes for DCMD.

   All the membranes studied in this work exhibited excellent rejection of ions, including radioactive Ra226 and organic compounds. Temperature polarization was found to have a negligible effect on membrane performance for high salinity feed waters. However, concentration polarization was found to have a major impact on permeate flux at high salinities, which was previously neglected when analyzing MD performance. It was estimated that the concentration of solute during high salinity tests was about 30% higher at the membrane surface when compared to bulk concentration. This study also revealed that iron-based deposits formed on the membrane surface even with relatively low concentrations of iron in the feed. After further investigation, it was realized that iron-based deposits had a negligible impact on membrane performance even after 3 days of operation at an extremely high TDS of 300,000 mg/l. The results obtained in this study indicate that DCMD can prove as a robust technology

for treatment of high salinity wastewaters to produce almost pure water with minimal membrane fouling.

2. The work described in Chapter 3 aims at evaluating the potential of DCMD for treatment of produced water generated during extraction of natural gas from unconventional (shale) reservoirs by using waste heat from the exhaust stream from natural gas compressor station as the energy source to operate DCMD. Using fundamental heat and mass transfer equations and literature correlations, a mathematical model was developed in this study to predict the performance of large scale DCMD systems. The model was incorporated into ASPEN Plus platform and calibrated using the results of laboratory-scale studies. The concept of minimum temperature similar to that employed in the design of heat transfer equipment was employed in this work to obtain the optimum membrane area when several membrane modules are arranged in series. It was found that a minimum temperature difference of 10 ^{o}C between the feed and the permeate-side streams yielded an optimum membrane area for permeate flux across the membrane. Using sensitivity analysis, it was established that the heat recovery efficiency and permeate flux increase with an increase in the DCMD feed temperature, which reduces the specific thermal energy consumption of this treatment process. A plant scale DCMD system with optimum membrane area, external heat recovery, and utilizing waste heat from NG CS was evaluated for its potential to treat produced water in PA region of Marcellus Shale. In this case study, it was found that the amount of energy required to concentrate produced water in PA to 30% salinity was much lower than the amount of waste heat available from NG CS irrespective of the produced water salinity. This study offered evidence of the idea that DCMD can be operated by using waste heat and that NG CS has can be a huge source of untapped waste heat.

3. MD has low single pass water recovery, which necessitates feed recirculation to reach a desired overall water recovery. While feed recirculation increases turbulence in the feed channel to reduce polarization effects and membrane fouling, it also increases the thermal and electrical energy requirements of the system. Chapter 4 emphasizes the importance of recirculation in MD and demonstrates its impact on the energy consumption of MD, which can be an order of magnitude greater when compared with calculations based on a single pass recovery. MD literature lacks reporting of the recycle ratio and its impact on the overall energy consumption of this process. Hence, in this study, a simple approach was used to estimate the single pass water recovery and the recycle ratio in an MD system based on the evaporation efficiency to demonstrate the significance of recirculation on the overall energy consumption of a MD system. The results from this work suggested it is not possible to have a single pass recovery of more than 10%, even with 100% evaporation efficiency in MD and that feed recirculation would be required if higher water recovery is desired. The previously developed ASPEN Plus model which employed fundamental heat and mass transfer equations to simulate DCMD performance was used to evaluate the effect of feed recirculation on the energy demand of this system. This work demonstrates that concentrate recycling accounts for a significant fraction of thermal and electrical energy in MD system. For example, the required recycle ratio increases from 3 to 22 and the corresponding thermal energy requirements increases from 39 to 256 kWh/m^3 of feed when the water recovery is raised from 10 to 50% for a feed solution containing 100 g/L of sodium chloride. This change in the water recovery also corresponds to an increase in the electrical energy consumption from 0.14 to 1.05 kWh/ m^3 of feed. This work also offers an evidence on the effect of feed salt concentration on the reduction in evaporation efficiency and single pass water recovery, which increases the recycle ratio required for a given

overall water recovery. A 10% water recovery using MD when the feed contains 100 g/L of dissolved salts has significantly lower energy requirements (58 kWh/m^3 of feed and a recycle ratio of 4) than that when the feed contains 250 g/L of dissolved salts (90 kWh/m^3 of feed and a recycle ratio of 8). It was also found that specific heat capacity of salt solution influenced the system performance as low salt concentration in the feed resulted in greater water evaporation for the same reduction in specific enthalpy or the same reduction in temperature.

4. As discussed in Chapter 2, concentration polarization was found to have a major impact on permeate flux at high salinities of feed with up to 30% higher solute concentration at the membrane surface when compared to bulk. Hence, a novel method was developed for characterization of concentration polarization. Chapter 5 discusses how the novel technique was developed and demonstrates the successful operation of this technique. To realize the novel technique, a custom membrane cell was fabricated which allowed passage of light perpendicular to the feed flow and parallel to the membrane surface. A laser source with a wavelength of 670 nm was used to illuminate the feed channel in the membrane cell, while a linear CCD camera with 2048 pixels arranged in a single row was used to sense the absorption of light across the feed channel. The apparatus exhibited a spatial resolution of 4.5 μm. The workability of this technique was demonstrated by testing with nickel chloride solutions up to 55 g/l. While the optical system developed in this work was limited to concentrations below 100 g/L of salt concentration in the feed due to the high absorbance at high salt concentrations, the concentration gradient near the membrane surface was clearly visible for the results presented in this study. Statistical analysis was carried out to evaluate the influence of different operating conditions, namely temperature and flow rate, on the workability of the optical technique. Statistical analysis demonstrated that feed temperature and flow rate had a

negligible effect on the absorbance measurements by the optical setup and that the method described in this work can measure the concentration polarization coefficient and boundary layer thickness irrespective of temperature and flow rate.

5. Chapter 6 focuses on probing the concentration gradient in DCMD and evaluating the effect of operating parameters such as feed temperature, flow rate and concentration on the concentration polarization effect. The experimental work was combined with theoretical model to understand the effect of feed concentration, hydrodynamic conditions and feed temperature on the extent of concentration polarization and the thickness of the boundary layer. Feed temperature was found to have a profound effect on concentration polarization, which is predominantly due to the increase in permeate flux at higher feed temperatures. A 20 ^{o}C increase in the feed temperature (i.e., from 40 to 60 ^{o}C) lead to a 10 to 30% increase in the (concentration polarization coefficient) CPC and a 60 to 490% increase in the (boundary layer thickness) BLT when the feed concentration changes from 5.4 to 54.5 g/l respectively. Increasing permeate flux due to increase in feed temperature leads to enhanced solute transport towards the membrane surface. As the solute is completely rejected in DCMD, greater mass of solute has to diffuse back to the bulk solution, which results in higher solute concentration at the feed-membrane interface and a thicker boundary layer. Feed flow rate (or feed velocity) lead to a decrease in both CPC and BLT. A 0.4 LPM increase in feed flow rate (i.e, Re increase by about 200%) lead to a 10 to 7% decrease in the CPC and a 65 to 37% decrease in the BLT when the feed concentration changes from 5.4 to 54.5 g/l respectively. In general, feed temperature was found to have the largest effect on concentration polarization followed by the feed flow rate and solute concentration.

Conventional approach of estimating the boundary layer thickness and solute concentration at the membrane surface was used to estimate the CPC and BLT. In this approach, a heat transfer correlation was developed specifically for the membrane cell and the operating conditions used in this work. The results from the experimental characterization of CPC and BLT were compared to the theoretically estimated values. In all the cases evaluated in this study (i.e., varying feed temperature, flow rate and solute concentration), general trends of the CPC and BLT calculated using the conventional modeling approach were similar with experimentally determined values. However, in all instances, the CPC and BLT were severely under predicted by the conventional approach. This drastic discrepancy in the model predictions and experimental observations demonstrate that the conventional approach of using the correlation parameters from Nusselt heat transfer correlation for Sherwood mass transfer correlation is not a sound approach of estimating the extent of concentration polarization in DCMD system operated at high solute concentrations. A novel approach is therefore required to truly understand the effect of concentration polarization and to estimate the CPC and BLT in these membrane systems.

8.0 OUTLOOK

The research presented in this document helped address several questions with respect to energetics and fundamental understanding of membrane distillation while also challenging conventional approaches followed by the membrane-related studies.

Chapter 2 discussed the viability of membrane distillation in desalination of high salinity brines generated from the oil and gas industry. It was demonstrated that MD can successfully desalinate produced water with minimal degradation of permeate quality and flux due to membrane fouling. The tests carried out in this chapter were limited to 3 days of continuous operation due to limited resources. In addition, the dependence of the membrane distillation coefficient on the properties of membrane active layer and support was also proven. While commercially available hydrophobic microfiltration membranes were used for MD application in this study, the membranes were not designed specifically for this application. Chapter 3 evaluated the potential of DCMD for treatment of produced water generated during extraction of natural gas from unconventional (shale) reservoirs by using waste heat from the exhaust stream from natural gas compressor station as the energy source to operate DCMD. The ASPEN Plus model used in this work was used to optimize the membrane area in a single module and the optimized membrane module was employed in a series parallel configuration to design a plant scale DCMD system. The model was then used for a case study to evaluate the energy requirements of DCMD for treating all produced water generated in the state of Pennsylvania by assuming that the produced water was

available at the same treatment facility. The ASPEN Plus model was also employed in Chapter 4 to emphasize the importance of feed recirculation in MD on its thermal and electrical energy requirements.

Based on the works described in Chapter 2, 3 and 4, studies focusing in the following direction would be beneficial for further developing membrane distillation and also evaluating its performance in the real world:

- A study focused on developing a robust hydrophobic membrane specifically for MD applications by altering the porosity and thickness to maximize the MD coefficient and minimize the thermal conductivity would be an important step towards the advancement of membrane distillation.
- Application of knowledge generated in Chapter 3 and 4 towards integration of membrane distillation with waste heat sources and evaluating the long term performance of a pilot scale membrane distillation system with real world high salinity brines would be truly beneficial in understanding the energetics, effects of membrane fouling and other challenges that the research community may have overlooked due to the small scale of testing.

Chapter 5 was focused on development and demonstration of a novel technique for characterization of the concentration gradient at the feed-membrane interface due to concentration polarization. Chapter 6 aimed at probing the concentration gradient using the spectrophotometric method to evaluate the effect of operating conditions on the concentration gradient. An interesting discovery from this work was that the conventional approach of estimation of concentration polarization coefficient and boundary layer thickness did not match with experimentally obtained

results. Elucidating why the conventional approach does not work would be instrumental in understanding the fundamentals of mass transfer through a porous medium and developing a new approach towards accurately estimating the solute concentration at the membrane surface.

APPENDIX A

A.1 SUPPORTING INFORMATION FOR CHAPTER 3

Assumptions used in ASPEN Plus simulations

1. The process is in a steady state.
2. Heat energy lost to the surroundings is assumed to be negligible.
3. Membrane wetting does not occur.
4. Salt rejection is assumed to be 100%.
5. For modelling the DCMD process, the tolerance for the relative difference between two subsequent iterations was 0.1%.
6. As sodium chloride is the main constituent of the salts present in produced water, the simulations were carried out with sodium chloride as the dissolved salt.
7. It is assumed that a plant scale system would be equipped with a pretreatment facility to remove the scale forming salts prior to treatment using DCMD. Hence, it was assumed that there will be no membrane fouling.

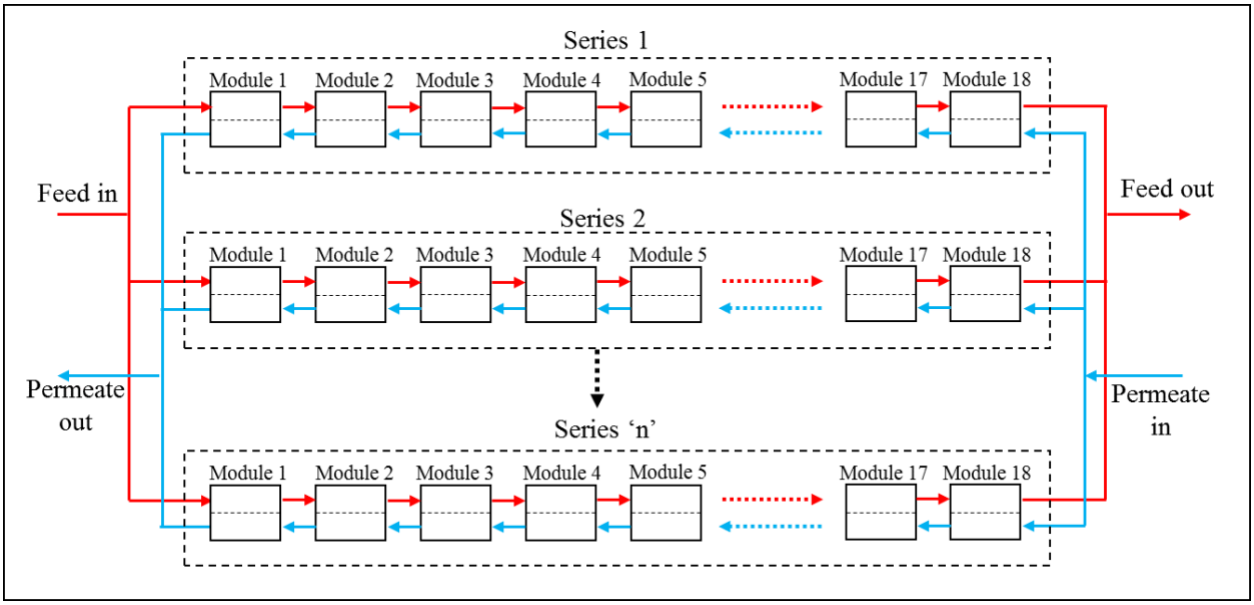

Figure A1. Schematic diagram of a series-parallel arrangement of DCMD modules.

Table A1. Characteristics of membrane used for simulation

Mean pore size		0.24 µm
Thickness	Total	148 ± 30 µm
	Active layer	60 ± 5 µm
Water contact angle		149 ± 3 °
Liquid entry pressure		15.5 ± 1.9 psi
Porosity		60 ± 6.8
Thermal conductivity		0.242 W/mK
Membrane distillation coefficient		5.6 LMH/kPa

Table A2. Characteristics of spacer used for simulation

Voidage	0.77
Diameter of spacer filament	1.2 mm
Spacer thickness	1.9 mm
Spacer angle	90 ^{o}
Mesh size	3.5 mm

A.2 SUPPORTING INFORMATION FOR CHAPTER 4

A.2.1 Material balance calculations used to determine the recycle ratio for a continuous direct contact membrane distillation system with a specified water recovery:

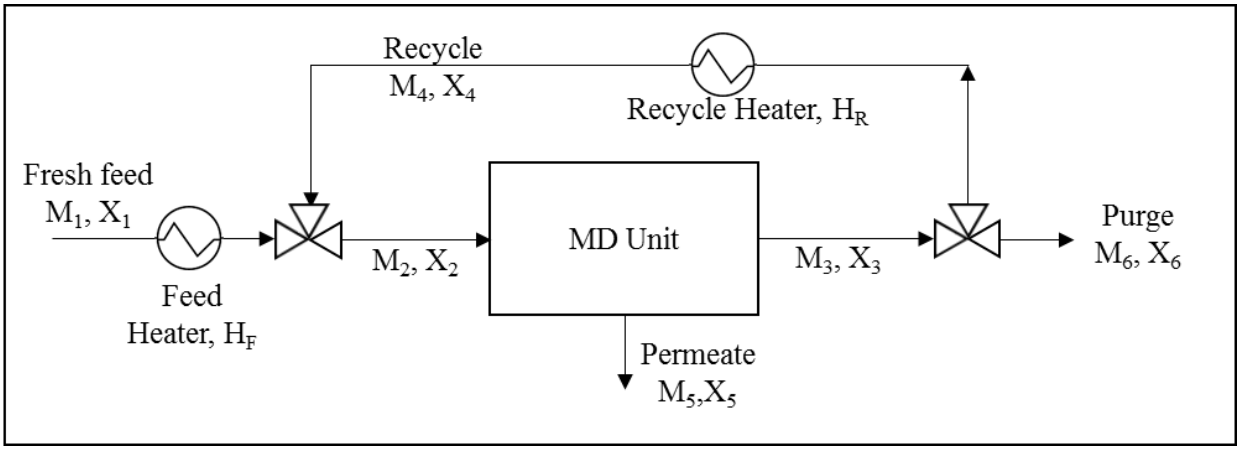

Figure A2. Schematic diagram of a continuous MD system with recycle and purge streams. M represents mass flow rate whereas X represents the concentration of salt in each streams.

Variables:

Mass flow rates (kg/s) = M_1, M_2, M_3, M_4, M_5, M_6

Salt Concentration (g/l) = X_1, X_2, X_3, X_4, X_5, X_6

Fresh feed, M_1= 1 kg/s

X_1 = 100 g/kg

Desired recovery = W %

Single pass conversion = x % (i.e., g of permeate/100g of feed)

For stream 5,

$$M_5 = \left(\frac{W}{100}\right) \times M_1$$

$$X_5 = 0$$

For stream 6,

$$M_6 = M_1 - M_5$$

$$X_6 = \frac{M_1 \times X_1}{M_6}$$

$$X_6 = X_3 = X_4$$

For stream 2,

$$M_2 = M_1 + M_4$$

$$X_2 = \frac{(M_1 \times X_1) + (M_4 \times X_4)}{M_2}$$

For stream 3,

$$M_3 = \left(\frac{100 - x}{100}\right) \times M_2$$

$$X_3 = \frac{M_2 \times X_2}{M_3}$$

The recycle ratio, i.e. M_4/M_1, can be obtained by solving for M_4 using the above set of equations.

A.2.2 Electrical energy requirements for pumping the recycle stream

The electrical energy requirement for pumping the recycle stream was obtained from the following equation:

$$E = \frac{Q \times \Delta P}{\alpha}$$

where E is the electrical energy consumption, Q is the mass flow rate through the pump, ΔP is the pressure difference and α is the pump efficiency. The flow rate of recycle stream was obtained through ASPEN Plus simulations, while the ΔP and α were assumed to be 20 psi and 80% respectively.

A.3 SUPPORTING INFORMATION FOR CHAPTER 5

A.3.1 Statistical analysis - Variance between measurements at different pixel numbers

Data in the feed bulk was recorded at 200 pixels that corresponds to a length of 900 μm. The variation in the measurements at each of these 200 pixels was analyzed using ANOVA at fixed operating conditions of feed flow rate, temperature and bulk concentration. The response variable, i.e., absorbance in this case, was given as y_{ijkl}, where, i = feed temperature (30, 40 and 50°C), j = pixel number (1, 2, 3, ..., 200), k = feed flow rate (0.2, 0.4 and 0.6 LPM) and l = bulk feed concentration (5.4, 13.6, 27.3, 40.9 and 54.5 g/L). Table A3 shows the p values for pixel numbers at each of the fixed bulk feed concentrations calculated using multi-factor ANOVA.

Table A3. p values for pixel numbers calculated using ANOVA.

Concentration (g/L)	p values for pixel numbers
5.5	0.99
13.6	0.17
27.3	0.28
40.9	0.36
54.6	0.05

All p values in Table A3 are greater than or equal to 0.05, thereby, indicating that the influence of pixel number on the measurement of absorbance values in the bulk feed was not significant (at a level of significance = $\alpha = 0.05$). Figure A3 supports the validity of the ANOVA analysis, showing that the analyzed data follows the normal probability plot and that the residuals are randomly distributed. The maximum coefficient of variation (CV) measured for absorbance measurements with varying pixel numbers was 5.1% for temperature experiments and was 5.9% for flow rate experiments.

(a)

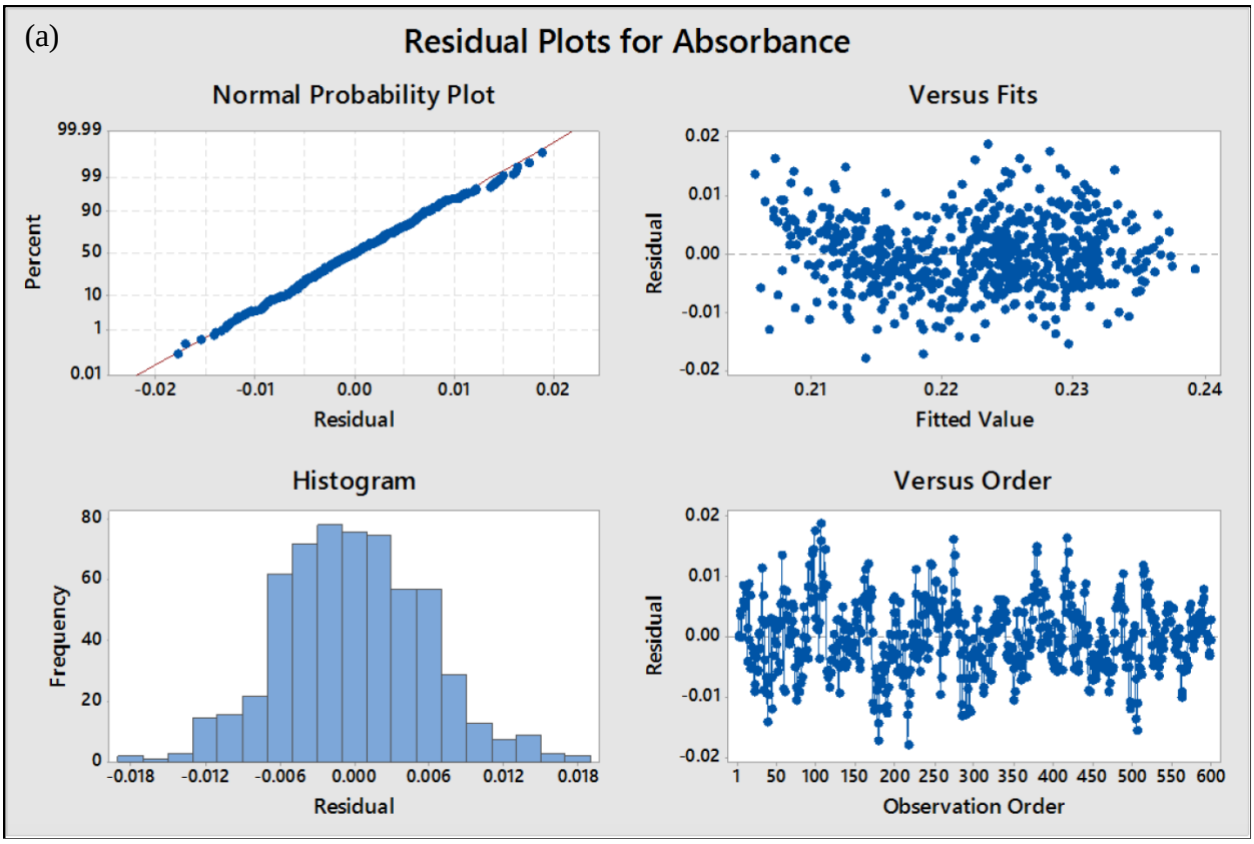
Residual Plots for Absorbance
Normal Probability Plot
Percent
99.99
99
90
50
10
1
0.01
-0.02
-0.01
0.00
0.01
0.02
Residual
Versus Fits
Residual
0.02
0.01
0.00
-0.01
-0.02
0.21
0.22
0.23
0.24
Fitted Value
Histogram
Frequency
80
60
40
20
0
-0.018
-0.012
-0.006
0.000
0.006
0.012
0.018
Residual
Versus Order
Residual
0.02
0.01
0.00
-0.01
-0.02
1
50
100
150
200
250
300
350
400
450
500
550
600
Observation Order

(b)

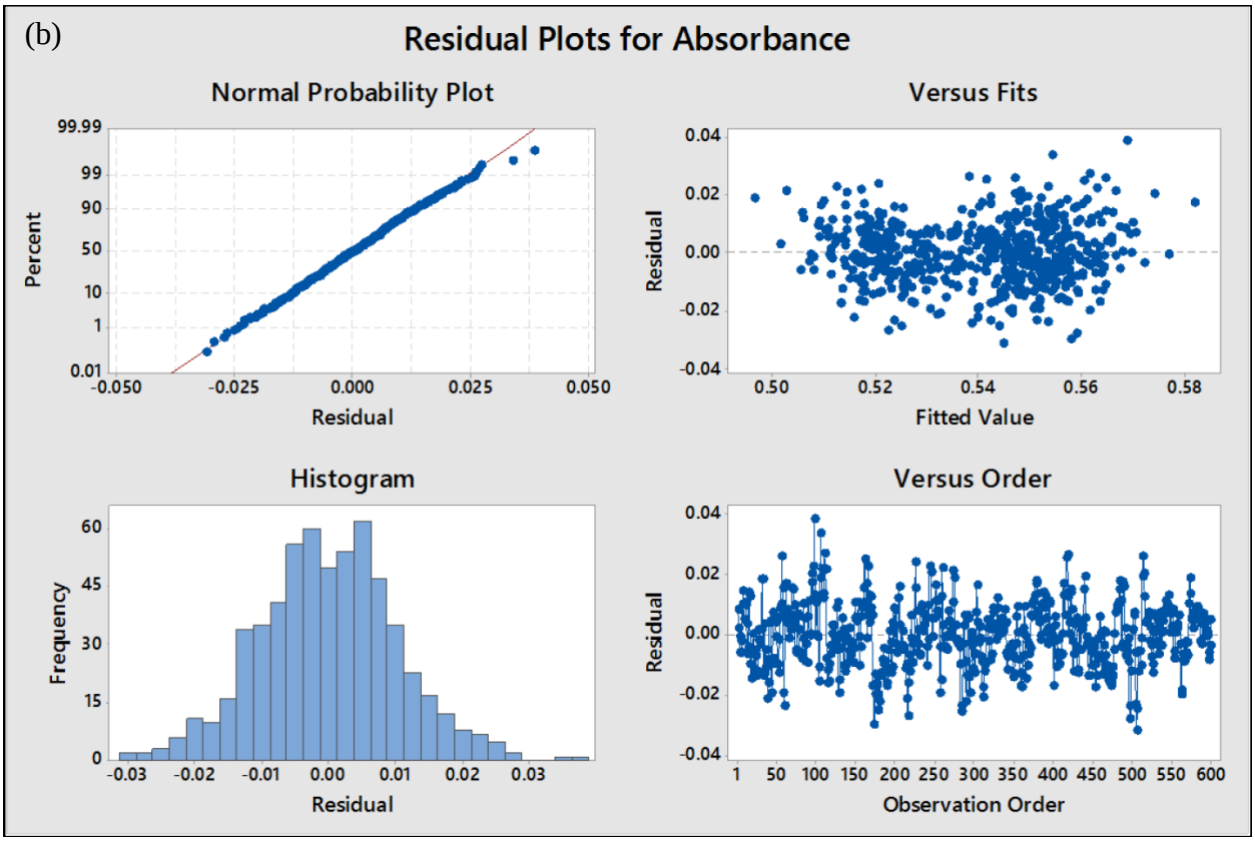
Residual Plots for Absorbance
Normal Probability Plot
Percent
99.99
99
90
50
10
1
0.01
-0.050
-0.025
0.000
0.025
0.050
Residual
Versus Fits
Residual
0.04
0.02
0.00
-0.02
-0.04
0.50
0.52
0.54
0.56
0.58
Fitted Value
Histogram
Frequency
60
45
30
15
0
-0.03
-0.02
-0.01
0.00
0.01
0.02
0.03
Residual
Versus Order
Residual
0.04
0.02
0.00
-0.02
-0.04
1
50
100
150
200
250
300
350
400
450
500
550
600
Observation Order

(c)

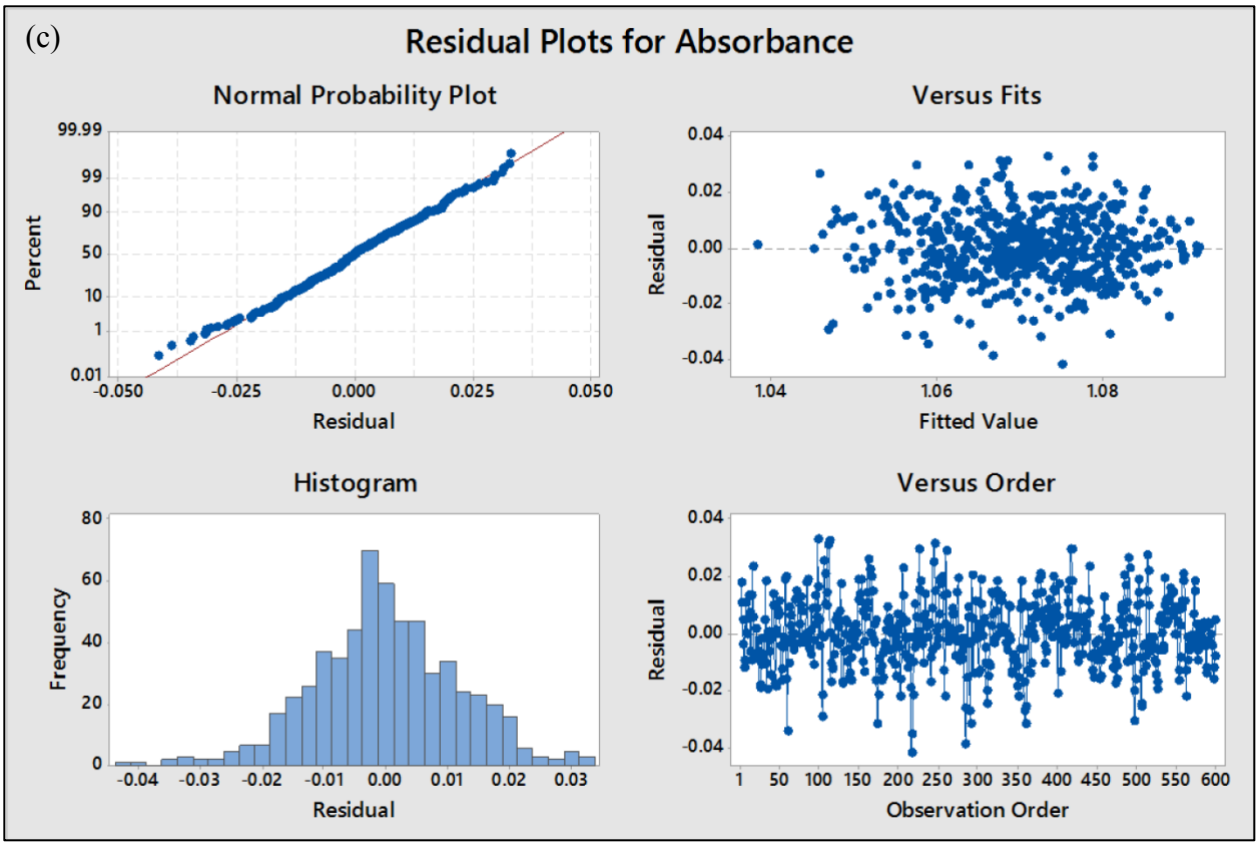
Residual Plots for Absorbance
Normal Probability Plot
Percent
99.99
99
90
50
10
1
0.01
-0.050
-0.025
0.000
0.025
0.050
Residual
Versus Fits
Residual
0.04
0.02
0.00
-0.02
-0.04
1.04
1.06
1.08
Fitted Value
Histogram
Frequency
80
60
40
20
0
-0.04
-0.03
-0.02
-0.01
0.00
0.01
0.02
0.03
Residual
Versus Order
Residual
0.04
0.02
0.00
-0.02
-0.04
1
50
100
150
200
250
300
350
400
450
500
550
600
Observation Order

(d)

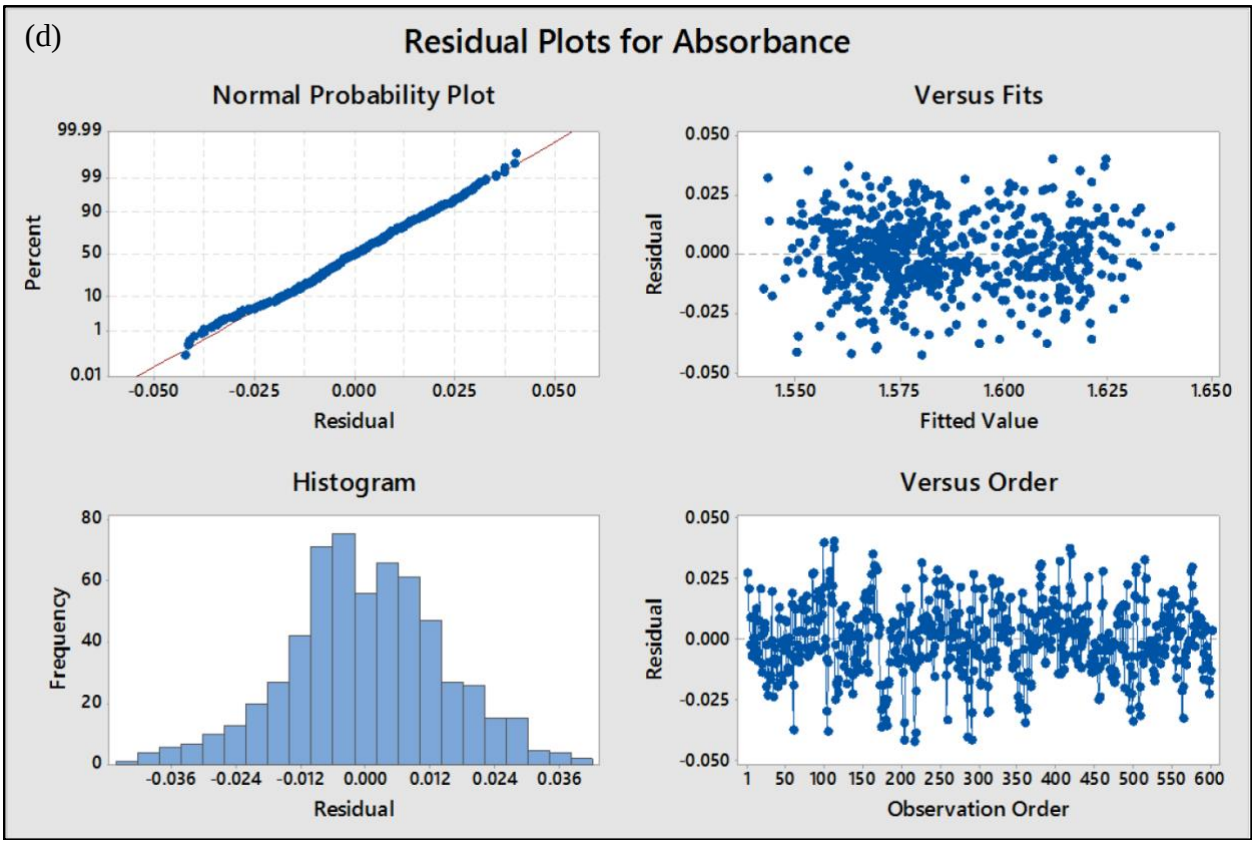
Residual Plots for Absorbance
Normal Probability Plot
Percent
99.99
99
90
50
10
1
0.01
-0.050
-0.025
0.000
0.025
0.050
Residual
Versus Fits
Residual
0.050
0.025
0.000
-0.025
-0.050
1.550
1.575
1.600
1.625
1.650
Fitted Value
Histogram
Frequency
80
60
40
20
0
-0.036
-0.024
-0.012
0.000
0.012
0.024
0.036
Residual
Versus Order
Residual
0.050
0.025
0.000
-0.025
-0.050
1
50
100
150
200
250
300
350
400
450
500
550
600
Observation Order

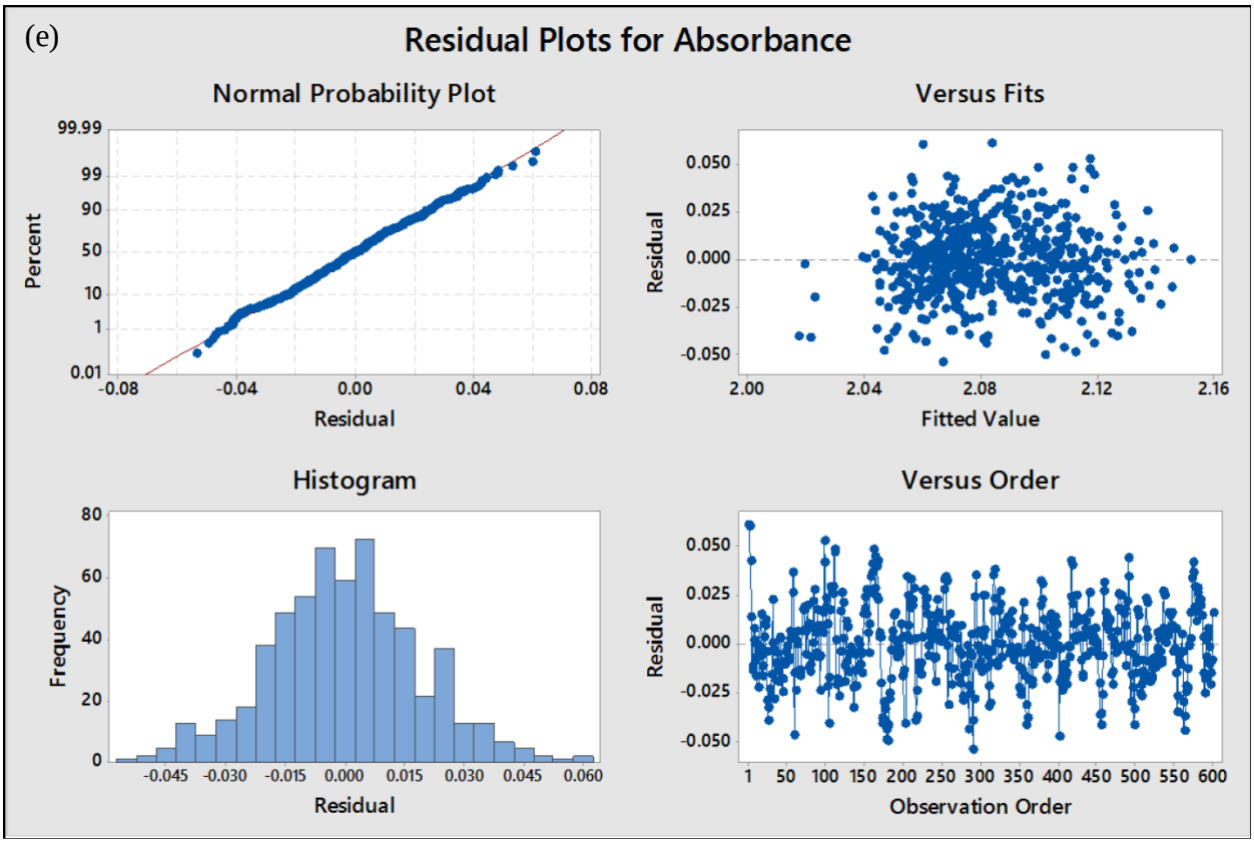

Figure A3: Normal probability and residual plots from ANOVA analysis for feed concentrations of (a) 5.4, (b) 13.6, (c) 27.3, (d) 40.9 and (e) 54.5 g/L.

A.3.2 Statistical analysis - Variance between measurements at different feed temperatures and flow rates

Effect of salt concentration on the absorbance is well established [208-210], however, it is important to determine the dependence and/or variation in the measurement of absorbance values with changes in feed temperature and flow rate. Multi-linear regression with interactions and indicator variables was used to test this variation. Two separate models were fitted: (1) fixed feed flow rate and varying bulk feed concentration and temperature to determine the variation caused by temperature and (2) fixed feed temperature and varying bulk feed concentration and flow rate

to determine the variation caused by flow rate. The following multi-linear regression model was fitted to the experimentally measured data:

$$y = \beta_0 + \beta_1 x_1 + \beta_2 x_2 + \beta_3 x_3 + \beta_4 x_1 x_2 + \beta_5 x_1 x_3 + \in$$

where, y is the response variable or absorbance in our case, $\beta_0, \beta_1, \beta_2, \beta_3, \beta_4 \; and \; \beta_5$ are fitting constants, x_1 is the bulk feed concentration (5.4, 13.6, 27.3, 40.9 and 54.5 g/L), x_2 and x_3 are indicator variables representing feed temperature or flow rate and $\in$ is the error in measurement. Table A4 gives the values that the indicator variables assume for the feed temperatures and flow rates in their respective models.

Table A4. Values of indicator variables for the respective cases of feed temperatures and flow rates.

Feed temperature (°C)	**Value of x_2**	**Value of x_3**
40	0	0
50	1	0
60	0	1
Feed flow rate (LPM)	**Value of x_2**	**Value of x_3**
0.2	0	0
0.4	1	0
0.6	0	1

The null hypothesis was tested to check the dependence of absorbance values on feed temperature and feed flow rate and also on their respective interactions with bulk feed concentration. In all cases, the p values were < 0.001 indicating the both feed temperature and flow

rate significantly affected the measurement of absorbance values using our developed technique. The regression equations obtained are as follows:

For feed temperature dependence:

$$y = 0.02235 + 0.02097x_1 - 0.00862\,x_2 + 0.01178\,x_3 - 0.00025\,x_1x_2 - 0.00052\,x_1x_3$$

For feed flow rate dependence:

$$y = 0.02235 + 0.01980x_1 - 0.03735\,x_2 + 0.00219\,x_3 + 0.00089\,x_1x_2 - 0.00118\,x_1x_3$$

However, when the raw data was plotted to check the dependence of the measured absorbance values as a function of feed temperature and feed flow rate, a complete random behavior was determined. Figure A4(a) and (b) show randomly picked absorbance values for 5 pixel numbers at fixed bulk feed concentration but varying feed temperature and flow rate respectively.

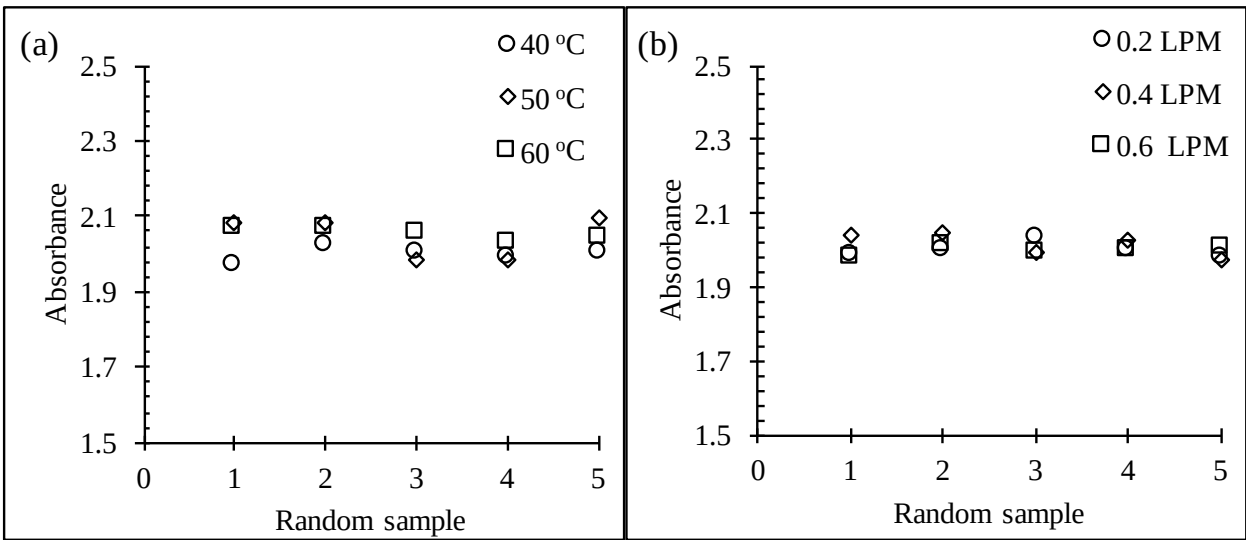

Figure A4. Randomly picked absorbance values when the feed concentration was 54.5 g/l at (a) varying feed temperature and (b) varying feed flow rates.

Hence, in this study, the effect of feed temperature and flow rate will be regarded as completely random and bulk feed concentration will be considered as the only factor affecting the measurement of absorbance values. Nevertheless, the maximum coefficient of variation (CV)

introduced by changing feed temperature was 3.62% and that by changing feed flow rate was 7.63%. Table A5 shows the coefficient of variation values for measurement of absorbance values with varying feed temperature and flow rate at each of the five respective bulk feed concentrations.

Table A5: Coefficient of variation in the measurement of absorbance values.

Bulk feed concentration (g/L)	CV for feed temperature	CV for feed flow rate
10	3.62%	7.54%
25	2.90%	4.22%
50	0.533%	1.08%
75	1.22%	1.86%
100	1.04%	7.63%

A.3.3 UV-Vis absorption spectra of metal salts

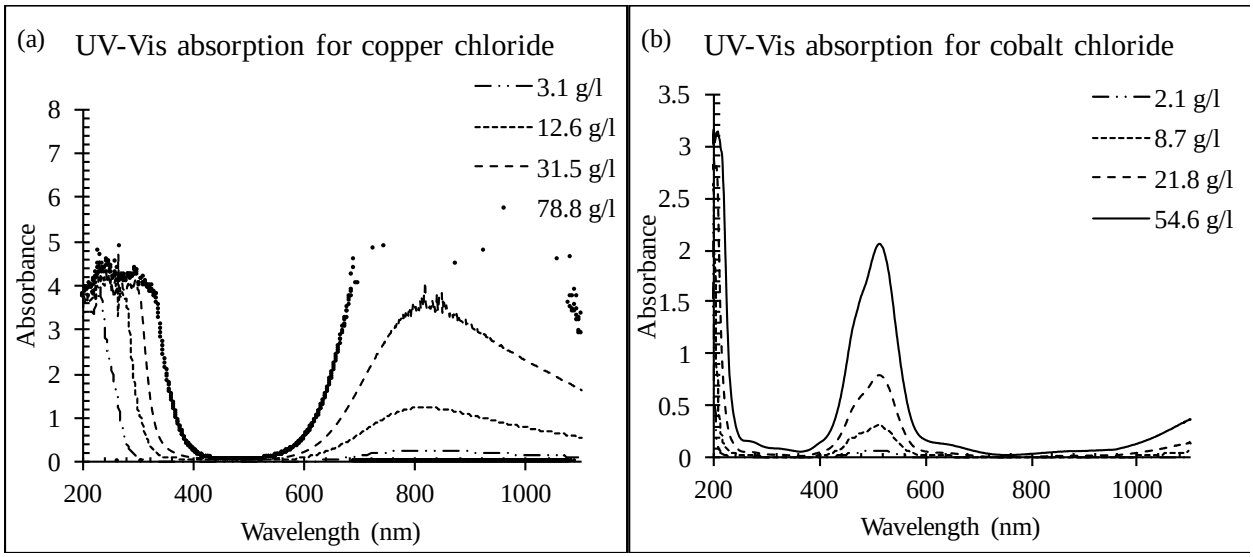

Figure A5. UV-Vis absorption spectra for (a) copper chloride and (b) cobalt chloride at different concentrations.

A.4 SUPPORTING INFORMATION FOR CHAPTER 6

Table A6. Membrane Properties [124]

Pore size (μm)	Thickness (μm)		Contact angle (active layer)	LEP (psi)	% Porosity of membrane		Thermal Conductivity (W/mK)	MD coefficient (LMH/kPa)
	Total	Active layer			Bulk	Active layer		
0.21	112	20	142	40.3	42	92	0.294	4.4

Table A7. Experimental conditions used for validating the Nusselt correlations with pure water as feed.

Feed flow (LPM), [velocity (m/s)]	Permeate flow (LPM), [velocity (m/s)]	Feed temperature (^oC)	Permeate temperature (^oC)	Flux (LMH)
0.5 [0.069]	0.2 [0.22]	60	20	25.9
0.5 [0.069]	0.2 [0.22]	50	20	17.1
0.5 [0.069]	0.2 [0.22]	40	20	7.9
0.2 [0.028]	0.1 [0.11]	50	20	11.3
0.4 [0.056]	0.1 [0.11]	50	20	14.4
0.6 [0.083]	0.1 [0.11]	50	20	15

BIBLIOGRAPHY

[1] U.S. EIA, Technically Recoverable Shale Oil and Shale Gas Resources: An Assessment of 137 Shale Formations in 41 Countries Outside the United States, in, Washington, DC, June 2013.

[2] U.S. EIA, Annual Energy Outlook 2015, in, Washington, DC, April 2015.

[3] USEIA, US Energy Information Administration, https://www.eia.gov/todayinenergy/detail.php?id=32412 (accessed October 4, 2017), (2017).

[4] D.T. Allen, V.M. Torres, J. Thomas, D.W. Sullivan, M. Harrison, A. Hendler, S.C. Herndon, C.E. Kolb, M.P. Fraser, A.D. Hill, Measurements of methane emissions at natural gas production sites in the United States, Proceedings of the National Academy of Sciences, 110 (2013) 17768-17773.

[5] A.T. Dale, V. Khanna, R.D. Vidic, M.M. Bilec, Process based life-cycle assessment of natural gas from the Marcellus Shale, Environmental science & technology, 47 (2013) 5459-5466.

[6] R.B. Jackson, A. Vengosh, T.H. Darrah, N.R. Warner, A. Down, R.J. Poreda, S.G. Osborn, K. Zhao, J.D. Karr, Increased stray gas abundance in a subset of drinking water wells near Marcellus shale gas extraction, Proceedings of the National Academy of Sciences, 110 (2013) 11250-11255.

[7] G.T. Llewellyn, F. Dorman, J. Westland, D. Yoxtheimer, P. Grieve, T. Sowers, E. Humston-Fulmer, S.L. Brantley, Evaluating a groundwater supply contamination incident attributed to Marcellus Shale gas development, Proceedings of the National Academy of Sciences, 112 (2015) 6325-6330.

[8] E. Mielke, L.D. Anadon, V. Narayanamurti, Water consumption of energy resource extraction, processing, and conversion, Belfer Center for Science and International Affairs, (2010).

[9] R. Vidic, S. Brantley, J. Vandenbossche, D. Yoxtheimer, J. Abad, Impact of shale gas development on regional water quality, Science, 340 (2013) 1235009.

[10] K.B. Gregory, R.D. Vidic, D.A. Dzombak, Water management challenges associated with the production of shale gas by hydraulic fracturing, Elements, 7 (2011) 181-186.

[11] J.D. Arthur, B. Bohm, M. Layne, Hydraulic fracturing considerations for natural gas wells of the Marcellus Shale, in: The Ground Water Protection Council 2008 Annual Forum, Cincinnati, Ohio, 2008, pp. 16.

[12] L.O. Haluszczak, A.W. Rose, L.R. Kump, Geochemical evaluation of flowback brine from Marcellus gas wells in Pennsylvania, USA, Applied Geochemistry, 28 (2013) 55-61.

[13] E. Barbot, N.S. Vidic, K.B. Gregory, R.D. Vidic, Spatial and temporal correlation of water quality parameters of produced waters from Devonian-age shale following hydraulic fracturing, Environmental science & technology, 47 (2013) 2562-2569.

[14] R.D. Vidic, S.L. Brantley, J.M. Vandenbossche, D. Yoxtheimer, J.D. Abad, Impact of shale gas development on regional water quality, Science, 340 (2013) 1235009.

[15] J.A. Slutz, J.A. Anderson, R. Broderick, P.H. Horner, Key shale gas water management strategies: an economic assessment, in: International Conference on Health, Safety and Environment in Oil and Gas Exploration and Production, Society of Petroleum Engineers, 2012.

[16] Marcellus Region production continues growth, in, U.S. Department of Energy, Energy Information Administration, 2014.

[17] M. Pathak, H. Kweon, P. Panja, R. Velasco, M.D. Deo, Suppression in the Bubble Points of Oils in Shales Combined Effect of Presence of Organic Matter and Confinement, in: SPE Unconventional Resources Conference, Society of Petroleum Engineers, 2017.

[18] J.A. Veil, M.G. Puder, D. Elcock, R.J. Redweik Jr, A white paper describing produced water from production of crude oil, natural gas, and coal bed methane, Argonne National Laboratory, Technical Report, (2004).

[19] J. Gao, F. You, Optimal design and operations of supply chain networks for water management in shale gas production: MILFP model and algorithms for the water-energy nexus, AIChE Journal, 61 (2015) 1184-1208.

[20] R. McCurdy, Underground injection wells for produced water disposal, in: USEPA Technical Workshops for the Hydraulic Fracturing Study: Water Resource Management. United States Environmental Protection Agency, Office of Research and Development, 2011.

[21] J.A. Slutz, J.A. Anderson, R. Broderick, P.H. Horner, Key Shale Gas Water Management Strategies: An Economic Assessment, in, Society of Petroleum Engineers.

[22] T. Hayes, T. Smith, Techno-economic Assessment of Water Management Solutions, Marcellus Shale Gas Water Management Initiative, Canonsburg, PA, (2011).

[23] D.M. Kargbo, R.G. Wilhelm, D.J. Campbell, Natural gas plays in the Marcellus shale: Challenges and potential opportunities, Environmental science & technology, 44 (2010) 5679-5684.

[24] W.L. Ellsworth, Injection-induced earthquakes, Science, 341 (2013) 1225942.

[25] M. Zoback, S. Kitasei, B. Copithorne, Addressing the environmental risks from shale gas development, Worldwatch Institute, 2010.

[26] K.M. Keranen, M. Weingarten, G.A. Abers, B.A. Bekins, S. Ge, Sharp increase in central Oklahoma seismicity since 2008 induced by massive wastewater injection, Science, 345 (2014) 448-451.

[27] A. McGarr, B. Bekins, N. Burkardt, J. Dewey, P. Earle, W. Ellsworth, S. Ge, S. Hickman, A. Holland, E. Majer, J. Rubinstein, A. Sheehan, Coping with earthquakes induced by fluid injection, Science, 347 (2015) 830-831.

[28] SAFER PA, The Shale Alliance for Energy Research, Pennsylvania, Life cycle management of future waste challengers for shale development in Pennsylvania, http://www.saferpa.org/Pages/Life-Cycle-Management-of-Future-Waste-Challenges-4-Shale-Development-in-PA.aspx (accessed July 18, 2017), (2015).

[29] U.K. Kesieme, N. Milne, H. Aral, C.Y. Cheng, M. Duke, Economic analysis of desalination technologies in the context of carbon pricing, and opportunities for membrane distillation, Desalination, 323 (2013) 66-74.

[30] N. Ghaffour, T.M. Missimer, G.L. Amy, Technical review and evaluation of the economics of water desalination: current and future challenges for better water supply sustainability, Desalination, 309 (2013) 197-207.

[31] T. Mezher, H. Fath, Z. Abbas, A. Khaled, Techno-economic assessment and environmental impacts of desalination technologies, Desalination, 266 (2011) 263-273.

[32] G.P. Thiel, E.W. Tow, L.D. Banchik, H.W. Chung, J.H. Lienhard V, Energy consumption in desalinating produced water from shale oil and gas extraction, Desalination, 366 (2015) 94-112.

[33] A. Subramani, J.G. Jacangelo, Emerging desalination technologies for water treatment: A critical review, Water research, 75 (2015) 164-187.

[34] B. Li, K.K. Sirkar, Novel Membrane and Device for Direct Contact Membrane Distillation-Based Desalination Process, Industrial & Engineering Chemistry Research, 43 (2004) 5300-5309.

[35] T.Y. Cath, V.D. Adams, A.E. Childress, Experimental study of desalination using direct contact membrane distillation: a new approach to flux enhancement, Journal of Membrane Science, 228 (2004) 5-16.

[36] M. Shirazi, Desalination of saline water using direct contact membrane distillation, J. Appl. Chem. Res, 17 (2011) 28-36.

[37] W. Chen, S. Chen, Q. Zhang, Z. Fan, K.-W. Huang, X. Zhang, Z. Lai, P. Sheng, High-flux water desalination with interfacial salt sieving effect in nanoporous carbon composite membranes, arXiv preprint arXiv:1604.07567, (2016).

[38] U.K. Kesieme, N. Milne, C.Y. Cheng, H. Aral, M. Duke, Recovery of water and acid from leach solutions using direct contact membrane distillation, Water Science and Technology, 69 (2014) 868-875.

[39] M. Xie, L.D. Nghiem, W.E. Price, M. Elimelech, A forward osmosis–membrane distillation hybrid process for direct sewer mining: system performance and limitations, Environmental science & technology, 47 (2013) 13486-13493.

[40] M. Gryta, K. Karakulski, A. Morawski, Purification of oily wastewater by hybrid UF/MD, Water research, 35 (2001) 3665-3669.

[41] C.M. Tun, A.G. Fane, J.T. Matheickal, R. Sheikholeslami, Membrane distillation crystallization of concentrated salts—flux and crystal formation, Journal of Membrane Science, 257 (2005) 144-155.

[42] X. Ji, E. Curcio, S. Al Obaidani, G. Di Profio, E. Fontananova, E. Drioli, Membrane distillation-crystallization of seawater reverse osmosis brines, Separation and Purification Technology, 71 (2010) 76-82.

[43] B. Li, K.K. Sirkar, Novel membrane and device for vacuum membrane distillation-based desalination process, Journal of Membrane Science, 257 (2005) 60-75.

[44] G. Meindersma, C. Guijt, A. De Haan, Desalination and water recycling by air gap membrane distillation, Desalination, 187 (2006) 291-301.

[45] L. Martinez, Comparison of membrane distillation performance using different feeds, Desalination, 168 (2004) 359-365.

[46] P. Zolotarev, V. Ugrozov, I. Volkina, V. Nikulin, Treatment of waste water for removing heavy metals by membrane distillation, Journal of hazardous materials, 37 (1994) 77-82.

[47] G. Zakrzewska-Trznadel, M. Harasimowicz, A.G. Chmielewski, Concentration of radioactive components in liquid low-level radioactive waste by membrane distillation, Journal of Membrane Science, 163 (1999) 257-264.

[48] S. Hsu, K. Cheng, J.-S. Chiou, Seawater desalination by direct contact membrane distillation, Desalination, 143 (2002) 279-287.

[49] V. Calabro, B.L. Jiao, E. Drioli, Theoretical and experimental study on membrane distillation in the concentration of orange juice, Industrial & engineering chemistry research, 33 (1994) 1803-1808.

[50] S. Gunko, S. Verbych, M. Bryk, N. Hilal, Concentration of apple juice using direct contact membrane distillation, Desalination, 190 (2006) 117-124.

[51] V. Alves, I. Coelhoso, Orange juice concentration by osmotic evaporation and membrane distillation: a comparative study, Journal of Food Engineering, 74 (2006) 125-133.

[52] M. Tomaszewska, M. Gryta, A. Morawski, Study on the concentration of acids by membrane distillation, Journal of Membrane Science, 102 (1995) 113-122.

[53] S.G. Osborn, A. Vengosh, N.R. Warner, R.B. Jackson, Methane contamination of drinking water accompanying gas-well drilling and hydraulic fracturing, proceedings of the National Academy of Sciences, 108 (2011) 8172-8176.

[54] S.M. Olmstead, L.A. Muehlenbachs, J.-S. Shih, Z. Chu, A.J. Krupnick, Shale gas development impacts on surface water quality in Pennsylvania, Proceedings of the National Academy of Sciences, 110 (2013) 4962-4967.

[55] D. Rahm, Regulating hydraulic fracturing in shale gas plays: The case of Texas, Energy Policy, 39 (2011) 2974-2981.

[56] C. Clark, J. Veil, Produced water volumes and management practices in the United States, in, Argonne National Laboratory (ANL), 2009.

[57] Y. Zhang, K. Ghyselbrecht, R. Vanherpe, B. Meesschaert, L. Pinoy, B. Van der Bruggen, RO concentrate minimization by electrodialysis: Techno-economic analysis and environmental concerns, Journal of Environmental Management, 107 (2012) 28-36.

[58] R. Bouchrit, A. Boubakri, A. Hafiane, S.A.-T. Bouguecha, Direct contact membrane distillation: Capability to treat hyper-saline solution, Desalination, 376 (2015) 117-129.

[59] J.B. Gálvez, L. García-Rodríguez, I. Martín-Mateos, Seawater desalination by an innovative solar-powered membrane distillation system: the MEDESOL project, Desalination, 246 (2009) 567-576.

[60] N.A. Elsayed, M.A. Barrufet, M.M. El-Halwagi, An integrated approach for incorporating thermal membrane distillation in treating water in heavy oil recovery using SAGD, Journal of Unconventional Oil and Gas Resources, 12 (2015) 6-14.

[61] D. Singh, K.K. Sirkar, Desalination of brine and produced water by direct contact membrane distillation at high temperatures and pressures, Journal of Membrane Science, 389 (2012) 380-388.

[62] D. Singh, P. Prakash, K.K. Sirkar, Deoiled produced water treatment using direct-contact membrane distillation, Industrial & Engineering Chemistry Research, 52 (2013) 13439-13448.

[63] F. Macedonio, A. Ali, T. Poerio, E. El-Sayed, E. Drioli, M. Abdel-Jawad, Direct contact membrane distillation for treatment of oilfield produced water, Separation and Purification Technology, 126 (2014) 69-81.

[64] H.C. Duong, S. Gray, M. Duke, T.Y. Cath, L.D. Nghiem, Scaling control during membrane distillation of coal seam gas reverse osmosis brine, Journal of Membrane Science, 493 (2015) 673-682.

[65] H.C. Duong, A.R. Chivas, B. Nelemans, M. Duke, S. Gray, T.Y. Cath, L.D. Nghiem, Treatment of RO brine from CSG produced water by spiral-wound air gap membrane distillation—A pilot study, Desalination, 366 (2015) 121-129.

[66] X. Zhang, Z. Guo, C. Zhang, J. Luan, Exploration and optimization of two-stage vacuum membrane distillation process for the treatment of saline wastewater produced by natural gas exploitation, Desalination, 385 (2016) 117-125.

[67] R.E. Kesting, Synthetic polymeric membranes, McGraw-Hill, 1971.

[68] M. Khayet, T. Matsuura, Preparation and characterization of polyvinylidene fluoride membranes for membrane distillation, Industrial & Engineering Chemistry Research, 40 (2001) 5710-5718.

[69] K. Smolders, A. Franken, Terminology for membrane distillation, Desalination, 72 (1989) 249-262.

[70] ASTM, E1461-13, Standard Test Method for Thermal Diffusivity by the Flash Method, ASTM International, West Conshohocken, PA, 2013, http://www.astm.org/, in.

[71] E. EPA, Method 901.1: Gamma Emitting Radionuclides in Drinking Water, in: Prescribed Procedures for Measurement of Radioactivity in Drinking Water, 1980.

[72] T. Zhang, D. Bain, R. Hammack, R.D. Vidic, Analysis of Radium-226 in High Salinity Wastewater from Unconventional Gas Extraction by Inductively Coupled Plasma-Mass Spectrometry, Environmental Science & Technology, 49 (2015) 2969-2976.

[73] L.D. Tijing, Y.C. Woo, J.-S. Choi, S. Lee, S.-H. Kim, H.K. Shon, Fouling and its control in membrane distillation—A review, Journal of Membrane Science, 475 (2015) 215-244.

[74] D.M. Warsinger, J. Swaminathan, E. Guillen-Burrieza, H.A. Arafat, J.H. Lienhard V, Scaling and fouling in membrane distillation for desalination applications: A review, Desalination, 356 (2015) 294-313.

[75] S. Adham, A. Hussain, J.M. Matar, R. Dores, A. Janson, Application of membrane distillation for desalting brines from thermal desalination plants, Desalination, 314 (2013) 101-108.

[76] A. Criscuoli, M.C. Carnevale, E. Drioli, Evaluation of energy requirements in membrane distillation, Chemical Engineering and Processing: Process Intensification, 47 (2008) 1098-1105.

[77] J. Phattaranawik, R. Jiraratananon, A. Fane, Heat transport and membrane distillation coefficients in direct contact membrane distillation, Journal of Membrane Science, 212 (2003) 177-193.

[78] J. Zhang, N. Dow, M. Duke, E. Ostarcevic, S. Gray, Identification of material and physical features of membrane distillation membranes for high performance desalination, Journal of Membrane Science, 349 (2010) 295-303.

[79] Y. Yun, R. Ma, W. Zhang, A. Fane, J. Li, Direct contact membrane distillation mechanism for high concentration NaCl solutions, Desalination, 188 (2006) 251-262.

[80] Y. Zhang, Y. Peng, S. Ji, Z. Li, P. Chen, Review of thermal efficiency and heat recycling in membrane distillation processes, Desalination, 367 (2015) 223-239.

[81] L. Martínez-Díez, M.I. Vazquez-Gonzalez, Temperature and concentration polarization in membrane distillation of aqueous salt solutions, Journal of Membrane Science, 156 (1999) 265-273.

[82] M. Khayet, M. Godino, J. Mengual, Study of asymmetric polarization in direct contact membrane distillation, Separation Science and Technology, 39 (2005) 125-147.

[83] L. Martinez-Diez, M. Vázquez-Gonzàlez, Temperature polarization in mass transport through hydrophobic porous membranes, AIChE journal, 42 (1996) 1844-1852.

[84] D. Faivre, Iron Oxides: From Nature to Applications, John Wiley & Sons, 2016.

[85] M. Gryta, Effect of iron oxides scaling on the MD process performance, Desalination, 216 (2007) 88-102.

[86] U. Schwertmann, E. Murad, Effect of pH on the formation of goethite and hematite from ferrihydrite, Clays and Clay Minerals, 31 (1983) 277-284.

[87] N. Kämpf, U. Schwertmann, Goethite and hematite in a climosequence in southern Brazil and their application in classification of kaolinitic soils, Geoderma, 29 (1983) 27-39.

[88] A. Hausmann, P. Sanciolo, T. Vasiljevic, M. Weeks, K. Schroën, S. Gray, M. Duke, Fouling mechanisms of dairy streams during membrane distillation, Journal of Membrane Science, 441 (2013) 102-111.

[89] R. McCurdy, Underground injection wells for produced water disposal, in: Proceedings of the Technical Workshops for the Hydraulic Fracturing Study: Water Resources Management. EPA, 2011.

[90] B. Bodell, Silicone rubber vapor diffusion in saline water distillation, United States Patent Serial, (1963).

[91] M. Findley, Vaporization through porous membranes, Industrial & Engineering Chemistry Process Design and Development, 6 (1967) 226-230.

[92] F. Edwie, T.-S. Chung, Development of simultaneous membrane distillation–crystallization (SMDC) technology for treatment of saturated brine, Chemical Engineering Science, 98 (2013) 160-172.

[93] G. Rácz, S. Kerker, Z. Kovács, G. Vatai, M. Ebrahimi, P. Czermak, Theoretical and Experimental Approaches of Liquid Entry Pressure Determination in Membrane Distillation Processes, Periodica Polytechnica Chemical Engineering, 58 (2014) 81-91.

[94] I. Hitsov, T. Maere, K. De Sitter, C. Dotremont, I. Nopens, Modelling approaches in Membrane Distillation: A critical review, Separation and Purification Technology, (2014).

[95] F. Laganà, G. Barbieri, E. Drioli, Direct contact membrane distillation: modelling and concentration experiments, Journal of Membrane Science, 166 (2000) 1-11.

[96] M. Khayet, A. Velázquez, J.I. Mengual, Modelling mass transport through a porous partition: effect of pore size distribution, Journal of Non-Equilibrium Thermodynamics, 29 (2004) 279-299.

[97] M. Khayet, Membranes and theoretical modeling of membrane distillation: a review, Advances in Colloid and Interface Science, 164 (2011) 56-88.

[98] T.-C. Chen, C.-D. Ho, H.-M. Yeh, Theoretical modeling and experimental analysis of direct contact membrane distillation, Journal of Membrane Science, 330 (2009) 279-287.

[99] V.A. Bui, L. Vu, M. Nguyen, Modelling the simultaneous heat and mass transfer of direct contact membrane distillation in hollow fibre modules, Journal of Membrane Science, 353 (2010) 85-93.

[100] M. Qtaishat, T. Matsuura, B. Kruczek, M. Khayet, Heat and mass transfer analysis in direct contact membrane distillation, Desalination, 219 (2008) 272-292.

[101] J. Phattaranawik, R. Jiraratananon, A. Fane, Effects of net-type spacers on heat and mass transfer in direct contact membrane distillation and comparison with ultrafiltration studies, Journal of membrane science, 217 (2003) 193-206.

[102] J. Zhang, J.-D. Li, S. Gray, Effect of applied pressure on performance of PTFE membrane in DCMD, Journal of Membrane Science, 369 (2011) 514-525.

[103] A. Fane, R. Schofield, C. Fell, The efficient use of energy in membrane distillation, Desalination, 64 (1987) 231-243.

[104] K.K. Sirkar, L. Song, Pilot-Scale Studies for Direct Contact Membrane Distillation-Based Desalination Process, in: USBR (Ed.), 2009.

[105] Y. Henderyckx, Evaporation-condensation recovery of a solution component using vapor-per-meable wall spaced from a cold wall, in, Google Patents, 1971.

[106] A. Criscuoli, Improvement of the Membrane Distillation performance through the integration of different configurations, Chemical Engineering Research and Design, 111 (2016) 316-322.

[107] S. Nene, S. Kaur, K. Sumod, B. Joshi, K. Raghavarao, Membrane distillation for the concentration of raw cane-sugar syrup and membrane clarified sugarcane juice, Desalination, 147 (2002) 157-160.

[108] A. Alklaibi, N. Lior, Membrane-distillation desalination: status and potential, Desalination, 171 (2005) 111-131.

[109] A. Alkhudhiri, N. Darwish, N. Hilal, Membrane distillation: A comprehensive review, Desalination, 287 (2012) 2-18.

[110] L. Song, Z. Ma, X. Liao, P.B. Kosaraju, J.R. Irish, K.K. Sirkar, Pilot plant studies of novel membranes and devices for direct contact membrane distillation-based desalination, Journal of Membrane Science, 323 (2008) 257-270.

[111] E. Guillen-Burrieza, A. Ruiz-Aguirre, G. Zaragoza, H.A. Arafat, Membrane fouling and cleaning in long term plant-scale membrane distillation operations, Journal of Membrane Science, 468 (2014) 360-372.

[112] A.E. Jansen, J.W. Assink, J.H. Hanemaaijer, J. van Medevoort, E. van Sonsbeek, Development and pilot testing of full-scale membrane distillation modules for deployment of waste heat, Desalination, 323 (2013) 55-65.

[113] P. Wang, T.-S. Chung, Recent advances in membrane distillation processes: Membrane development, configuration design and application exploring, Journal of Membrane Science, 474 (2015) 39-56.

[114] Y. Xu, B.-K. Zhu, Y.-y. Xu, Pilot test of vacuum membrane distillation for seawater desalination on a ship, Desalination, 189 (2006) 165-169.

[115] J.H. Hanemaaijer, J. van Medevoort, A.E. Jansen, C. Dotremont, E. van Sonsbeek, T. Yuan, L. De Ryck, Memstill membrane distillation – a future desalination technology, Desalination, 199 (2006) 175-176.

[116] S. Tavakkoli, O.R. Lokare, R.D. Vidic, V. Khanna, A Systems-level Analysis of Waste Heat Recovery Opportunities from Natural Gas Compressor Stations in the US, ACS Sustainable Chemistry & Engineering, (2016).

[117] Energy Information Agency, US Natural Gas Pipeline, in.

[118] INGAA, Natural Gas Pipeline and Storage Infrastructure Pojections Trough 2030 Prepared for INGAA Foundation, Inc. by: ICF International, (2009).

[119] M. El-Bourawi, Z. Ding, R. Ma, M. Khayet, A framework for better understanding membrane distillation separation process, Journal of Membrane Science, 285 (2006) 4-29.

[120] L. Song, B. Li, K.K. Sirkar, J.L. Gilron, Direct Contact Membrane Distillation-Based Desalination: Novel Membranes, Devices, Larger-Scale Studies, and a Model, Industrial & Engineering Chemistry Research, 46 (2007) 2307-2323.

[121] R.W. Schofield, A.G. Fane, C.J.D. Fell, R. Macoun, Factors affecting flux in membrane distillation, Desalination, 77 (1990) 279-294.

[122] K.W. Lawson, D.R. Lloyd, Membrane distillation, Journal of membrane Science, 124 (1997) 1-25.

[123] R.D. Gustafson, J.R. Murphy, A. Achilli, A stepwise model of direct contact membrane distillation for application to large-scale systems: Experimental results and model predictions, Desalination, 378 (2016) 14-27.

[124] O.R. Lokare, S. Tavakkoli, S. Wadekar, V. Khanna, R.D. Vidic, Fouling in direct contact membrane distillation of produced water from unconventional gas extraction, Journal of Membrane Science, 524 (2017) 493-501.

[125] G. Guan, X. Yang, R. Wang, R. Field, A.G. Fane, Evaluation of hollow fiber-based direct contact and vacuum membrane distillation systems using aspen process simulation, Journal of Membrane Science, 464 (2014) 127-139.

[126] M.A. Izquierdo-Gil, C. Fernández-Pineda, M. Lorenz, Flow rate influence on direct contact membrane distillation experiments: different empirical correlations for Nusselt number, Journal of Membrane Science, 321 (2008) 356-363.

[127] K. He, H.J. Hwang, M.W. Woo, I.S. Moon, Production of drinking water from saline water by direct contact membrane distillation (DCMD), Journal of Industrial and Engineering Chemistry, 17 (2011) 41-48.

[128] C. Shaw, in, Alfa Laval Inc., 2015.

[129] Y.M. Manawi, M. Khraisheh, A.K. Fard, F. Benyahia, S. Adham, Effect of operational parameters on distillate flux in direct contact membrane distillation (DCMD): Comparison between experimental and model predicted performance, Desalination, 336 (2014) 110-120.

[130] U.V. Shenoy, Heat exchanger network synthesis: process optimization by energy and resource analysis, Gulf Professional Publishing, 1995.

[131] T.F. Russell, A.S. Robinson, N.J. Wagner, Mass and heat transfer: analysis of mass contactors and heat exchangers, Cambridge University Press, 2008.

[132] S.M. Hall, Rules of thumb for chemical engineers, Butterworth-Heinemann, 2012.

[133] F. He, J. Gilron, K.K. Sirkar, High water recovery in direct contact membrane distillation using a series of cascades, Desalination, 323 (2013) 48-54.

[134] S. Lin, N.Y. Yip, M. Elimelech, Direct contact membrane distillation with heat recovery: Thermodynamic insights from module scale modeling, Journal of Membrane Science, 453 (2014) 498-515.

[135] M. Khayet, J. Mengual, G. Zakrzewska-Trznadel, Direct contact membrane distillation for nuclear desalination, Part II: experiments with radioactive solutions, International journal of nuclear desalination, 2 (2006) 56-73.

[136] M.S. Khayet, T. Matsuura, Membrane Distillation : Principles and Applications, Elsevier Science & Technology, Saint Louis, MO, USA, 2011.

[137] S. Al-Obaidani, E. Curcio, F. Macedonio, G. Di Profio, H. Al-Hinai, E. Drioli, Potential of membrane distillation in seawater desalination: thermal efficiency, sensitivity study and cost estimation, Journal of Membrane Science, 323 (2008) 85-98.

[138] A. Kayvani Fard, Y.M. Manawi, T. Rhadfi, K.A. Mahmoud, M. Khraisheh, F. Benyahia, Synoptic analysis of direct contact membrane distillation performance in Qatar: A case study, Desalination, 360 (2015) 97-107.

[139] J. Gilron, L. Song, K.K. Sirkar, Design for Cascade of Crossflow Direct Contact Membrane Distillation, Industrial & Engineering Chemistry Research, 46 (2007) 2324-2334.

[140] H. Lee, F. He, L. Song, J. Gilron, K.K. Sirkar, Desalination with a cascade of cross-flow hollow fiber membrane distillation devices integrated with a heat exchanger, AIChE Journal, 57 (2011) 1780-1795.

[141] PADEP, Pennsylvania Department of Environmental Protection, http://www.depweb.state.pa.us/ (accessed July 15, 2015), (2015).

[142] PADEP, Pennsylvania Department of Environmental Protection, http://www.depreportingservices.state.pa.us/ReportServer/Pages/ReportViewer.aspx?%2fOil_Gas%2fOil_Gas_Well_Historical_Production_Report (accessed May 15, 2015), (2015).

[143] D. Yoxtheimer, Appalachian shale energy produced fluids management and UIC well disposal trends, http://www.saferpa.org/Documents/Resources/TechBrief-08-2015/Appalachian-Shale-Energy-Produced-Fluids-Management-UIC-Well-Disposal-Trends_SaferPA-08-20-2015.pdf (accessed May 20, 2015), (2015).

[144] H.C. Duong, A.R. Chivas, B. Nelemans, M. Duke, S. Gray, T.Y. Cath, L.D. Nghiem, Treatment of RO brine from CSG produced water by spiral-wound air gap membrane distillation—A pilot study, Desalination, (2014).

[145] J. Minier-Matar, R. Sharma, A. Hussain, A. Janson, S. Adham, Field evaluation of membrane distillation followed by humidification/dehumidification crystallizer for inland desalination of saline groundwater, Desalination, 398 (2016) 12-21.

[146] J. Minier-Matar, A. Hussain, A. Janson, S. Adham, Treatment of produced water from unconventional resources by membrane distillation, in: IPTC 2014: International Petroleum Technology Conference, 2014.

[147] H. Fan, Y. Peng, Application of PVDF membranes in desalination and comparison of the VMD and DCMD processes, Chemical Engineering Science, 79 (2012) 94-102.

[148] G. Zuo, R. Wang, R. Field, A.G. Fane, Energy efficiency evaluation and economic analyses of direct contact membrane distillation system using Aspen Plus, Desalination, 283 (2011) 237-244.

[149] E. Guillén-Burrieza, J. Blanco, G. Zaragoza, D.-C. Alarcón, P. Palenzuela, M. Ibarra, W. Gernjak, Experimental analysis of an air gap membrane distillation solar desalination pilot system, Journal of Membrane Science, 379 (2011) 386-396.

[150] S. Mondal, S.R. Wickramasinghe, Produced water treatment by nanofiltration and reverse osmosis membranes, Journal of Membrane Science, 322 (2008) 162-170.

[151] C.J. Gabelich, M.D. Williams, A. Rahardianto, J.C. Franklin, Y. Cohen, High-recovery reverse osmosis desalination using intermediate chemical demineralization, Journal of Membrane Science, 301 (2007) 131-141.

[152] S.S. Wadekar, T. Hayes, O.R. Lokare, D. Mittal, R.D. Vidic, Laboratory and pilot-scale nanofiltration treatment of abandoned mine drainage for the recovery of products suitable for industrial reuse, Industrial & Engineering Chemistry Research, 56 (2017) 7355-7364.

[153] G. Guan, X. Yang, R. Wang, A.G. Fane, Evaluation of heat utilization in membrane distillation desalination system integrated with heat recovery, Desalination, 366 (2015) 80-93.

[154] A. Khalifa, H. Ahmad, M. Antar, T. Laoui, M. Khayet, Experimental and theoretical investigations on water desalination using direct contact membrane distillation, Desalination, 404 (2017) 22-34.

[155] J. Swaminathan, H.W. Chung, D.M. Warsinger, J.H. Lienhard V, Simple method for balancing direct contact membrane distillation, Desalination, 383 (2016) 53-59.

[156] A. Hausmann, P. Sanciolo, T. Vasiljevic, M. Weeks, M. Duke, Integration of membrane distillation into heat paths of industrial processes, Chemical Engineering Journal, 211–212 (2012) 378-387.

[157] P.J. Foster, A. Burgoyne, M.M. Vahdati, Improved process topology for membrane distillation, Separation and Purification Technology, 21 (2001) 205-217.

[158] J. Zhang, S. Gray, J.-D. Li, Modelling heat and mass transfers in DCMD using compressible membranes, Journal of Membrane Science, 387 (2012) 7-16.

[159] L.M. Camacho, L. Dumée, J. Zhang, J.-d. Li, M. Duke, J. Gomez, S. Gray, Advances in membrane distillation for water desalination and purification applications, Water, 5 (2013) 94-196.

[160] O.R. Lokare, S. Tavakkoli, G. Rodriguez, V. Khanna, R.D. Vidic, Integrating membrane distillation with waste heat from natural gas compressor stations for produced water treatment in Pennsylvania, Desalination, 413 (2017) 144-153.

[161] K. Yao, Y. Qin, Y. Yuan, L. Liu, F. He, Y. Wu, A continuous-effect membrane distillation process based on hollow fiber AGMD module with internal latent-heat recovery, AIChE Journal, 59 (2013) 1278-1297.

[162] L. Martínez-Díez, M.I. Vázquez-González, A method to evaluate coefficients affecting flux in membrane distillation, Journal of Membrane Science, 173 (2000) 225-234.

[163] L.G. Liu, C. Zhu, S.C. Cheung, W.C. Leung, Theoretical and experimental studies on air gap membrane distillation, Heat and Mass Transfer, 34 (1998) 329-335.

[164] F.A. Banat, J. Simandl, Desalination by Membrane Distillation: A Parametric Study, Separation Science and Technology, 33 (1998) 201-226.

[165] L. Martínez, J.M. Rodríguez-Maroto, On transport resistances in direct contact membrane distillation, Journal of Membrane Science, 295 (2007) 28-39.

[166] J.C. Chen, Q. Li, M. Elimelech, In situ monitoring techniques for concentration polarization and fouling phenomena in membrane filtration, Advances in Colloid and Interface Science, 107 (2004) 83-108.

[167] A. Kroiß, S. Eyerer, J. Kuczaty, C. Thies, S. Wolf, A. Präbst, M. Spinnler, T. Sattelmayer, Optical methods for simultaneous measurement of temperature and concentration polarization, in: Proceedings of the International Desalination Association World Congress on Desalination and Water Reuse, 2015.

[168] V. Chen, H. Li, A.G. Fane, Non-invasive observation of synthetic membrane processes – a review of methods, Journal of Membrane Science, 241 (2004) 23-44.

[169] V. Vilker, C. Colton, K. Smith, Concentration polarization in protein ultrafiltration, AIChE J, 27 (1981) 632.

[170] C.R. Ethier, D.C. Lin, Refractometric measurement of polarized layer structure: studies of hyaluronic acid ultrafiltration, Journal of Membrane Science, 68 (1992) 249-261.

[171] L.M. Gowman, C.R. Ethier, Concentration and concentration gradient measurements in an ultrafiltration concentration polarization layer Part I: A laser-based refractometric experimental technique, Journal of Membrane Science, 131 (1997) 95-105.

[172] L.M. Gowman, C. Ross Ethier, Concentration and concentration gradient measurements in an ultrafiltration concentration polarization layer Part II: Application to hyaluronan, Journal of Membrane Science, 131 (1997) 107-123.

[173] P. Schiebener, J. Straub, J. Levelt Sengers, J. Gallagher, Refractive index of water and steam as function of wavelength, temperature and density, Journal of physical and chemical reference data, 19 (1990) 677-717.

[174] J. Fernández-Sempere, F. Ruiz-Beviá, P. García-Algado, R. Salcedo-Díaz, Experimental study of concentration polarization in a crossflow reverse osmosis system using Digital Holographic Interferometry, Desalination, 257 (2010) 36-45.

[175] D. Mahlab, N.B. Yosef, G. Belfort, Concentration polarization profile for dissolved species in unstirred batch hyperfiltration (Reverse Osmosis) - II Transient case, Desalination, 24 (1977) 297-303.

[176] J. Fernández-Sempere, F. Ruiz-Beviá, R. Salcedo-Díaz, Measurements by holographic interferometry of concentration profiles in dead-end ultrafiltration of polyethylene glycol solutions, Journal of Membrane Science, 229 (2004) 187-197.

[177] J. Fernández-Sempere, F. Ruiz-Beviá, P. García-Algado, R. Salcedo-Díaz, Visualization and modelling of the polarization layer and a reversible adsorption process in PEG-10000 dead-end ultrafiltration, Journal of Membrane Science, 342 (2009) 279-290.

[178] S. Yao, M. Costello, A.G. Fane, J.M. Pope, Non-invasive observation of flow profiles and polarisation layers in hollow fibre membrane filtration modules using NMR micro-imaging, Journal of Membrane Science, 99 (1995) 207-216.

[179] J.M. Pope, S. Yao, A.G. Fane, Quantitative measurements of the concentration polarisation layer thickness in membrane filtration of oil-water emulsions using NMR micro-imaging, Journal of Membrane Science, 118 (1996) 247-257.

[180] D. Airey, S. Yao, J. Wu, V. Chen, A.G. Fane, J.M. Pope, An investigation of concentration polarization phenomena in membrane filtration of colloidal silica suspensions by NMR micro-imaging, Journal of Membrane Science, 145 (1998) 145-158.

[181] R.M. Mc Donogh, H. Bauser, N. Stroh, U. Grauschopf, Experimental in situ measurement of concentration polarisation during ultra- and micro-filtration of bovine serum albumin and Dextran Blue solutions, Journal of Membrane Science, 104 (1995) 51-63.

[182] S. Tavakkoli, O.R. Lokare, R.D. Vidic, V. Khanna, A techno-economic assessment of membrane distillation for treatment of Marcellus shale produced water, Desalination, 416 (2017) 24-34.

[183] V. Di Noto, M. Mecozzi, Determination of seawater salinity by ultraviolet spectroscopic measurements, Applied Spectroscopy, 51 (1997) 1294-1302.

[184] X. Li, L. Liu, J. Zhao, J. Tan, Optical Properties of Sodium Chloride Solution Within the Spectral Range from 300 to 2500 nm at Room Temperature, Applied spectroscopy, 69 (2015) 635-640.

[185] A. Mottana, F. Burragato, Absorption Spectroscopy in Mineralogy, in, Elsevier, New York, 1990.

[186] H. Hosoda, H. Mori, N. Sogoshi, A. Nagasawa, S. Nakabayashi, Refractive Indices of Water and Aqueous Electrolyte Solutions under High Magnetic Fields, The Journal of Physical Chemistry A, 108 (2004) 1461-1464.

[187] A. Tamburini, P. Pitò, A. Cipollina, G. Micale, M. Ciofalo, A Thermochromic Liquid Crystals Image Analysis technique to investigate temperature polarization in spacer-filled channels for Membrane Distillation, Journal of membrane science, 447 (2013) 260-273.

[188] C. Morrell, Personal Communication, in, Thermo Fisher Scientific, 8th March, 2017.

[189] M.S. Khayet, T. Matsuura, ebrary Inc., Membrane distillation principles and applications, in, Elsevier,, Amsterdam ; Boston, 2011, pp. 1 online resource.

[190] A. Bahmanyar, M. Asghari, N. Khoobi, Numerical simulation and theoretical study on simultaneously effects of operating parameters in direct contact membrane distillation, Chemical Engineering and Processing: Process Intensification, 61 (2012) 42-50.

[191] A. Tamburinia, G. Micalea, M. Ciofalob, A. Cipollinaa, Experimental analysis via thermochromic liquid crystals of the temperature local distribution in membrane distillation modules, CHEMICAL ENGINEERING, 32 (2013).

[192] M.E. Leitch, G.V. Lowry, M.S. Mauter, Characterizing convective heat transfer coefficients in membrane distillation cassettes, Journal of Membrane Science, 538 (2017) 108-121.

[193] CRC Handbook of Chemistry and Physics, 83 ed., 2002.

[194] L.C. Thomas, Fundamentals of heat transfer, (1980).

[195] R.K. Shah, A.L. London, Laminar flow forced convection in ducts: a source book for compact heat exchanger analytical data, Academic press, 2014.

[196] E.N. Sieder, G.E. Tate, Heat Transfer and Pressure Drop of Liquids in Tubes, Industrial & Engineering Chemistry, 28 (1936) 1429-1435.

[197] A.L. Zydney, Stagnant film model for concentration polarization in membrane systems, Journal of Membrane Science, 130 (1997) 275-281.

[198] M.S.H. Bader, J.N. Veenstra, Analysis of concentration polarization phenomenon in ultrafiltration under turbulent flow conditions, Journal of Membrane Science, 114 (1996) 139-148.

[199] I.D. Zaytsev, G.G. Aseyev, Properties of aqueous solutions of electrolytes, CRC press, 1992.

[200] X. Yi, J. Hu, X. Zhang, M. Sun, S. Liu, A Temperature-Dependent Thermodynamic Model Derived from Heat Capacity of Metal Chloride Aqueous Solutions, Journal of Chemical & Engineering Data, 62 (2017) 4117-4127.

[201] M. Laliberté, Model for Calculating the Viscosity of Aqueous Solutions, Journal of Chemical & Engineering Data, 52 (2007) 321-335.

[202] M. Laliberté, W.E. Cooper, Model for Calculating the Density of Aqueous Electrolyte Solutions, Journal of Chemical & Engineering Data, 49 (2004) 1141-1151.

[203] R.H. Stokes, S. Phang, R. Mills, Density, conductance, transference numbers, and diffusion measurements in concentrated solutions of nickel chloride at 25°C, Journal of Solution Chemistry, 8 (1979) 489-500.

[204] A. Kumano, M. Sekino, Y. Matsui, N. Fujiwara, H. Matsuyama, Study of mass transfer characteristics for a hollow fiber reverse osmosis module, Journal of Membrane Science, 324 (2008) 136-141.

[205] M. Gryta, M. Tomaszewska, A.W. Morawski, Membrane distillation with laminar flow, Separation and Purification Technology, 11 (1997) 93-101.

[206] Y. Chang, A. Myerson, The diffusivity of potassium chloride and sodium chloride in concentrated, saturated, and supersaturated aqueous solutions, AIChE journal, 31 (1985) 890-894.

[207] B. Jiao, A. Cassano, E. Drioli, Recent advances on membrane processes for the concentration of fruit juices: a review, Journal of Food Engineering, 63 (2004) 303-324.

[208] K. Hideki, S. Yasuyoshi, I. Akihide, K. Akihiko, Role of Iron Ion Electron Mediator on Photocatalytic Overall Water Splitting under Visible Light Irradiation Using Z-Scheme Systems, Bulletin of the Chemical Society of Japan, 80 (2007) 2457-2464.

[209] J. Grodkowski, P. Neta, Copper-Catalyzed Radiolytic Reduction of CO2 to CO in Aqueous Solutions, The Journal of Physical Chemistry B, 105 (2001) 4967-4972.

[210] H.B. Albada, F. Soulimani, B.M. Weckhuysen, R.M.J. Liskamp, Scaffolded amino acids as a close structural mimic of type-3 copper binding sites, Chemical Communications, (2007) 4895-4897.